Experimental studies on the behaviour of rare earth elements and tin in granitic systems

DISSERTATION

zur Erlangung des Doktorgrades der Naturwissenschaften

der Geowissenschaflichen Fakultät
der Eberhard-Karls-Universität Tübingen

vorgelegt von

QUACH DUC TIN
aus Hanoi (Vietnam)

- 2007 -

Tag der mündlichen Prüfung:	
Dekan:	Prof. Dr. Peter Grathwohl
1. Berichterstatter:	Prof. Dr. Hans Keppler
2. Berichterstatter:	Priv. Doz. Dr. Wolfgang Siebel

Acknowledgements

This thesis is the results of the scientific research mainly at Institute for Geosciences, University of Tuebingen (EBERHARD-KARLS-UNIVERSITÄT TÜBINGEN). Some parts were carried out at the University of Hannover and Swiss Federal Institute of Technology in Zürich (ETH Zürich). With a great sense of appreciation, I take the opportunity to thank those people who have helped, supported and encouraged me along the way. I would like to thank my colleagues and other people I had the opportunity to work with.

I am greatly indebted to my supervisor, Prof. Dr. Hans Keppler, whose comments, valuable scientific discussions and critical ideas are highlights of various aspects of this research. Without his financial aid, sound guidance, supervision, motivation, kindness and continual support, this research would have not reached its present form. With his patience and encouragement, he gave me the confidence to complete this thesis. I also highly appreciate his support by sending me to other scientific institutions to do the research as well as solving the financial matters related to the research. Moreover, his personal qualities, inter-personal skills and good humor created an excellent working environment at Institute for Geosciences.

Most of this work was funded by the DFG Leibniz award of my supervisor, Prof. Hans Keppler. In addition, the German Academic Exchange Service (DAAD) fellowship program sponsored this work.

I would also like to acknowledge and extend my thanks to Dr. Andreas Audetat for his ideas about inclusion trapping experimental set-up and for many helpful discussions and suggestions during the course of the research. I thank him for arranging the working session in ETH Zürich, for providing technical assistance with Laser-ablation ICP-MS and for his patience and creativity when working with me.

My thanks and appreciation go out to all the others who helped me with scientific and technical aspects of this project, including PD. Dr. Thomas Wenzel for teaching and providing me technical assistance in working with electron microprobe (JEOL 8900), Dr. Christoph Berthold for helping me to carry out X-ray diffraction analysis, Prof. Detlef Günther and Kathrin Hametner for arranging the LA- ICP-MS analysis in ETH, Zurich, Prof. Marcus Nowak for arranging the experiments at Hannover University and Mr. Norbert

Walker for his assistance in maintaining the high temperature and pressure vessels system in the lab.

Great appreciation is given to my colleagues and friends in the Institute for Geosciences, who were always willingly to discuss and never hesitated to help me out in whatever way they could. To name a few, Mrs. Dagmar Dimitrovice, Dr. Katrin Mierdel, Dr. Nguyen Thi Bich Thuy, Dr. Bernd Binder, Dr. Johannes Baier, Dr. Syvatoslav Shcheka, Dr. Udo Neumann, Dipl. Volker Presser, Dr. Baldorj Baatartsogt, Dr. Michael Dorn, Dr. Giovanna Laudisio, Mr. Gregor Seidel, Mr. Alexander Konschak, Dr. Michael Marks, Dr. Martin O'Connell, Miss. Jasmin Koehler, Miss. Gesa Graser, Mr. Thomas Krumrei and all my friends in the institute.

Last but not least, I would like to express special thanks to my parent, sisters, brothers, my wife and daughter, who all supported and encouraged me in pursuing my study. Without them a little could have been achieved. They make my life filled with love and happiness.

Table of contents

Part II: Solubility of tin in magmatic-hydrothermal fluids ... 96

List of figures

List of tables

Abstract

In this thesis, the behavior of rare earth elements and of tin during the crystallization of a granitic magma and the release of hydrothermal fluids has been studied in two series of experiments in hydrothermal cold seal bombs.

Part I: Monazite and xenotime solubility in haplogranitic melts

Crystals of pure rare earth phosphates were synthesized for each rare earth element (except Pm) by the reaction of rare earth oxides with aqueous solutions of phosphoric acids at 800 °C and 2 kbar. The light rare earths from La to Gd formed crystals of monazite, while the heavy rare earths from Gd to Lu formed xenotime. The $GdPO_4$ samples were a mixture of the monazite and xenotime polymorph.

The solubility of the rare earth phosphates in hydrous (6 wt. % H_2O) haplogranitic melts with aluminum saturation index ranging from 0.7 to 1.2 was investigated at 2 kbar and 800 °C with run durations between one and two months. The influence of phosphorus and fluorine rare earth phosphate solubility was also studied under the same conditions. One additional series of experiments was carried out at 1100 °C and 2 kbar. Run products were investigated by electron microprobe. Equilibrium rare earth concentrations were estimated both from average microprobe analyses and from the extrapolation of measured diffusion profiles around dissolving crystals to the crystal-melt interface. To demonstrate equilibrium, runs with variable duration and reversed experiments were carried out as well.

Monazite solubility decreases with phosphorus concentration in the melt. This effect can be quantitatively modeled if one assumes that monazite partially dissolves as ionic and molecular species (Gd^{3+} and $GdPO_4$). Equilibrium constant for the dissolution reactions as well as quantitative data on speciation have been derived from the solubility data. Monazite and xenotime solubility strongly increase with the peralkalinity of the melt. This effect is mostly due to an increase in the solubility of the ionic species, which are probably stabilized by non-bridging oxygen atoms in the melt. Lanthanum is the only rare earth element, which does not appear to show a major increase in monazite solubility in peralkaline melts. In peraluminous melts, the solubility of monazite and xenotime is nearly constant. Fluorine has no major effect

on monazite and xenotime solubility; in fact, the solubility appears to slightly decrease with fluorine content.

The solubility of rare earth phosphates is not a simple continuous function of atomic number or ionic radius. Rather, the solubility shows a typical “tetrad” pattern with several local maxima of solubility at individual rare earth elements. The solubilities of neighboring rare earth elements sometimes differ by more than a factor of two; these effects are far outside any analytical error. The tetrad pattern is particularly clearly seen in some of the peralkaline melts and in the fluorine-rich metaluminous melts. Some features, however, such as solubility maximum at ytterbium, are seen in virtually all melts.

The lanthanide tetrad effect in some highly evolved granites is therefore likely to be a result of monazite and xenotime fractionation. The ultimate cause of the tetrad effect is probably electronic repulsion between the partially filled f-orbitals of the rare earth and the surrounding oxygen atoms. If the coordination geometry is different in the melt and the solid phase, the rare earth partition coefficients or solubilities will depend on the precise electronic configuration in the 4f shell, not just on the effective ionic radius. The solubility of monazite and xenotime in silicate melt probably shows this tetrad effect, because of the very unusual coordination of the rare earth elements in these phosphate minerals.

The lanthanide tetrad effect in some highly evolved granites is real. However, it cannot be used as an indicator of fluid/rock or fluid/melt interaction experienced by these granites, since the effect can be experimentally reproduced in the laboratory in the absence of any fluids.

Part II: Solubility of tin in magmatic-hydrothermal fluids

Synthetic fluid inclusions in quartz were grown from cassiterite-saturated fluid in cold-seal pressure vessels at 700 °C / 140 MPa / $f\mathrm{O}_2$ ~ NNO and subsequently analyzed by Laser-Ablation ICP-MS. Most inclusions were synthesized using a new technique that allows entrapment of fluid that had no immediate contact to the capsule walls, such that potential disequilibrium effects due to alloying could be avoided. Measured Sn solubilities increase with increasing ligand concentration in the fluid, ranging from 100 to 800 ppm in NaCl-bearing fluids (5-35 wt.% NaCl), from 70 to 2000 ppm in HF-bearing fluids (0.5-3.2 m HF), and from 0.8 to 11 wt.% in HCl-bearing fluids (0.5-4.4 m HCl). Runs performed by in-situ

cracking after one week of pre-equilibration demonstrate that fluid inclusions grown by the new technique failed to reach equilibrium in the most acid HCl and HF solutions because the inclusion production rate was too fast. Graphical evaluation of the solubility data suggests that Sn may have been dissolved as Sn(OH)Cl in the NaCl-bearing fluids, as Sn(OH)Cl and $SnCl_2$ in the HCl-bearing fluids, and as SnF_2 in the HF-bearing fluids. Experiments with NaF-bearing fluids produced an additional melt phase with an approximate composition 53 wt.% SiO_2, 25 wt.% H_2O, 14 wt.% NaF and 8 wt.% SnO, which caused the composition of the coexisting fluid to be buffered at 0.5 wt.% NaF and 150 ppm Sn. Fluorine-rich, peralkaline melts may therefore serve as important transport medium for Sn in the final crystallization stages of tin granites. Based on the available cassiterite solubility data in fluids and melts, $D_{Sn, fluid/melt}$ in natural granite systems is estimated to be in the order of 0.1-4 (depending on their aluminosity), suggesting that Sn cannot easily be mobilized by magmatic-hydrothermal fluids. This interpretation is in accordance with the high degrees of Sn enrichment commonly observed in highly fractionated melt inclusions. $D_{Sn, fluid/melt}$ is primarily controlled by the HCl concentration in the fluid. Compared to HCl, the effect of fluorine on $D_{Sn, fluid/melt}$ is subordinate.

Zusammenfassung

In dieser Dissertation wurde das Verhalten der Seltenen Erden und von Zinn bei der Kristallisation eines Granitmagmas und bei der Freisetzung hydrothermaler Fluide experimentell untersucht. Die Experimente wurden in hydrothermalen Autoklaven vom "Cold-seal"-Typ ausgeführt.

Teil I: Monazit- and Xenotim-Löslichkeit in haplogranitischen Schmelzen

Kristalle von reinen Seltenerd-Phosphaten wurden für jede Seltene Erde (außer Pm) synthetisiert durch Reaktion der Oxide mit wäßrigen Lösungen von Phosphorsäure bei 800 ˚C und 2 kbar. Die leichten Seltenen Erden von La bis Gd bildeten Kristalle von Monazit, während die schweren Seltenen Erden von Gd bis Lu Xenotim bildeten. Die $GdPO_4$-Proben waren eine Mischung der Monazit- und Xenotim-Modifikation.

Die Löslichkeit der Seltenerd-Phosphate in wasserhaltigen (6 Gew. % Wasser) haplogranitischen Schmelzen mit einem ASI von 0,7 bis 1,2 wurde bei 2 kbar und 800 ˚C untersucht mit Versuchsdauern zwischen einem und zwei Monaten. Der Einfluß von Phosphor und Fluor auf die Seltenerd-Phosphat-Löslichkeit wurde ebenfalls unter den gleichen Bedingungen untersucht. Eine zusätzliche Serie von Experimenten wurde bei 1100 ˚C ausgeführt. Versuchsprodukte wurden untersucht mit Hilfe der Elektronenstrahl-Mikrosonde. Gleichgewichts-Konzentrationen der Seltenen Erden wurden abgeschätzt sowohl aus gemittelten Mikrosonden-Analysen als auch durch die Extrapolation von gemessenen Diffusionsprofilen um Kristalle zur Grenzfläche Kristall-Schmelze. Um Gleichgewichtseinstellung nachzuweisen, wurden Experimente mit variabler Versuchsdauer und reversible Experimente ausgeführt.

Die Löslichkeit von Monazit nimmt mit der Konzentration von Phosphor in der Schmelze ab. Dieser Effekt kann quantitativ modelliert werden, wenn man annimmt, dass Monazit teilweise in ionischer und teilweise in molekularer Form gelöst wird (als Gd^{3+} und $GdPO_4$). Gleichgewichtskonstanten für die Lösungs-Reaktion sowie quantitative Daten zur Speziation wurden aus den gemessenen Löslichkeiten abgeleitet. Die Löslichkeit von Monazit und Xenotim nimmt mit der Peralkalinität der Schmelze stark zu. Dieser Effekt beruht überwiegend auf einer Zunahme der Löslichkeit der ionischen Spezies, welche stabilisiert werden durch nicht-brückenbildende Sauerstoffatome in der Schmelze. Lanthan ist die einzige Seltene Erde, für die keine wesentliche Zunahme der Monazit-Löslichkeit mit der Paralkalinität beobachtet wurde. In peraluminischen Schmelzen ist die Löslichkeit von Monazit und Xenotim etwa konstant. Fluor hat keinen wesentlichen Effekt auf die Löslichkeit von Monazit und Xenotim; die Löslichkeit scheint bei Gegenwart von Fluor sogar leicht abzunehmen.

Die Löslichkeit der Seltenerd-Phosphate ist keine einfache kontinuierliche Funktion der Ordnungszahl oder des Ionenradius. Die Löslichkeit zeigt ein typisches „Tetraden“-Muster mit mehreren lokalen Maxima der Löslichkeit bei einzelnen Seltenerd-Elementen. Die Löslichkeiten benachbarter Seltenerd-Elemente unterscheiden sich manchmal um mehr als einen Faktor von zwei; diese Effekte sind weit größer als die analytischen Fehler. Das Tetraden-Muster ist besonders deutlich in einigen peralkalischen Schmelzen sowie in Fluor-reichen metaluminischen Schmelzen. Einige Effekte, wie etwa das Löslichkeits-Maximum bei Ytterbium, konnten bei allen Schmelzzusammensetzungen beobachtet werden.

Der Lanthaniden-Tetraden-Effekt in einigen hochdifferenzierten Graniten ist daher wahrscheinlich ein Resultat der Fraktionierung von Monazit und Xenotim. Die letztliche Ursache für den Tetraden-Effekt liegt wahrscheinlich in der Abstoßung zwischen den Elektronen der teilweise gefüllten f-Orbitale der Seltenen Erd-Kationen und den umgebenden Sauerstoff-Atomen. Sofern die Koordinationsgeometrie in der Schmelze und der koexistierenden festen Phase unterschiedlich ist, werden die Löslichkeiten und Verteilungskoeffizienten der Seltenen Erden nicht nur vom Ionenradius, sondern von der genauen Besetzung der einzelnen f-Orbitale abhängen. Die Löslichkeit von Monazit und Xenotim in Silikatschmelzen zeigt wahrscheinlich den Tetraden-Effekt, weil die Koordinationsgeometrie der Seltenen Erden in Monazit und Xenotim sehr ungewöhnlich ist.

Der Lanthanide-Tetraden-Effekt in einigen hochdifferenzierten Graniten ist real. Dieser Effekt kann jedoch nicht benutzt werden als ein Indikator für Fluid-Gesteins- oder Fluid-Schmelze-Wechselwirkungen in der Entwicklung dieser Granite, da der Effekt sich im Labor auch in Abwesenheit einer Fluidphase reproduzieren lässt.

Tei II: Löslichkeit von Zinn in magmatisch-hydrothermalen Fluiden

Synthetische Flüssigkeitseinschlüsse in Quarz wurden aus Kassiterit-gesättigten Fluiden in Hydrothermal-Autoklaven bei 700 °C / 140 MPa / f_{O2} ~ NNO gezüchtet, und anschliessend mittels Laser-Ablation ICP-MS analysiert. Die meisten Einschlüsse wurden mit Hilfe einer speziellen Synthese-Technik hergestellt mit der es möglich ist, Fluid einzufangen welches für geraume Zeit nicht mit der umgebenden Goldkapsel in Kontakt war. Auf diese Weise kann verhindert werden, dass die Zinnlöslichkeit im Fluid durch die Legierung von Zinn in die Goldkapsel beeinflusst wird. Die gemessenen Zinn-Löslichkeiten steigen mit zunehmender Ligand-Konzentration im Fluid, und reichen von 100 bis 800 ppm in NaCl-haltigen Fluiden (5-35 Gew.% NaCl), von 70 bis 2000 ppm in HF-haltigen Fluiden (0.5-3.2 m HF), und von 0.8 bis 11 Gew.% in HCl-haltigen Fluiden (0.5-4.4 m HCl). Experimente bei denen die Einschlussbildung durch in-situ Abschreckung nach einer Woche Vorequilibrierung ausgelöst wurde zeigen, dass die neue Technik in konzentrierten HCl und HF-Lösungen versagte weil die Einschlussbildung vor Erreichen des Lösungsgleichgewichts erfolgte. Die Löslichkeitsdaten implizieren, dass Sn überwiegend in Form von Sn(OH)Cl in den NaCl-haltigen gelöst war, in Form von Sn(OH)Cl und $SnCl_2$ in HCl-haltigen Fluiden, und in Form von SnF_2 in HF-haltigen Fluiden. Experimente mit NaCl-haltigen Fluiden führten zur Bildung einer zusätzlichen Schmelzphase mit der ungefähren Zusammensetzung 53 Gew.% SiO_2, 25 Gew.% H_2O, 14 Gew.% NaF und 8 Gew.% SnO. Die Präsenz dieser Schmelzphase führte dazu, dass der NaF-Gehalt im koexistierenden Fluid bei 0.5 Gew.% NaF und 150 ppm Sn gepuffert wurde. Diese Resultate implizieren, dass Fluor- und Alkali-reiche Schmelzen ein wichtiges Transportmedium für Zinn im Endstadium der Kristallisation von Zinn-Graniten darstellen könnten. Der Verteilungskoeffizient $D_{Sn, fluid/melt}$ in natürlichen Graniten wird auf ca. 0.1-4 geschätzt, was bedeutet, dass Sn nur schwierig mittels magmatisch-hydrothermalen Fluide mobilisiert werden kann. Diese Interpretation steht im Einklang mit der Beobachtung, dass Sn in hochfraktionierten Schmelzeinschlüssen oft stark angereichert ist. $D_{Sn, fluid/melt}$ ist primär durch die HCl-Konzentration im Fluid kontrolliert, während die Konzentration von F im Fluid eine eher untergeordnete Rolle spielt.

Part I: Monazite and xenotime solubility in haplogranitic melts

1. Introduction

1.1. General geochemistry of rare earth elements

Rare earth elements (REE´s) or lanthanides are a group of 15 elements, beginning with lanthanum (La, atomic number 57) and ending with lutetium (Lu, atomic number 71). All lanthanides occur in nature, except Promethium (Pm), which is radioactive and extinct.

All rare earth atoms have the same electronic configuration in their outer two shells ($5d^1$ $6s^2$) and they differ only by the number of 4f electrons, which ranges from zero for La to 14 for Lu. Because of the identical electronic configuration in the outer two shells, the properties of all rare earth elements are quite similar. However, the increasing number of f electrons and the simultaneously increasing nuclear charge cause the atomic and ionic radii to decrease significantly from La to Lu (Table 1.1). This feature is known as the lanthanide contraction and occurs because the inner electron shell is built up rather a new shell being added. This change in atomic and ionic radii causes a subtle and smooth change in physical and chemical properties. However, some of the properties of the rare earth elements may be slightly influenced by crystal field effects due to the interaction between the partially filled f orbitals and the surrounding ligands. Such an interaction is probably responsible for the “lanthanide tetrad effect” first described by Peppard et al. (1969). This effect implies that certain thermodynamic properties, such as solubility or partition coefficients, have minima or maxima for those rare earth elements possessing a quarter, half or three quarter filled f shell.

Rare earth elements are sometimes classified into two subgroups: the light rare earth or cerium subgroup (abbreviated LREE), comprising the first seven elements from La to Eu (atomic numbers 57-63), and the heavy rare earth or yttrium subgroup (abbreviated HREE), comprising the elements from Gd to Lu with atomic numbers 64-71. Yttrium and scandium, although they are not real rare earth elements, have properties similar to the heavy rare earth.

Important rare earth minerals include monazite [$(Ce,La,Nd,Th)(PO_4)$], [$(REE)PO_4$], xenotime [$Y,REE(PO_4)$], bastnaesite [$(Ce,La)(CO_3)F$] and apatite [$Ca,REE)_5(PO_4)_3(OH,F)$]. The most important commercial sources of REE have been monazite bearing placer deposits such as fluviatile deposits in North Carolina and beach placers in Brazil, India, China and Australia (Neary and Highley, 1984). Bastnaesite and monazite are sources of the light REE and account for about 95% of the current REE production, while xenotime and minerals such as allanite are a source of the heavy REE and yttrium. Monazite commonly contains thorium up to 10%, some yttrium and a small amount of uranium.

Table 1.1 Ionic radii (Å) of REE ions (mostly of valency state 3+) for co-ordination numbers (CN) 6 and 8, based on O^{2-} radius of 1.40 Å (Shannon, 1976)

Name	Symbol	Atomic No.	Atomic weight	Ionic radius (Å) State	CN6	CN8
Lanthanium	La	57	138.9055	3+	1.032	1.160
Cerium	Ce	58	140.1150	3+	1.010	1.143
				4+	0.870	0.970
Praseodymium	Pr	59	140.9077	3+	0.990	1.126
Neodymium	Nd	60	144.2400	3+	0.983	1.109
				2+		1.290
Samarium	Sm	62	150.3600	3+	0.958	1.079
				2+		1.270
Europium	Eu	63	151.9650	3+	0.947	1.066
				2+	1.170	1.250
Gadolinium	Gd	64	157.2500	3+	0.938	1.053
Terbium	Tb	65	158.9254	3+	0.923	1.040
				4+	0.760	0.880
Dysprosium	Dy	66	162.5000	3+	0.912	1.027
				2+	1.070	1.190
Holmium	Ho	67	164.9303	3+	0.901	1.015
Erbium	Er	68	167.2600	3+	0.890	1.004
Thulium	Tm	69	168.9342	3+	0.880	0.994
				2+	1.030	
Ytterbium	Yb	70	173.0400	3+	0.868	0.985
				2+	1.020	1.140
Lutetium	Lu	71	174.9670	3+	0.861	0.977

In nature, REE do not occur as free metals. They mostly occur in mineral structure in covalent or ionic bonding with various other REE and nonmetals. Monazite and xenotime are very common accessory minerals in granites and gneisses. These minerals are also very stable in near-surface environment. Due to their chemical resistance and high density, they are frequently concentrated in placer deposits. For this reason, placers are the major economic source of REE, while much smaller quantities are mined from primary ore deposits. Primary deposits include REE-bearing carbonatites such as Mountain Pass, California; the niobium mine at Araxa, Brazil, the baestnasite-bearing vein at Karonge southeast of Bujumbura in the Republic of Burundi, and the Mount Weld Rare Earth deposit in Western Australia. In many cases, they are exploited as by-product. For example, apatite for fertilizer manufacture can yield large amounts of REE, especially where apatite is associated with alkaline igneous rocks (as in America, Russia, Sweden) or REE-bearing clays (China). Various REE minerals such as allanite are produced as by-product of uranium mining (Canada). REE minerals of lesser importance include allanite (containing Ce and Y), zircon (Th, Y and Ce), euxenite and loparite (Neary and Highley, 1984).

1.2. The abundances of lanthanides in various reservoirs

When comparing concentrations of REE with other elements in various reservoirs, it becomes clear that the REE are actually abundant, although loosely called "rare earths". In the Earth's crust, each REE is more abundant than silver, gold or platinum. Cerium, yttrium, neodymium and lanthanum are more abundant than lead. As lithophile elements, REE preferentially partition into silicates and oxides, rather than metals or sulfide. They only appear as trace elements in many minerals, being dispersed in all reservoirs. It is rare to find high concentrations of REE in nature. They are usually incompatible during magmatic crystallization i.e. they concentrate in the melt during the magma evolution. But they are compatible if monazite, xenotime, allanide or zircon present in the melt.

Though REE tend to have similar geochemical characteristics in most geological environments, their abundances are not the same. REE with even atomic numbers (e.g. Ce, atomic number 58) are more abundant than those with odd atomic number. This feature is also found in chondritic meteorites, which were among the first objects formed from the solar nebula. REE with even atomic number were produced in higher abundance during nucleosynthesis because of their higher nuclear stability. This feature produces a “zigzag” effect in the plot of REE analysis. This is also called “Oddo-Harkins effect”, which can be normally eliminated by plotting REE analysis normalized to average abundances in a standard such as a chondritic meteorite (i.e. the concentration of each REE in the sample is divided by the concentration of the same REE in the reference material) (Table 1.2). Chondritic meteorites were the first choice, because they are thought to represent unaltered and unfractionated samples of the original composition of the solar system and they should therefore most clearly reproduce the abundance of the elements formed by nucleosynthesis at the beginning of the solar system. Thus, they are also thought to have the same chemical composition as the entire primitive Earth. Unfortunately the composition of chondritic meteorites is quite variable and chondrites with “chondritic” REE abundances are rather the exception than the rule (Boynton, 1984). This different composition of chondrites has given rise to a large number of sets of normalizing values for the REE and to-date a number of chondritic standards have been used and no fixed values have been adopted. “Average chondrite” and C1 chondrites are used very often, as they are thought to be the most representative of the composition of the original solar nebula. The X-Y plot often uses a logarithmic scale for the normalized abundance versus atomic number (or ionic radii) of the REE. This kind of plot is also called Masuda-Coryel diagram (Henderson, 1984) after the original proponents of the diagram (Masuda, 1962). This diagram allows determining the fractionation of any REE relative to the normalized standards.

Table 1.2. Rare earth element abundances in various geochemical reservoirs (in ppm, except when noted)

Elements	Solar (Si = 10^6)	Bulk earth	CI chondrite	Primitive mantle	Depleted mantle	Continental crust			Ocean crust			Average shale	Seawater (p.p.tr) (> 2500 m)	
						Upper	Total	Lower	Andesite	MORB	OIB		Atlantic Ocean	N.W. Pacific Ocean
	(1)	(2)	(3)	(4)	(5)	(6)	(7)	(8)	(9)	(10)	(11)	(12)	(13)	(14)
La	0.31	0.480	0.367	0.695	0.234	30.00	16.00	11.00	19.00	3.70	37	38.20	4.08	6.50
Ce	0.81	1.280	0.957	1.800	0.772	64.00	33.00	23.00	38.00	11.50	80	79.60	3.68	1.30
Pr	0.12	0.162	0.137	0.274	0.131	7.10	3.90	2.80	4.30	1.80	9.7	8.83	0.90	
Nd	0.39	0.870	0.711	1.340	0.713	26.00	16.00	12.70	16.00	10.00	38.5	33.90	3.61	4.30
Sm	0.14	0.260	0.231	0.436	0.27	4.50	3.50	3.17	3.70	3.30	10	5.55	0.71	0.80
Eu	0.10	0.100	0.087	0.165	0.107	0.88	1.10	1.17	1.10	1.30	3	1.08	0.13	0.21
Gd	0.30	0.370	0.306	0.584	0.395	3.80	3.30	3.13	3.60	4.60	7.62	4.66	1.13	1.30
Tb	-	0.067	0.058	0.107	0.075	0.64	0.60	0.59	0.64	0.87	1.05	0.77	0.18	
Dy	0.26	0.450	0.381	0.721	0.531	3.50	3.70	3.60	3.70	5.70	5.6	4.68	0.99	1.60
Ho	-	0.101	0.085	0.161	0.122	0.80	0.78	0.77	0.82	1.30	1.06	0.99	0.25	
Er	0.19	0.290	0.249	0.473	0.371	2.30	2.20	2.20	2.30	3.70	2.62	2.85	0.85	1.60
Tm	0.04	0.044	0.036	0.703	0.06	0.33	0.32	0.32	0.32	0.54	0.35	0.41	0.13	
Yb	0.20	0.290	0.248	0.475	0.401	2.20	2.20	2.20	2.20	3.70	2.16	2.82	0.85	1.40
Lu	0.13	0.049	0.038	0.072	0.063	0.32	0.30	0.29	0.30	0.56	0.03	0.43	0.16	

Data sources: (1) Ross and Aller (1976); Aller (1987); (2) Ganapathy and Andrers (1974); (3) McLennan (1999); (4) McDonough and Sun (1989); (5) (Salters and Stracke, 2004); (6), (7), (8), (9), (10) Taylor and McLennan (1985); (11) (Sun and McDonough, 1989); (12) values for PAAS, McLennan (1989); (13) Elderfield and Greaves (1982); (14) Taylor and McLennan (1988).

For most of the elements in the same group of the periodic table, the ionic radius increases as the atomic number increase. The REE provide an exception to this rule as the trivalent ions of these elements shrink steadily from the lightest rare earth La (1.16Å) to the heaviest one Lu (0.977 Å) (Table 1.1). This feature is called lanthanide contraction and occurs because the inner electron shell is build up rather than a new shell being added. This systematic variation from light REE to heavy REE causes significant differences in their abundances, behavior and partition coefficients. In nature, most of REE form stable 3+ ions of similar size, thus they have very similar chemical and physical properties. However, the progressive decrease in ionic size with increasing atomic number can cause the REE to be fractionated relatively to one another by a variety of geochemical and petrological processes. Because of their slightly larger sizes, LREE are generally more incompatible in common silicate minerals than the HREE.

Therefore, the ratio between LREE and HREE is not always the same for every reservoir and it can be used to determine the evolutionary histories of rocks. For example, primitive mantle has a chondritic LREE/HREE ratios. Depleted mantle has a LREE/HREE ratio less than chondritic, because during melt extraction, light REE are preferentially removed, while enriched mantle has greater LREE/HREE (McDonough and Frey, 1989) (Figure 1.1). In practice, La/Yb and Ce/Y are two common LREE/HREE ratios, which are used to determine the degree of fractionation of a REE pattern. Using the REE patterns in a wide variety of rocks and minerals can help to understand the effect of petrogenetic processes on REE abundances including fractionation and melting processes.

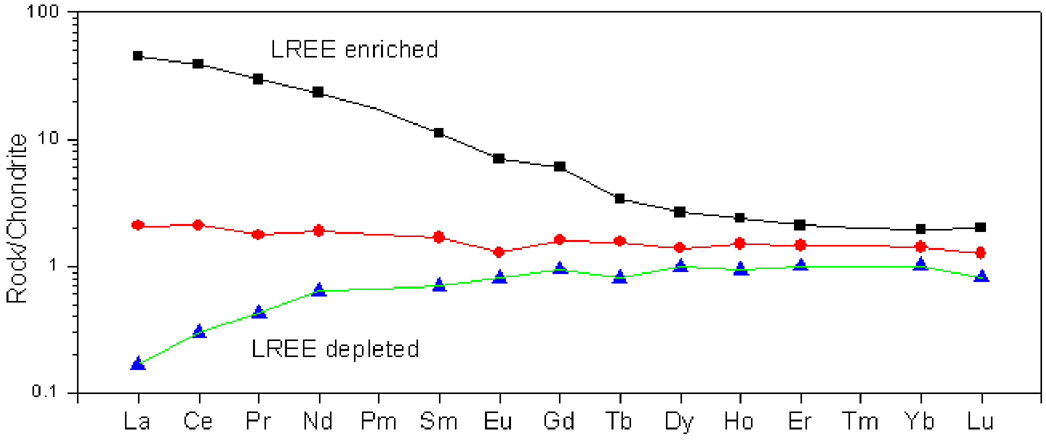

Figure 1.1.Schematic chondrite normalized diagram showing idealized REE patterns (Redrawn from Hollings and Wyman, 2004)

The relative abundance of REE in the solar system was estimated by analyzing the concentration of elements in carbonaceous chondrites and in the sun. Table 1.2 shows the results of the relative abundances (normalized to Si = 10^6) in the solar atmosphere as determined from spectral analysis (Ross and Aller, 1976).

As noted above, the REE abundance in the bulk Earth is believed to be roughly chondritic. Since during the formation of the metallic core, the REE partition almost completely into the silicate mantle (i.e. they are lithophile, not siderophile), the REE concentration in the primitive mantle or bulk silicate earth (BSE) is higher than in the bulk Earth, but the relative abundances in the primitive mantle are still chondritic. The precise values for the REE abundances in the bulk Earth and primitive mantle are somewhat model dependent, as they depend on the choice of chondritic material believed to be representative for the Earth.

The REE abundance in chondrites is quite variable both in absolute abundance and in ratios of elements depending on the samples and the precision of the analytical methods. Although the absolute values may vary by 10-15%, among which the values given in Table 1.2 are one of the most commonly used data sets, the relative abundances are essentially the same. Thus the normalized rare earth *pattern* should be the same regardless of normalizing values. More details can be found in Boynton (1984). REE patterns of sediments, surface and ocean water are usually similar to each other and to that of the continental crust.

1.3. REE in the mantle

Most of the present day upper mantle is depleted in trace elements, including REE, by partial melting and melt extraction which led to the formation of the continental and oceanic crust. The depleted mantle is more homogeneous than other mantle or crustal reservoirs. This reservoir is believed to be occupied by the upper mantle. However, there are some dissenters, most notably Anderson (Anderson et al., 1992) , who places the depleted mantle within the seismic transition zone.

The mantle plumes originate from some thermal boundary layer, such as the core-mantle boundary or the 660 km discontinuity. They appear to tap a different geochemical reservoir, which may either represent some primitive mantle or an enriched mantle source, i.e. a part of the mantle which has been chemically altered by the addition of silicate melts or fluids.

Abundances of rare earth elements in the upper mantle can be directly measured by studying samples of mantle rock that became exposed within the crust by geological processes. Using such data plus some assumptions, many authors have derived the absolute abundance of REE in the primitive mantle. For example, Sun and McDonough (1989) have calculated the absolute abundance of REE in the primitive mantle (Table 1.2) by assuming that: (i) the HREE contents of upper and lower mantle are similar, (ii) abundances of refractory lithophile elements in the mantle are in chondritic proportion, and (iii) the mantle Yb content is in the range of 0.45 to 0.5 ppm. The result implies that the primitive mantle is enriched in REE and all other refractory lithophile elements by a factor of 2.2±0.1 as compared to ordinary chondrites.

There is an agreement that the REE abundances in the bulk earth are similar to those of chondrite, i.e., the REE pattern of the bulk earth should be flat. Ideally, there are only two reservoirs, which contain a significant amount of REE, the crust and the mantle. Thus, if the crust is enriched in LREE, then the mantle should be depleted in LREE. The REE pattern in lower continental crust is relatively smooth, while there is a negative Eu anomaly in the upper continental crust. This anomaly is very common in continental crustal rocks; it is related to the retention of Eu as Eu^{2+} in residual plagioclase during partial melting, as will be discussed below.

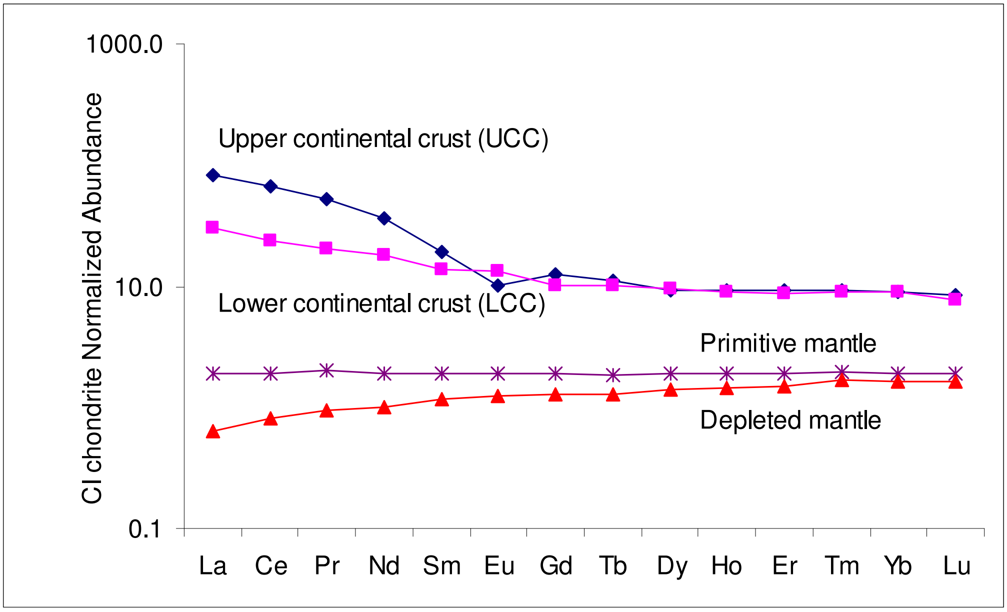

Figure 1.2. A rare earth plot showing rare earth patterns for primitive mantle (McDonough and Frey, 1989), lower continental crust (LCC), upper mantle crust (UCC) (Taylor and McLennan, 1985) and depleted mantle (Salters and Stracke, 2004)

Rare earth patterns for primitive mantle, depleted mantle, lower continental crust (LCC) and upper continental crust (UCC) are shown in Figure 1.2. The abundance of rare earth elements in the primitive mantle is higher than in the chondrites. This is due to the fact that the REE are lithophile, i.e. in equilibrium with a metal phase, they do not partition into the metal but into the coexisting silicates. Therefore, during the formation of core and mantle from a chondritic starting material, all the rare earth partitioned into the mantle.

Moreover, rare earth elements are incompatible, because their ionic radius is usually too large for them to fit easily into rock-forming minerals. This effect is particularly strong for the light rare earth elements, as they have the largest ionic radius. Therefore, upon melting, the rare earth partition into the melt phase and become depleted in the residual. This is the explanation why the crust is more enriched in rare earth than the primitive mantle and why the depleted mantle is depleted in rare earth compared to the primitive mantle.

1.4. The oxidation state of REE in geological systems

REEs are strongly electropositive and most of their chemistry is dominated by ionic bonding. Most of the REE are trivalent over a wide range of oxygen fugacity. The oxidation states +2 of Eu^{+2}, Sm^{+2} and Yb^{+2} can be seen at low oxygen fugacity. However, only Eu^{+2} appears to occur in nature (Morris and Haskin, 1974). The negative anomalies and the concentration of Yb in some inclusions in a carbonaceous chondrite were explained by the appearance of Yb^{+2}. However, this explanation seems not satisfactory, because Yb^{+2} requires extremely reducing conditions and alternative explanations are possible. The observed depletion may be due to the higher volatility of Yb as compared to other REE (Boynton, 1984). The presence of Sm^{+2} in minerals was first suggested by Goldschmidt (1954), but this hypothesis has not been substantiated and is unlikely. The oxidation state of +4 is known for Ce and Tb, but in natural system, only Ce can be partly or wholly in the +4 state. There is no record of the presence of Tb^{+4} in any mineral or natural aqueous system (Henderson, 1984).

Among the non-trivalent REE, Eu^{2+} and Ce^{4+} are the most important ones and they have been used a lot to model petrologic processes. Eu^{2+} only occurs at highly reducing condition. Its size is similar to Sr^{2+}, Ca^{2+} and Na^{+} while Eu^{3+} is much smaller. Therefore, Eu^{2+} easily substitutes for those elements particularly in plagioclase, resulting in anomalous REE distribution patterns. The anomalous Eu behavior in magmatic rocks is a sign of relatively shallow igneous processes, because plagioclase is stable only to about 40 km depth in the Earth crust. In contrast, Ce^{4+} requires oxidizing condition, which commonly occurs in secondary processes like weathering and early marine diagenesis. Under these conditions, Ce^{4+} dominates and tends to form highly insoluble hydroxide complexes that will fractionate Ce from other REE and therefore will cause anomalous REE patterns (McLennan, 1994).

1.5. Rare earth elements in basaltic systems

1.5.1. Partition coefficient

In basalt systems, most rare earth elements are dissolved in the common rock-forming minerals (olivine, pyroxenes, etc) and their concentrations can often be understood in terms of equilibrium thermodynamics. Partition coefficients (D) are thermodynamic variables that vary with pressure (*P*), temperature (*T*) and phase composition (*X*). Knowledge of variations in mineral-melt partition coefficients as a function of *P*, *T*, mineral and melt composition is therefore of great value in the interpretation and modeling of magma evolution processes, including partial melting, fractional crystallization, and assimilation coupled with fractional crystallization.

The partition coefficient of REE between minerals and melt can be defined in a simple way as the ratio of concentration of the element (E) in the mineral (α) divided by its concentration in the molten silicate melt (β) in equilibrium with that mineral.

$$\mathbf{D_{E,\alpha/\beta} = C(E_\alpha) / C(E_\beta)} \qquad \textbf{(Eq. 1. 1)}$$

where $D_{E,\alpha/\beta}$ is the Nernst partition coefficient, C (E_α) is the concentration of the element (E) in mineral and C (E_β) is its concentration in coexisting melt in ppm or wt%.

In literature, the term “distribution coefficient” and “partition coefficient” are often used interchangeably (McKay, 1989). Because the concentration of element E in the solid phase is normalized to its concentration in the melt, in the simplest case $D_{E,\alpha/\beta}$ will be independent on absolute concentration of element E. A mineral/melt partition coefficient ($D_{E,\alpha/\beta}$) of less than 1.0 implies that the concentration of the element in the mineral is less than in the coexisting melt; in this case, the element is called incompatible. $D_{E,\alpha/\beta}$ of 1.0 indicates that the element is equally distributed between the mineral and the melt. An element which is concentrated in the mineral as compared to the melt has $D_{E,\alpha/\beta}$ greater than 1.0 and is called compatible.

REE contents in minerals are usually very low in comparison with major elements, thus, they are entirely passive and have negligible influence on a particular process. However, they are complex functions of crystal composition, melt structure and composition, temperature, defect equilibria, oxygen fugacity, pressure, and kinetic effects, leading to the great number of published data for partition coefficient. The behavior of REE is very sensitive to the presence or absence of particular phases, which may vary with depth. Partial melting has strong effects on REE concentrations. It is likely that much of the incompatible element variations observed in magmas and magmatic rocks are related to variations in the degree of melting. For example, LREEs are incompatible in garnet, whereas HREEs are more compatible and preferentially enter the garnet structure. This can be useful in determining whether the melt generation took place in the presence of a garnet phase or not. This can also help in determining the depth of the melting. The presence of garnet in the residue causes a strong HREE depletion and LREE enrichment of the melt.

In general, several workers have recently developed predictive models for D-values. These models are based on either natural observations or experimental data, and are either empirical (McKay, 1989), theoretical (Van Westrenen et al., 2000), or a combination of both (Wood and Blundy 1997).

1.5.2. REE in different basaltic setting

Basalt is the most common rock type in the Earth's oceanic crust. In fact, most of the ocean floor is made of basalt and huge outpourings of lava called "flood basalts" are found on the surface of many continents. Basaltic magma is commonly produced by direct melting of the Earth's mantle. Thus, the internal differentiation history of the mantle can be ascertained from studies of the chemical signature brought to the surface by melts. It is important to note that the rare earth patterns in the two most common types of basalts, mid-ocean-ridge basalt (MORB) and ocean-island basalt (OIB) are distinctly different. This reflects the sources of the parental magmas, the extent of partial melting and petrogenetic processes associated with melt formation and magma evolution. This section briefly reviews the systematic of REE in these basalts.

1.5.2.1 Mid-Ocean Ridge Basalts (MORB)

In general, MORB melts are thought to be formed at shallow depth beneath a ridge axis by anhydrous decompression melting. Initial melting may appear at depth of 60-80 km, and segregation occurs at about 20 km (Hollings and Wyman, 2004). The normalized REE patterns are smooth and characterized by LREE depleted patterns with general unfractionated HREE (Figure 1.3). The LREE depletion result from the fact that the MORB originates from a depleted upper mantle, i.e. a part of the mantle that has already seen melts extraction before.

MORB basalts are mainly olivine tholeiites with a narrow range of major element composition. The variation of major and trace element reflect the degree of partial melting and magma fractionation and the existence of mantle heterogeneities.

The most common MORB is normal MORB (N-MORB), which is known to be derived from mantle source that is depleted in the most incompatible elements. Holling and Wyman (2004) noted that, other kinds of MORB are enriched in incompatible elements and radiogenic isotopes. Their REE abundance and incompatible element composition are transitional from plume MORB (P-MORB), transitional MORB (T-MORB) and enriched MORB (E-MORB) to that of ocean island basalts (OIB). The REE pattern of E-MORB is almost the same as that of OIB, which is explained by the mix of depleted MORB mantle and an enriched OIB like source.

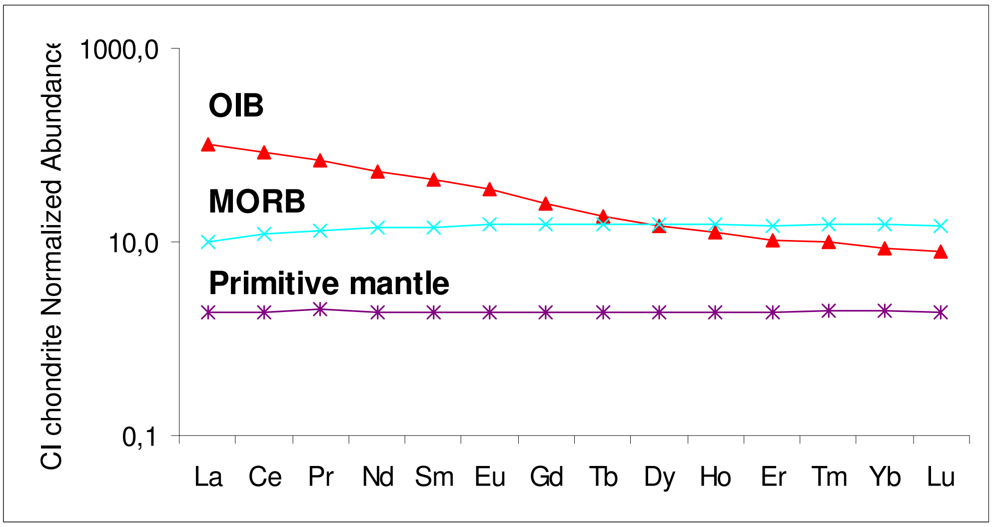

Figure 1.3. A rare earth plot showing rare earth patterns for ocean island basalt (OIB) (Sun and McDonough, 1989) and mid ocean ridge basalt (MORB) (Taylor and McLennan, 1985)

1.5.2.2 Ocean island basalts (OIB)

It is generally accepted that OIBs are derived from mantle plumes. They can be either tholeiitic or alkalic and are generated by partial melting of multi-component sources including: High-μ (HIMU) recycled ocean crust; enriched mantle near primitive mantel (EM1); enriched mantle recycled lithosphere (EM2) and depleted MORB mantle (DMM). The tholeiitic OIB represent a greater degree of partial melting (20-30%) than the alkaline OIB (5-15%) (Wilson, 1989). OIB is typically LREE enriched compared to N-MORB, likely as a result of their deviation from mixture of DMM with HIMU, EM1 and EM2 sources.

The wide range of fluctuations of REE and other trace elements seen in the OIB when compared with the much more homogeneous N-MORB suggests that the upper layer of the mantle is better mixed than the composition of the lower layer.

1.6. REE partition coefficient patterns for some major basaltic minerals

Shapes of the partition coefficients patterns of the major minerals involved in basalts petrogenesis are illustrated in Figure 1.4.

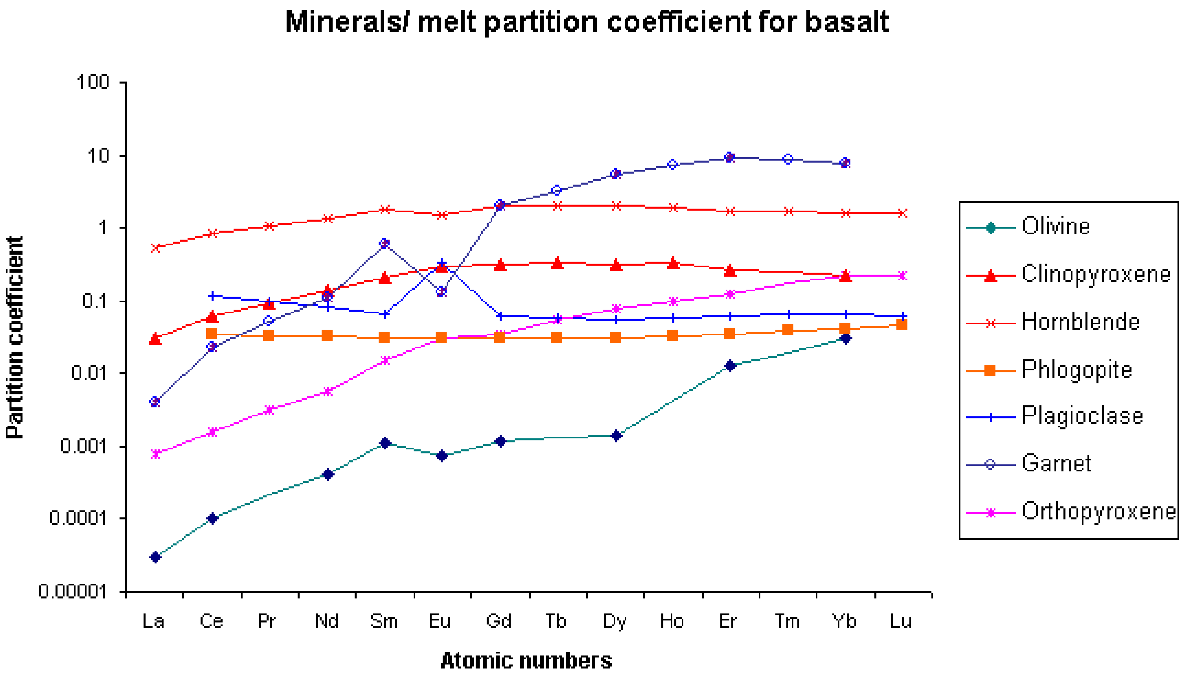

Figure 1.4. Rare earth elements patterns of some major mineral in basalts melts. Data sources: Olivine: Kennedy et al. (1993); Orthopyroxene and Clinopyroxene: Green, T. H. et al. (2000); Hornblende: Fujimaki et at (1984); Phlogopite and Plagioclas: Arth (1976); Garnet: Barth et al. (1997)

In general, europium anomalies are chiefly controlled by the appearances of plagioclase. Eu is compatible in plagioclase as Eu^{2+} and tends to substitute for calcium in the plagioclase structure, in contrast to the trivalent REE, which are incompatible. The D-values of REE for plagioclase are generally low, except for Eu, thus the fractionation of plagioclase has no strong effect on the trivalent REE. The pattern drops from LREE to HREE with a positive Eu anomaly (McKay, 1989).

In basaltic systems, REE are incompatible in most of the major minerals like olivine, orthopyroxene and clinopyroxene with a small fractionation of LREE relative to the heavy ones. Partition coefficients increase usually by about an order of magnitude from La to Lu. An extreme depletion of the HREE relates to the present of garnet in the source. Hornblende has some and phlogopite has little effect on the relative fractionation of REE.

1.6.1. Olivine

Olivine is one of the most abundance rock-forming minerals, and plays a key role in controlling the fractionation of the compatible elements, but is unimportant in the fractionation of incompatible elements because of its very low partition coefficients (Beattie, 1994).

In the last decades, a number of studies were conducted to investigate the partition coefficient of rare earth elements between olivine and silicate melts in natural samples by analyzing phenocrysts-matrix pairs (Fujimaki et al., 1984; Higuchi and Nagasawa, 1969; Philpotts and Schnetzler, 1970), including some studies under controlled conditions (see review by Green, 1994; Wood and Blundy, 2004).

McKay (1986) measured Nd, Sm, Gd and Yb olivine/synthetic basaltic melts partition coefficient at log fO_2 0.5 unit above the iron-wustite buffer on synthetic lunar mare and highland basalts. The values for the light REE are much lower than those from previous experiment or phenocryst/matrix studies and showed two orders of magnitude increase in partition coefficient from Nd to Yb. Kennedy et al. (1993) carried out experiments on lanthanide partitioning between olivine and melt at atmospheric pressure; oxygen fugacity was fixed at half a log unit below the iron-wustite buffer curve. Beattie (1994) measured olivine/melt partition coefficient for 7 REE in several terrestrial lavas, a komatiite, two kimberlites and three basalts. In these experiments oxygen fugacity was maintained approximately at the NNO buffer. Taura et al. (1998) used secondary-ion mass spectrometry and electron microprobe to study the partition coefficient of only La and Ce between olivine and melt at upper mantle condition, 3 to 14 GPa. At this condition, the partition coefficients of REE tend to be somewhat elevated, and decrease from La to Ce. Because there are only data for La and Ce available, it is impossible to reconstruct the general patterns of all REE. The partition coefficients of REE generally increase with atomic number, and olivines are strongly LREE depleted. However, the partition coefficient values, in general, are very low, so that olivine is not capable of producing significant REE fractionation during magma evolution.

Olivine has two octahedral (sixfold) sites (M1 and M2), but the partitioning of trivalent REE into olivine is preferentially into M1 position. In most cases, charge balance is maintained by a coupled substitution of REE^{3+} for Mg^{2+} and Al^{3+} for Si^{4+} (Beattie, 1994).

1.6.2. Clinopyroxene

Extensive studies on REE partitioning between (D_{REE}) clinopyroxene and silicate melts both from natural samples and experimental ones are increasingly well understood (Wood and Blundy, 1997; 2004) and revealed that partitioning is a complex function of pressure (P), temperature (T) and phase composition. Lattice strain theory is the most applicable model to predict the partitioning of REE between clinopyroxene and silicate melt for a wide range of composition, water content and physical condition. The effects of such factors on D_{REE} were considered in many experimental studies at pressures from 0.5 to 7.5 GPa and temperatures from 1000 to 1290°C (Hack et al., 1994).

In general, D_{REE} between clinopyroxene and melt are very low and have smooth patterns, in which D-values in the LREE part increase steeply from La to Eu, whereas in the HREE apart from Eu to Lu, the pattern is relatively constant. D_{REE} has positive correlations with Ca concentration in pyroxene, and Al concentration in pyroxene and melts. D_{REE} varies by over a factor of 2 for any given bulk composition, and by up to a factor of 10 over the range of compositions from alkali basalt to island arc basalts to mid-ocean ridge basalt (Hack et al., 1994). D_{REE} slightly increases with decreasing temperature, except D_{Lu} that shows a small but consistent increase as temperature increases from 1050 to 1200 ^{o}C. D_{REE} has positive correlation with pressure for clinopyroxene from relatively silica rich composition (Green and Pearson, 1985), but has negative correlation with pressure for clinopyroxene from basalts (Adam et al., 1994; 2003; Dunn, 1987). These correlations between partition coefficient and pressure may be related to changes in site volumes and electrostatic potentials accompanying shifts in the relative concentrations of Al^{IV} and Na.

At high and constant pressure, D_{REE} is also controlled by water content of the melt. The effect of water on clinopyroxene-melt partition coefficient overwhelms the effect of temperature. This leads to increasing fractionation of light from heavy REE compared to anhydrous experiments (Green et al., 2000). The effect of H_2O on the activities of D_{REE} does not depend on the composition of the clinopyroxene, but increase in water content leads to substantial decreases in REE partition coefficients (Wood and Blundy, 2002).

1.6.3. Orthopyroxene

A number of researchers have measured the REE partition coefficient (D_{REE}) between orthopyroxene and coexisting melt under controlled conditions (Colson et al., 1988; Kennedy et al., 1993; McKay et al., 1986; Nielsen et al., 1992). Although the experiments were conducted under different conditions and on different bulk composition, the results are generally in good agreement. D_{REE} depends on the Fe/Mg ratio. It is supposed to be controlled by composition in the combined data sets as well as other physical parameters (Colson et al., 1988; McKay, 1986). At temperatures from 1050 – 1400^{o}C, McKay (1986) and Nielsen et al. (1992) found a strong correlation between D_{REE} and wollastonite content of pyroxene, but the trends are not identical. The D_{REE} from McKay (1986) is lower at given Ca content than the result of Nielsen et al. (1992). This was explained by the effect of different experimental conditions, melt composition or the precision of the analytical instrument. In general, however, D_{REE} increase as a function of Ca content in the pyroxene.

The D_{REE} between orthopyroxene and melt are similar to olivine and are also very low. However, in contrast to clinopyroxene, this pattern is steep and smoother, increasing from La to Lu as illustrated in Figure 1.4, including a strong fractionation of $D_{Lu}/D_{La} = 250$, and from D_{Gd} to D_{Lu} a sloping pattern with $D_{Gd}/D_{Lu} = 6.6$ as compared to the flat D_{Gd} to D_{Lu} pattern for clinopyroxene (Green et al., 2000).

1.6.4. Garnet

Garnets are groups of minerals having similar physical and crystalline properties. They have general formula $X_3Y_2(SiO_4)_3$, where X represents divalent ions such as calcium, magnesium, ferrous iron, or manganese, and Y represents trivalent ions such as aluminum, ferric iron, or chromium, or in rare instances, titanium. REE prefer entering the dodecahedral X-sites by substituting Ca, Mg or Fe.

The role of garnet in the generation of mid-ocean ridge and ocean island basalts (MORB and OIB) is controversial. Rare earth element (REE) concentrations in basalt appear to require the presence of at least some garnet in the source of MORB and OIB (Frey et al., 1993; MacKenzie and Canil, 1999; Shen and Forsyth, 1995).

In general, D_{REE} garnet/melt patterns resulting from all experiments are smooth and are quite steep upwards from La to Lu with the LREE being incompatible and the HREE being compatible (Figure 1.4). Thus, the presence of garnet in the melt can cause extreme depletion of HREE relative to the LREE because the distribution coefficient for Lu is 1000 time greater than for La for basaltic magma. Therefore, a small degree of melting or a garnetiferous residue may produce magmas with fractionated REE patterns. An important implication is that two compositionally similar source regions, undergoing similar degrees of melting, may produce magmas of different composition because of differing mineral stabilities in the zone of partial melting. The thickness of overlying crust plays an important role in defining the composition of mantle melts because of the control exerted on the depth of melting (e.g. above or within the garnet stability field).

When the experiments were carried out at oxidized condition, D_{REE} garnet/melt patterns showed no discernable Eu anomaly, whereas, at more reducing condition, for example, D_{REE} garnet/melt patterns for pyrope garnet commonly showed a little negative Eu anomaly.

At different pressure-temperature conditions, Barth et al. (1997) showed that D_{REE} of garnet increase significantly with decreasing temperature; the La/Yb ratio decreases with decreasing temperature. At melting experiments under pressures ranging from 3 to 7 GPa. Shimizu et al. (1997) showed that HREE compatibility decreases with increasing pressure. The garnet partition coefficients most applicable to lherzolite melting are significantly higher than those from previous studies (Salters and Longhi, 1999).

1.6.5. Plagioclase

The most widely quoted example of the control of oxidation state on the behavior of REE is that of the partitioning of Eu between plagioclase and a basaltic melt (Drake and Weill, 1975). The partition coefficient for Eu between atmospheric condition and the relative reducing conditions found in natural basalts is quite different. This is because europium forms Eu^{2+} at reduced conditions while Eu^{3+} is stabilized at oxidizing conditions. Eu^{2+} is much more compatible than Eu^{3+} in plagioclase, thus at reduced conditions, the partition coefficient of europium between plagioclase and basaltic melt is high (generally above 1), whereas at oxidized conditions the partition coefficient for europium is low, and similar to other REE (Figure 1.5). In lunar basalt, Eu^{2+} dominates, while in terrestrial basalts Eu^{2+} and Eu^{3+} are of comparable abundance (Hess, 1989).

Eu^{2+} is compatible in plagioclase, while other trivalent REE are incompatible. This leads to the enrichment of trivalent REE in the melt and depletes the melt of Eu^{2+} during the fractionation of plagioclase, creating a negative europium anomaly in the chondrite-normalized REE pattern of the partial melt and a positive anomaly in the crystalline residuum (Figure 1.6).

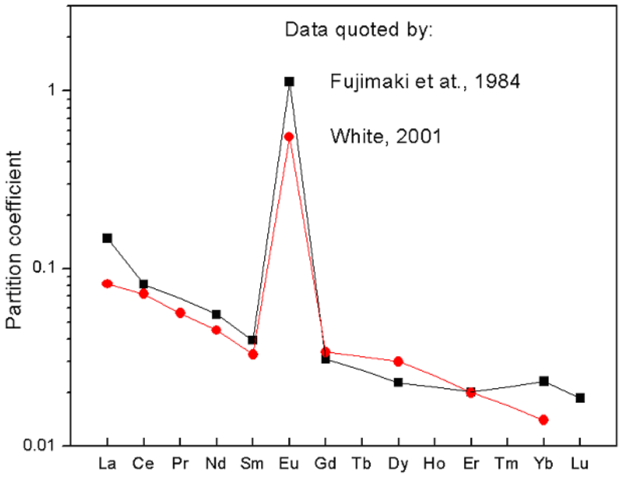

Figure 1.5. Plot of the partition coefficient for REE between plagioclase and melt (log scale vs. atomic number)

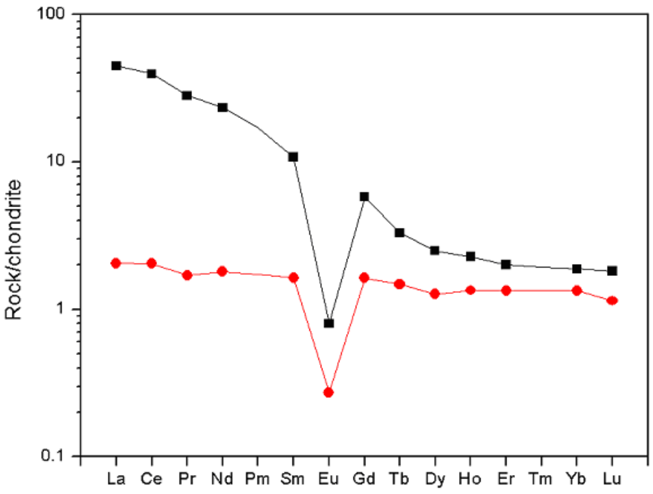

Figure 1.6. Chondrite normalized diagram showing negative Eu anomalies characteristic of plagioclase fractionation (Hollings and Wyman, 2004)

The partition coefficient of Eu^{3+} can be calculated by interpolation from two neighboring elements Sm^{3+} and Gd^{3+}. This can be used to calculate the Eu^{2+}/Eu^{3+} ratio in each phase, where the behavior of Eu^{2+} and Eu^{3+} is quite different and varies with oxygen fugacity.

1.7. Rare earth elements in granitic systems

1.7.1. Distribution of REE in granitic rocks

Many hydrothermal and pegmatitic ore deposits are closely associated with granites. They provide the most important source for metals such as copper, silver, tin, tungsten and molybdenum etc. In some of these deposits, ore metals are enriched more than one million times relative to their average content in the Earth's crust. This enrichment is usually a result of source enrichment, magmatic fractionation and sometimes the separation of a free fluid phase. Searching for new ore deposits in the field requires a solid understanding of these processes and the ability to reconstruct the fractionation path of a granitic magma from field relationships and geochemical data.

All of the REE have been commonly considered to be incompatible, i.e. they preferentially partition into magmatic liquid relative to the coexisting crystalline assemblage, and thus crystal fractionation should result in progressive enrichment of those elements in the remaining melt. The exception is that heavy rare earth elements behave as compatible elements in cases where garnet or amphibole appears as important constituents of the solid assemblage. In felsic igneous rocks, some studies have shown that LREE concentration decreases rapidly during differentiation, suggesting that the REE are not incompatible; rather, their abundance is controlled by the separation of some LREE bearing accessories minerals (Miller and Mittlefehld, 1982).

In granite, most of the rare earth elements are not in the common rock-forming minerals (feldspars, micas, etc), rather they are contained in tiny traces of accessory minerals. Thus the geochemical behavior of REEs is controlled by the solubility of these accessory minerals like zircon, monazite, apatite, allanite, xenotime, thorite, and huttonite (Seydoux et al., 2002). During crystallization, REE behavior is controlled by the nature of the crystallizing accessories, the kinetics of nucleation and crystal growth, and the dynamics of solid melt segregation. During partial melting, REE concentration in melts is controlled by the solubility, solution kinetics, and accessibility of the accessories to the melt. Understanding that process can help to reconstruct the origin and fractionation of granitic magmas from trace element abundances measured in natural samples. This is obviously something of great importance for understanding the origin of economic ore deposits. A main focus of the present study will be on rare earth elements and the behavior of accessory minerals such as monazite and xenotime. Both monazite and xenotime often control the concentration of rare earth element during the fractionation of granite.

Monazite and xenotime are the most common accessory minerals in both peralumious granitoids, intermediate to high grade metapelictic rocks and in some hydrothermal veins (Franz et al., 1996; Nabelek and Glascock, 1995; Zhu and O'Nions, 1999) and they are the main accessory minerals controlling the behavior of REE, U and Th during the formation and differentiation in peraluminous granites (Mittlefehld and Miller C.F., 1983).

Despite their generally minor occurrence and small crystal size, monazite and xenotime are nevertheless of outstanding geological importance. Firstly, monazite and xenotime have proved to be a valuable chronometer for many geological processes (Zhu and O'Nions, 1999) such as metamorphism (Parrish, 1990; Zhu et al., 1997), magmatism (Harrison et al., 2002) sedimentation (Evans and Zalasiewicz, 1996) and mineralisation (Wang et al., 1994). Secondly, monazite and xenotime may significantly affect or even dominate the light and heavy REE budget of the host rock (Bea et al., 1994;Bea, 1996). Thirdly, monazite and xenotime occur as important REE bearing ore minerals in a variety of sub-economic to economic REE deposits of possible hydrothermal origin such as Lemhi Pass, Idaho/Montana (Anderson, 1961), Bayan Obo, China (Chao et al., 1992), Olympic Dam, Australia (Oreskes and Einaudi, 1990), and Steenkampskraal, South Africa (Andreoli et al., 1994). Fourthly, their behavior puts important constraints on integrated models for petrogenesis. This is particularly true for intermediate to high silica granite suite in which REE abundance decreases with the increasing index of differentiation (Evans and Hanson, 1993). They are also a primary host of thorium, which could be used as a replacement for uranium in nuclear power generation. The REE phosphates have also been proposed as hosts for nuclear waste disposal owing to their physical and chemical durability, ability to resist metamictization, and capacity to contain actinides (Boatner et al., 1981; Boatner et al., 2002; Ewing et al., 2002). In addition, the geochemistry of monazite and xenotime is important for models of metallogenesis and mineral exploration for various types of hydrothermal ore deposits (Cetiner et al., 2005; Fryer and Taylor, 1987; Lottermoser, 1992; Plimer et al., 1991).

1.7.2. Crystal structure of monazite and xenotime

In general, pure rare earth element phosphate crystals are assumed to form in two structure types: (1) Monazite, which has the formula $REE(PO_4)$, and is light rare earth elements (LREE) selective i.e. it prefers elements with ionic radii between La (1.16 Å) and Gd (1.053), and (2) xenotime, which has the simplified formula YPO_4, and is heavy rare earth elements (HREE) selective i.e. it incorporates elements between Tb (1.04 Å) and Lu (0.977 Å) (Franz et al., 1996; Heinrich et al., 1997; Ni et al., 1995;Rapp and Watson, 1986). However, the boundary between the two structures (usually between $GdPO_4$ and $TbPO_4$) depends strongly on the condition of formation, mainly on temperature and the properties of the precursor material. At temperatures above 1000°C, $TbPO_4$ of monazite structure type slowly transforms into the xenotime structure. Flux growth of $GdPO_4$ resulted in both monazite and xenotime. At temperatures of 800-1400°C, the monazite structure dominates, whereas at 1600-1700°C, the xenotime structure is favoured (Kolitsch and Holtstam, 2004). The transition from monazite to xenotime structure occurs between Gd and Tb at condition of 25°C and 1 bar (Ni et al., 1995).

Monazite is monoclinic, a = 6.79, b = 7.01, c = 6.46, β = 104.4°, Z = 4 with space group *P2₁/n* and point group *2/m* and has a ninefold coordination for the REE. Crystals are usually small, tabular, or prismatic, often forming granular masses. Xenotime is tetragonal, with space group *I4₁/amd* and is isostructural with zircon and thorite, which is the dimorph of huttonite. Both atomic arrangements are based on [001] chains of alternative edge-sharing phosphate tetrahedra and REE polyhedra, with a $REEO_8$ polyhedron in xenotime and a $REEO_9$ polyhedron in monazite (Figure 1.7). Monazite is isostructural with crocoite, $PbCrO_4$ and huttonite ($ThSiO_4$). Both monazite and xenotime show a linear correlation between cell volume and ionic radious of their respective REE (Gratz and Heinrich, 1997). The biggest cell volume of the monazite suite is 305.7$Å^3$ ($LaPO_4$) and gradually decreases to 279.1 $Å^3$ ($GdPO_4$) as the ionic radii decrease from La to Gd, while the biggest cell volume of the xenotime suite decreases from 291.1 $Å^3$ ($TbPO_4$) to 273.6 $Å^3$ ($LuPO_4$) as the radii decrease from Tb to Lu (Figure 1.8).

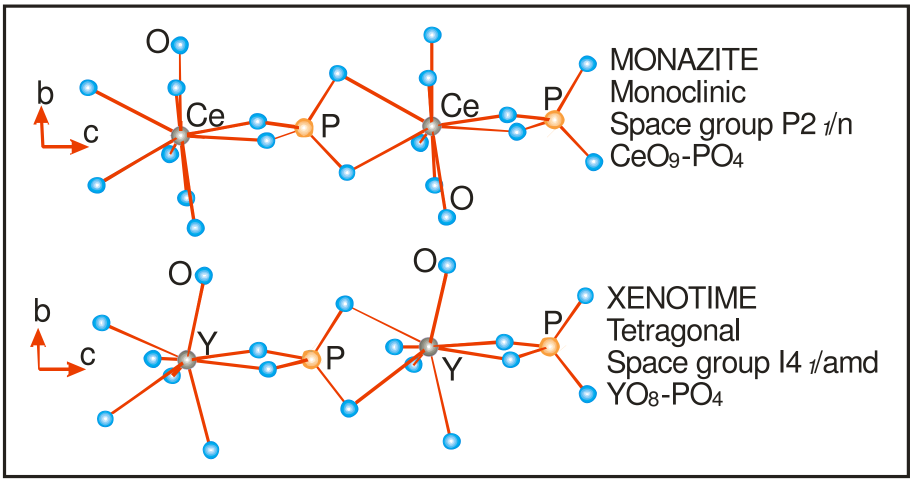

Figure 1.7. Typical monazite ($CePO_4$) and xenotime (YPO_4) structure. Both arrangements are based on [001] chains of alternating phosphate tetrahedra and $REEO_8$ polyhedra in xenotime or $REEO_9$ polyhedra in monazite (Modified after Taylor and Ewing, 1978)

In nature, there is no pure single rare earth element monazite. Rather, monazite is a solid solution including all of the rare earths, but Ce, La and Th are usually the dominant large cations. The three most common monazite types are distinguished as monazite-Ce {(Ce, La, Nd, Th, Y)PO_4}, monazite-La {(La, Ce, Nd)PO_4} and monazite-Nd {(Nd, La, Ce)PO_4}. Silica or SiO_4, is often present in natural monazite replacing a small percentage of the phosphate groups. Uranium is also a trace element in some specimens. Like in monazite, Y in xenotime also can be replaced by other REE or uranium and thorium to form a solid solution series.

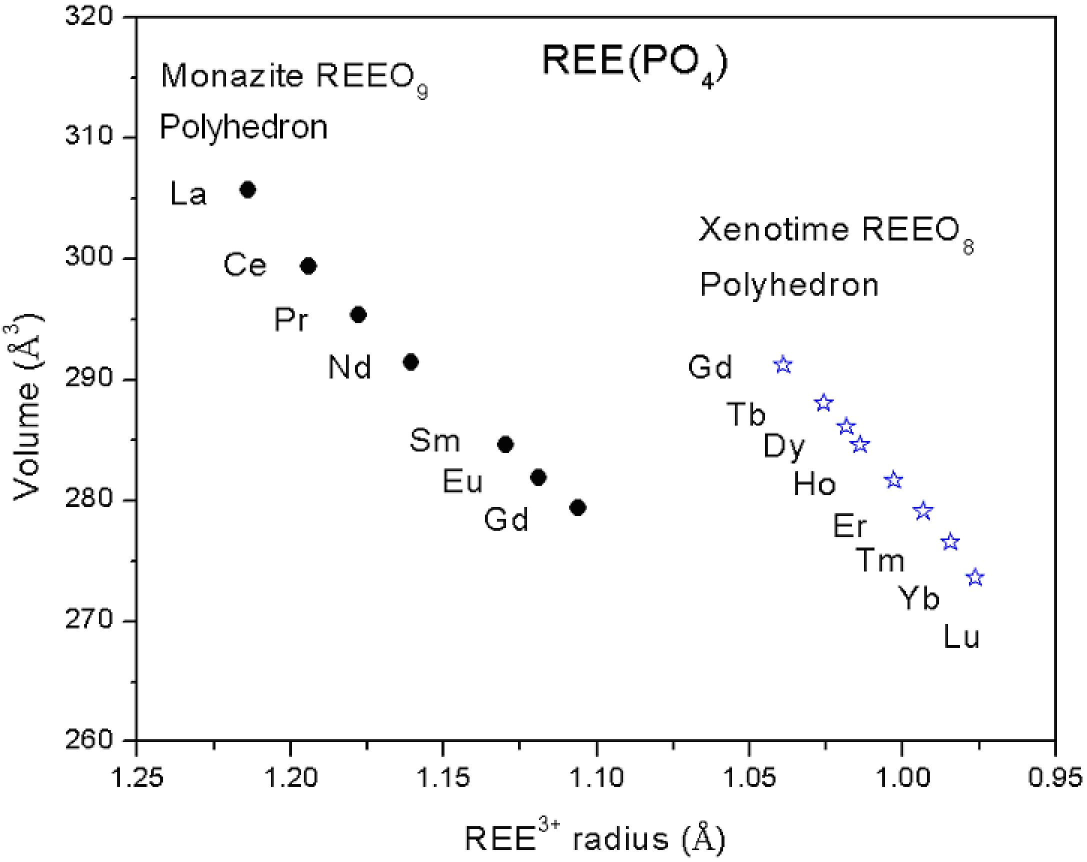

Figure 1.8. Unit-Cell volume of pure REE(PO_4) vs. REE ionic radii (Redrawn from Gratz and Heinrich, 1997)

1.7.3. Monazite and xenotime solubility in granitic melts

The solubility of monazite and xenotime in granite melt has been investigated in a number of dissolution experiments (see reviews by Johannes and Holtz, 1996; Linnen and Cuney, 2004). The procedures were designed as either direct or reversed experiments. The first one examines the dissolution of monazite/xenotime crystals in a granitic melt, while the latter investigates the solubility of REE in a melt by crystallizing monazite/xenotime from REE- and PO_4 doped melt. The result from both procedures allows evaluating the attainment of equilibrium. All the previous experiments were carried out in hydrous melt (1-6 wt% H_2O) at a wide range of temperature and pressure. Montel (1986, 1987, 1993) examined the effect of melt composition on the solubility of pure synthetic Ce-monazite in hydrous saturated $SiO_2 – Al_2O_3 – K_2O – Na_2O$ melts (containing 6 wt% H_2O) mainly at 800 °C and 2 kbar. Some experiments were carried out at temperatures between 800 and 1000°C. ASI (Al/Na+K) in mol of melt composition varied from 0.51 to 1.11 and (Na/K) ratio changes from 1.56 to 2.74, i.e. most of the experiments were performed with peralkaline compositions. Rapp and Watson (1986) used natural monazite {(Ce, La, Nd, Pr, Sm, Gd, Eu, Th)PO_4} and a natural Ca- Fe- and Mg- poor obsidian melt (Lake Country obsidian) and Rapp et al. (1987) used natural Ca- Fe- and Mg- rich obsidian melt as the starting material for the experiments to study the solubility of monazite in felsic melts. Runs were carried out in a piston cylinder apparatus at 8 kbar over a temperature range of 1000-1400°C, and a wide range of water contents (1-6 wt % H_2O). These were partial dissolution experiments in a short time (4 hours to 2 weeks), in which the REE diffused gradually from crystal into melt as a function of time, temperature and distance. The saturation level was thought to be at the interface between crystals and melt, and was calculated from the gradient of concentration in the glass around the crystals. Wolf and London (1995) studied the relative solubility of apatite, monazite and xenotime in peraluminous granitic melt at 750°C and 2 kbar. Natural apatite $\{Ca_5(PO_4)_3\}$ (with 1.4 wt% REE_2O_3), monazite $\{(Ce, Nd, Sm, Gd)(PO_4)\}$ and xenotime $\{(Y, Dy, Yb, Er)(PO_4)\}$ were mixed with Ca-free haplogranite. The initial composition has ASI ranging from 1.05 to 1.2 and projects slightly to the feldspar side of the 2 kbar, water saturated minimum haplogranite (Tuttle and Bowen, 1958). Under conditions of 800°C and 2 kbar, Keppler (1993) investigated the role of F on the solubility of some rare earth phosphate crystals ($LaPO_4$, $GdPO_4$ and $YbPO_4$) in $SiO_2 – Al_2O_3 – K_2O – Na_2O$ melt with the ASI equal to 1.

In spite of various experimental techniques and conditions, the results have shown that the solubility of monazite/xenotime in the melt mainly depends on: (1) the temperature, (2) the melt composition (3) the water content, and may be (4) other volatile or non-metallic elements including P, F, Cl, etc. Pressure has little effect on the solubility of monazite/xenotime in melt.

Figure 1.9, adapted from Johannes and Holtz (1996) and/or Montel (1993) illustrates the temperature dependence of monazite solubility. However, the diagram also shows some of the original data by Rapp and Watson (1986), which were arbitrarily excluded from the plot of Johannes and Holtz and which do not fall on their regression line.

The most important compositional parameter controlling monazite solubility in a felsic melt is the aluminum saturation index (ASI). ASI can be defined as the molar ratio $Al_2O_3/(Na_2O + K_2O)$ or, for a Ca-bearing granite, as $Al_2O_3/(CaO + Na_2O + K_2O)$. Granites are classified according to ASI as: (1) peralkaline (ASI < 1); (2) metaluminous (ASI closes to 1 and $[Na_2O+K_2O] < [Al_2O_3] < [CaO+Na_2O+K_2O]$) and (3) peraluminous (ASI> 1 for Ca-bearing granite or ASI > 1.15 for high P rare element granite) (Linnen and Cuney, 2004). Peralkaline granites are characterized by very high concentration of REE, up to thousands ppm. Peraluminous granites contain extremely low REE concentrations, even lower than the average upper crustal abundance. Most of the rare-element granites contain only few ppm REE or less (Linnen and Cuney, 2004). This is in agreement with the experimental results that monazite/xenotime solubility in water-saturated haplogranite melt depends strongly on the melt composition, ranging from >1000 ppm in strongly peralkaline composition to few hundred ppm for high-silica peraluminous composition at >800°C and 2 kbar to only few tens ppm for low temperature peraluminous granite (see Figure 1.10). While monazite solubility increases strongly with peralkalinity, there is no difference in monazite solubility between sub-alkaline and sub-aluminous melts.

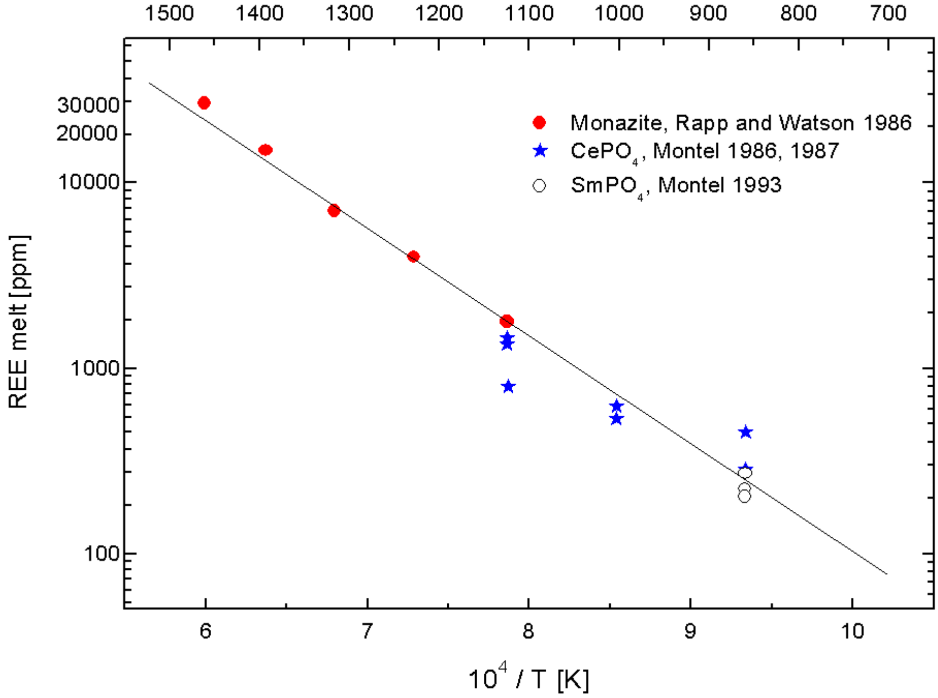

Figure 1.9. Solubility of monazite (expressed as REE concentration of melt in ppm) in felsic melts (almost subaluminous compositions) containing approximately 6 wt% H_2O (Modified after Montel et al., 1993)

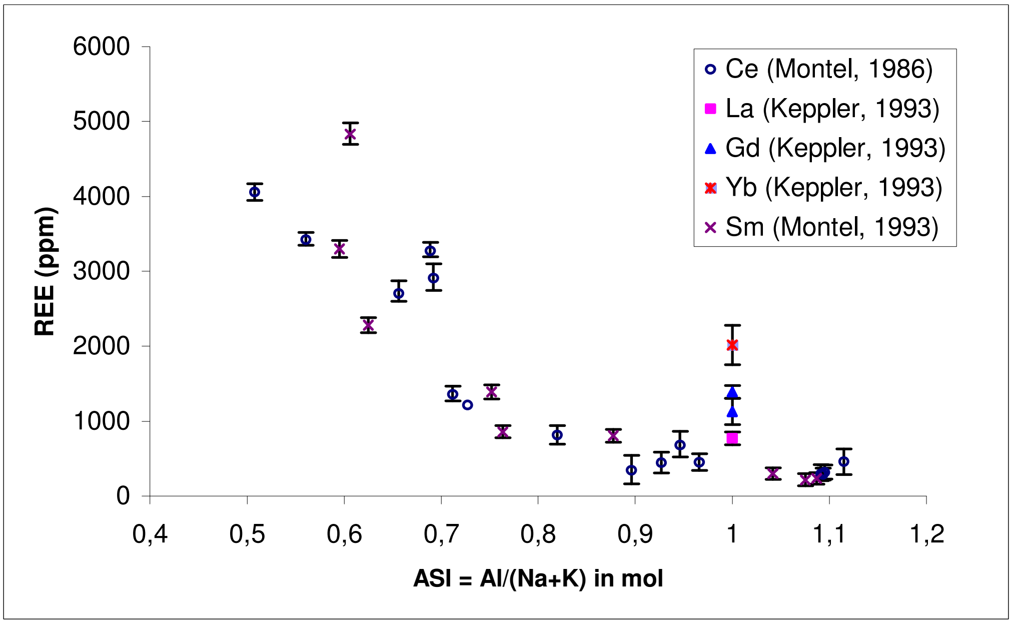

Figure 1.10. Solubility of REE(PO_4) crystals at 800°C, 2 kbar, under water-saturated conditions, in SiO_2-$A1_20_3$-Na_2O-K_20 melts

Water also has some effect on monazite solubility. According to Rapp and Watson (1986), increasing the water content of the granite melt from 1 to 6 wt. % approximately doubles monazite solubility. On the other hand, Keppler (1993) found no significant effect of fluorine on the solubility of $LaPO_4$, $GdPO_4$ und $YbPO_4$ in a water-saturated haplogranitic melt at 800 °C and 2 kbar.

The effect of phosphorus on monazite solubility has never been explicitely studied, despite the fact that phosphorus should, according to the law of mass action, reduce REE solubility, if the REE phosphates dissociate in the melt at least partially into REE^{3+} and phosphate. This effect could be quite important, as phosphorus concentrations in granites are quite variable. Highly fractionated granites contain 0.2-0.5 wt% P_2O_5 (Breiter et al., 1997; Manning and Pichavant, 1988), and extremely high contents (up to 1-2.5 wt %) are reached in some final fractionated granite systems like dyke granite or pegmatite (Breiter et al., 1997; London et al., 1999). By contrast, P_2O_5 is known to be dramatically lower in Ca-bearing melt, because of the formation of apatite (Pichavant et al., 1992).

Montel (1993) proposed the equation below to estimate the solubility of monazite as a function of temperature, water content and anhydrous composition of the melt.

$$\ln(REE_t) = 9.5 + 2.34D + 0.3879\sqrt{H_2O} - \frac{13318}{T} \qquad \textbf{(Eq. 1. 2)}$$

Where $REE_t = \sum \frac{REE_i(ppm)}{at.weight(g/mol)}$ **(Eq. 1. 3)**

and $D = \frac{Na + K + Li + 2Ca}{Al} * \frac{1}{(Al + Si)}$ **(Eq. 1. 4)**

Na, K, Li, Ca, Al, Si are in atomic wt%; H_2O is in wt%; and T in Kelvin. The REE is considered only for LREE from La to Gd, except Eu.

This equation was based on the assumption that the three parameters: T, H_2O and melt composition independently affect the monazite solubility. There are two justifications to support this assumption: (1) Temperature strongly affects on the solubility of monazite, but not the slope of the correlation between melt composition and REE content of the melt. (2) Reducing the water content of the melt simply shifts the Arrhenius type relationship between the solubility and T towards lower intercepts, with only a very small effect on the slope.

This equation (Eq.1.2) fits quite well the data of Montel (1987; 1986; 1993), but disagrees with the result of Rapp et al. (1986; 1987). This was explained by the author that, the composition used by Rapp et al. (1986; 1987) are rich in Ca, Fe and Mg, which can significantly change the solubility of monazite. With the addition of those elements, the melt composition will shift to more metaluminous composition, which then affects the solubility of monazite in the melt. Also, the appearance of Ca in melt will produce allanite at the expense of monazite (Cuney and Friedrich, 1987; Lee and Bastron, 1967).

The proposed equation was extrapolated by using data on the solubility of monazite with different rare earth elements (Ce, Sm) and did not consider the effect of many elements like Fe, Mg, P, F or Cl, etc. In addition, Montel (1993) did not quote the data from Rapp et al. (1986) individually, but sum up as total REE solubility in the melt. This equation may therefore be applicable to only Ca, Fe and Mg poor compositions, with a molar ratio of REE/P equal to 1 and to peralkaline rocks.

Moreover, there are several additional problems with this equation: (1) It does not discriminate between different REE elements, (2) the effect of phosphorus on the solubility product of REE phosphates is not considered at all, (3) the equation would predict a continuous change of solubility with ASI both in the peralkaline and the peraluminous field, while experimental data show no variation in the peraluminous field at all.

1.8. Lanthanide tetrad effect

A “lanthanide tetrad effect” was first discovered by Peppard et al. (1969) during a study of REE distribution between organic liquids and an aqueous phase. Peppard et al. (1969) showed that the partitioning behavior of the lanthanides was not a smooth function of atomic number, but rather showed a periodicity corresponding to quarter, halve and three quarter filled f-orbital levels. Accordingly, this effect is probably related to some interactions between the f-orbitals and the surrounding ligands, similar to the crystal field effects seen in transition metal ions. The lanthanide tetrad effect has since then drawn the attention of geochemists and petrologists. Literature on lanthanide tetrad effects in natural geological materials and experimental products has recently increased with a lot of significant achievements from many authors (Akagi et al., 1993; Bau, 1996; Coppin et al., 2002; Irber et al., 1997; Irber, 1999; Kawabe, 1995; Liu and Zhang, 2005; Masau et al., 2000; Masuda and Akagi, 1989; Monecke et al., 2002; Pan and Bau, 1997; Takahashi et al., 2002; Takahashi et al., 2003; Wu et al., 2004; Zhao et al., 1992). Several authors (Byrne and Li, 1995; McLennan, 1994) have, however, questioned its existence in natural geological samples and often ascribed it to analytical problems or to artifacts of the normalization procedure. However, this problem has been overcome by the advent of new analytical methods such as ICP-MS analyses, which produce a complete REE spectrum with high enough precision (Monecke et al., 2002).

The lanthanide tetrad effect can be observed as a split of rare earth element abundance or distribution patterns into four rounded segments: (1). La–Nd, (2). Pm–Gd, (3). Gd–Ho, and (4). Er–Lu, and each tetrad forms a smooth convex or concave pattern, which is further termed the M-type or W-type tetrad effect (Figure 1.11) (Masuda et al., 1987; Takahashi et al., 2002). The W-type was found commonly in inorganic chemistry (Fidelis and Siekierski, 1971; Siekierski, 1971), aqueous system and near-surface geochemical systems (Kawabe et al., 1991; Masuda et al., 1987; Masuda and Akagi, 1989; Masuda and Ikeuchi, 1979), whereas, the M-type pattern has been reported in many granites or pegmatites, which have undergone a high degree of fractional crystallization, hydrothermal alteration and which are associated with economically important mineralizations (Irber, 1999; Jahn et al., 2001; Seung-Gu et al., 1994; Zhao et al., 1999; Zhao et al., 1993). In these rocks, it therefore appears that the enrichment of rare earth elements is not related to ionic radius, but is somehow controlled by the electronic configuration of the respective rare earth ion.

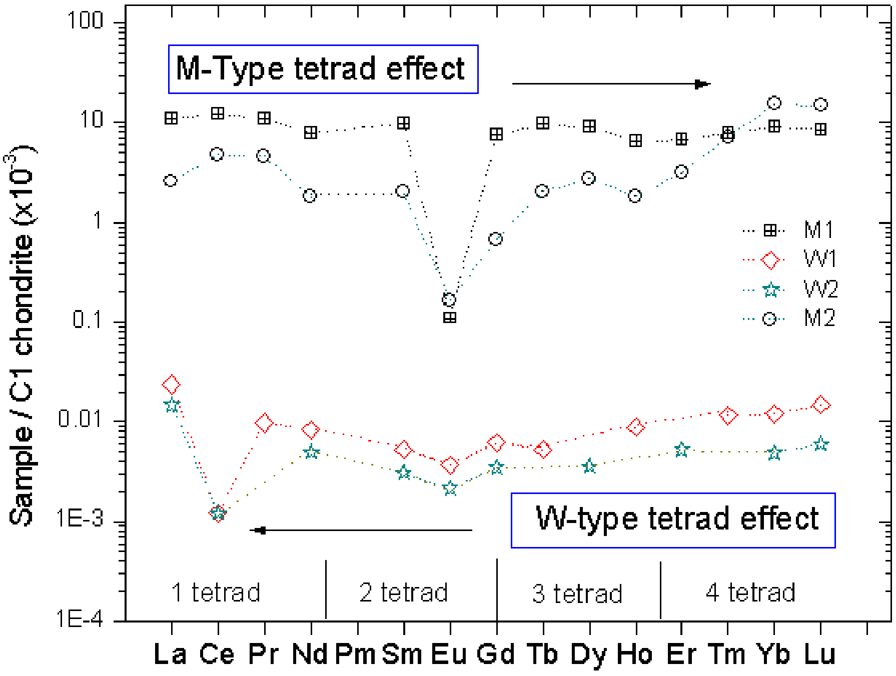

Figure 1.11. Typical examples of M- and W-type tetrad effect observed in REE patterns of granites and seawaters. M1- (Irber, 1999) and M2 patterns (Bau, 1996) are though to be formed by the chemical complexation in an aqueous-like fluid system during the final stage of granite crystallization. W1 (De Baar et al., 1985) and W2 (Piepgras and Jacobsen, 1992) showing a well-defined lanthanide tetrad effect with four concave segments in seawater.

It has been suggested that tetrad effects may be a characteristic indication for the fractional crystallization of REE-rich accessory minerals, such as monazite (Pan and Breaks, 1997; Yurimoto et al., 1990; Zhao and Cooper, 1992), apatite (Jolliff et al., 1989; McLennan, 1994), garnet (Zhao and Cooper, 1992) and xenotime (Foerster, 1998), which largely control the solubility of rare earth elements in granitic melts. These interpretations, however, are not confirmed by experimental work. This is because all experimental studies so far (Montel, 1986; Rapp and Watson, 1986; Rapp and Watson, 1985) only measured the bulk solubility of natural monazite and xenotime crystals in the granitic melt, while no attempt was made to study the partitioning of the individual rare earth elements between these minerals and the granitic melt. Moreover, the existence of the tetrad effect both in minerals and their host rocks is difficult to explain by the fractional crystallization of such accessory minerals. This led to the suggestion that the tetrad effect of highly evolved peraluminous magmas and granite-related rare metal deposits may result from melt/fluid interaction (Bau, 1997; Irber, 1999; Liu and Zhang, 2005) or the transitional nature of volatile rich evolved magmatic liquids (Bau, 1996).

The distribution of rare earth elements (REE) in hydrothermal system has been studied in black smoker vent fluids (Klinkhammer et al., 1994), in dispersed flows at the ocean floor (Michard et al., 1993), in fumaroles and thermal spring waters (Moeller, 2000). The REE abundance in fluids is supposed to be mainly controlled by accessory minerals, REE exchange with rock-forming minerals and their amorphous surface coatings, and coprecipitation of REE with alteration minerals (Moeller et al., 2004). However, a tetrad effect was not observed in the REE patterns in many hydrothermal systems, especially of related vein fluorite samples. The tetrad effect is observed only at the related granite and it is thought to be due to extensive magmatic differentiation, during which there are was intense interaction between the residual melts and aqueous hydrothermal fluid, probably rich in F and Cl (Jahn et al., 2001). Therefore, it is unlikely that the convex tetrad effect in the samples from the magmatic environment can be explained by removal of a respective complementary REE pattern by a coexisting hydrothermal fluid. It is suggested that the tetrad effect formed within the magma-fluid system before phase separation caused a split of this system into fluid and magma subsystems. Alternatively, the tetrad effect may also be inherited from an external fluid influencing the system during or after the emplacement of the magma (Monecke et al., 2002).

In conclusion, the tetrad effect is very common in highly fractionated granites with strong hydrothermal interaction or deuteric alteration. However, the causes of the tetrad effect in natural granites are not yet fully understood.

2. Experimental procedures and methods

2.1. Starting materials and preparation of sample capsules

2.1.1. Synthesis of glasses

Three series of experiments were carried out in this study. The first one was designed to investigate the effect of phosphorus on the solubility of monazite and xenotime in granitic melts. The second one studied the relationship between REE solubility and aluminium-saturated index (ASI), and the last one examined the effect of fluoride on monazite and xenotime solubility in the melt. In addition, a series of reverse experiments was also done to test for equilibrium in the experiments. Table 2.1 lists the chemicals, their purity and manufacturer used to produce the glasses, which served as starting materials in this study. The theoretical composition of the mixtures for glass synthesis is shown in Table 2.2.

Table 2.1. Chemicals used for the synthesis of glasses

Chemical	Purity grade	Manufacturer	Chemical	Purity grade	Manufacturer
$Na_4P_2O_7.10H_2O$	99	Merck	REE_2O_3*	99.9	Chempur
Na_2CO_3	99.9	Merck	CeO_2	99.9	Chempur
K_2CO_3	99	Merck	Tb_4O_7	99.9	Chempur
$Al(OH)_3$	99.9	Merck	AlF3	99.9	Aldrich
SiO_2	99.99	Chempur	KF	99	Merck
H_3PO_4		Merck	NaF	99	Merck

** REE abbreviated for all rare earth elements except Ce and Tb*

Six different glasses (H1-H6) containing 0,1% of P_2O_5 were used as solid starting material for ASI variation series experiments (Table 2.2). Two glasses doped with F (F2 and F4) were prepared by adding NaF, KF and AlF_3 to glass H4 (ASI = 1) so as to obtain the F-content of 2 and 4 wt%. In these glasses, F was introduced so that F replaced a stoichiometrically equivalent amount of O (2F =O) while the molar Al/(Na+K) ratio was kept constant. Two sets of different glasses doped with P_2O_5 content ranging from 0.25 to 1.5 wt% were prepared (Table 2.2). The first one (H82-H86) was based on the peralkaline composition (ASI = 0.8) and the second one (H102-H106) was based on the metaluminous composition (ASI =1). The metaluminous composition of the glasses was 40% of $NaAlSi_3O_8$, 25% of SiO_2 and 25% $KAlSi_3O_8$ corresponding to the 2 kbar water-saturated haplogranite minimum (Tuttle and Bowen, 1958). The theoretical ASI of the glasses was varied from peralkaline (ASI = 0.7) to peralumiunous (ASI = 1.2) by changing the Na, K and Al content, but in all cases the ratio of Na/K = 1 and the silica content were constant. The glasses were prepared by melting mixtures of high purity chemicals supplied by Chempur, Merck and Aldrich companies. Before preparing the sample, all equipment was cleaned well by rinsing in distilled water and dried in the oven up to 150°C in 2-3 hours. The chemicals of K_2CO_3, Na_2CO_3, NaF, KF, AlF_3 and SiO_2 were kept in the oven at 110°C for about 5 hours for drying, then they were cooled down to room temperature in a desiccator for about 2 hours; the water-bearing chemicals such as $Na_4P_2O_7.10H_2O$ and $Al(OH)_3$ were used directly. Chemicals were weighed using an electric SATORIUS – BP 211D microbalance with an accuracy of 0,01mg. Ethanol was used to wash all the chemicals from the weighing paper into the sample jar. The samples were then dried for 5 to 7 days at room temperature in a fume hood. The samples were subsequently homogenized by grinding in ball-grinder under ethanol for 30 minutes. After grinding, the samples were allowed to dry in a fume hood for 2-3 days.

Table 2.2. Theoretical compositions of mixtures for glass synthesis (in weight percent)

	Chemical (g)					Calculated	
Samples	$Na_4P_2O_7.10H_2O$	Na_2CO_3	K_2CO_3	$Al(OH)_3$	SiO_2	ASI	P_2O_5
H1	0.03142	0.98349	0.75895	1.60196	7.86866	0.7	0.10
H2	0.03142	0.91900	0.70918	1.71076	7.86866	0.8	0.10
H3	0.03142	0.86244	0.66554	1.80616	7.86866	0.9	0.10
H4	0.03142	0.81245	0.62695	1.89050	7.86866	1.0	0.10
H5	0.03142	0.76793	0.59260	1.96560	7.86866	1.1	0.10
H6	0.03142	0.72803	0.56181	2.03290	7.86866	1.2	0.10
H82	0.07856	0.88185	0.69385	1.69069	7.86866	0.8	0.25
H83	0.15712	0.84929	0.68562	1.67062	7.86866	0.8	0.50
H84	0.23568	0.81673	0.67738	1.65056	7.86866	0.8	0.75
H85	0.31425	0.78417	0.66915	1.63049	7.86866	0.8	1.00
H86	0.47137	0.71906	0.65268	1.59036	7.86866	0.8	1.50
H102	0.07856	0.77707	0.61340	1.86833	7.86866	1.0	0.25
H103	0.15712	0.74576	0.60612	1.84615	7.86866	1.0	0.50
H104	0.23568	0.71444	0.59884	1.82398	7.86866	1.0	0.75
H105	0.31425	0.68313	0.59156	1.80180	7.86866	1.0	1.00
H106	0.47137	0.62050	0.57700	1.75745	7.86866	1.0	1.50

Then the samples were mixed and ground by hand once again in an agate mortar. The powder was then slowly heated in a platinum crucible to 1000 – 1200 °C and kept there for 10 - 14 hours in order to release all water and carbon dioxide (Table 2.3). The slow heating is necessary in order to avoid an explosive release of volatiles. After decarbonisation, the melted samples were immediately quenched by dipping into distilled water in 30 seconds. After that the samples were dried in oven at 150°C for 5 hours. Those glasses were ground up and melted again at 1600°C in 3.5-6 hours as illustrated in Figure 2.1.

Table 2.3. Melting procedure of the dry glasses used as starting material

Samples	Decarbonatisation				Melting			
	Heating		Annealing		Heating		Annealing	
	(hrs)	(°C)	(hrs)	(°C)	(hrs)	(°C)	(hrs)	(°C)
H1	12	1100	2	1100	2.5	1600	1	1600
H2	9	1200	1	1200	2.5	1600	1.5	1600
H3	10	1000	7	1000	2.5	1600	1.5	1600
H4	12	1100	2	1000	3	1600	0.5	1600
H5	12	1000	2	1000	3	1600	2	1600
H6	12	1000	2	1000	3	1600	3	1600
H82	12	1100	1	1100	2.5	1600	1	1600
H83	12	1100	1	1100	2.5	1600	1	1600
H84	12	1100	1	1100	2.5	1600	1	1600
H85	12	1100	1	1100	2.5	1600	1	1600
H86	12	1100	1	1100	2.5	1600	1	1600
H102	12	1100	1	1100	2.5	1600	1	1600
H103	12	1100	1	1100	2.5	1600	1	1600
H104	12	1100	1	1100	2.5	1600	1	1600
H105	12	1100	1	1100	2.5	1600	1	1600
H106	12	1100	1	1100	2.5	1600	1	1600

The samples obtained after decarbonatisation were not hundred percent glassy. They contained a lot of tiny crystals. The number of the crystals increased with increasing aluminium. However, after melting at 1600 °C, the samples were hundred percent glassy. About 470 mg of these crystal-free glasses and 30 mg H_2O were welded into gold capsule (35 x 5 x 0.25 mm) to produce water-saturated starting haplogranite glasses containing about 6 wt% H_2O. These syntheses were carried out at 2kbar and 800°C in cold-seal vessels with a run duration of 10-12 days. The glass composition and water content were checked by electron microprobe (EMPA), X-ray powder diffractometry (XRD) and near infrared spectrometry (FTIR) (see detail below). The compositions of hydrous glasses are listed in Table 2.4.

Table 2.4. Average electron microprobe analyses of water saturated starting materials at $800^{o}C$/ 2 kbar in cold seal system. Run duration is 10-12 days. Values given in weight % and relative error limits were estimated from the standard deviation (1δ) based on replicate analyses (N). Water content was measured by FTIR.

Sample	Na_2O	K_2O	Al_2O_3	SiO_2	P_2O_5	F	Total	H_2O	N	ASI*
	%	%	%	%	%	%	%	%		
G1	5.22±0.13	5.35±0.20	10.38±0.04	72.23±0.27	0.13±0.02	-	93.37±0.26	5.86	5	0.73±0.02
G2	5.58±0.20	4.20±0.02	10.75±0.08	74.00±0.91	0.12±0.04	-	94.64±0.91	5.66	5	0.79±0.02
G3	4.99±0.15	4.19±0.18	11.56±0.05	73.50±0.49	0.13±0.04	-	94.39±0.61	5.96	6	0.91±0.03
G4	4.65±0.08	3.87±0.11	12.13±0.06	74.11±0.42	0.10±0.01	-	94.96±0.22	5.31	6	1.03±0.02
G5	4.54±0.17	4.11±0.11	13.04±0.16	74.39±0.18	0.12±0.01	-	96.24±0.35	6.25	6	1.10±0.02
G6	3.90±0.14	3.81±0.14	12.74±0.16	74.24±0.13	0.11±0.01	-	94.47±0.34	5.42	7	1.22±0.02
G11	5.38±0.04	4.91±0.01	10.36±0.13	73.11±0.93	0.11±0.03	-	93.88±0.99	5.56	6	0.74±0.01
G12	5.17±0.04	4.49±0.03	10.78±0.19	74.56±0.93	0.10±0.01	-	95.10±0.86	5.81	6	0.81±0.01
G13	4.58±0.08	4.48±0.03	11.44±0.15	72.26±0.91	0.11±0.02	-	92.88±1.04	5.74	7	0.93±0.01
G14	4.22±0.09	4.47±0.02	11.91±0.11	75.13±0.33	0.10±0.02	-	95.85±0.35	5.75	7	1.02±0.02
G15	3.84±0.12	3.99±0.03	11.93±0.07	74.14±0.46	0.12±0.03	-	94.03±0.43	5.96	6	1.13±0.02
G16	3.72±0.21	3.70±0.09	12.53±0.20	75.33±0.57	0.09±0.01	-	95.39±0.73	5.58	7	1.25±0.05
AF2	4.19±0.14	4.09±0.08	12.18±0.30	70.68±0.36	0.10±0.02	1.79±0.28	93.04±0.37	5.72	20	1.08±0.04
AF4	4.25±0.14	4.23±0.05	12.16±0.30	68.59±0.40	0.10±0.02	3.88±0.12	93.23±0.91	5.64	11	1.06±0.02
G81	5.09± 0.10	4.22± 0.12	11.00± 0.13	73.39± 0.14	0.12± 0.02	-	93.83± 0.24	5.92	5	0.86± 0.02
G82	5.27± 0.44	4.58± 0.12	10.88± 0.10	73.30± 0.81	0.31± 0.02	-	94.33± 0.43	5.76	13	0.80± 0.03
G83	5.14± 0.39	4.34± 0.12	10.58± 0.15	73.69± 0.59	0.49± 0.04	-	94.24± 0.89	5.81	13	0.81± 0.02
G84	5.13± 0.40	4.44± 0.04	10.54± 0.08	73.63± 0.42	0.73± 0.03	-	94.47± 0.64	6.15	23	0.80± 0.03
G85	5.12± 0.57	4.25± 0.17	10.42± 0.15	73.92± 0.16	0.97± 0.04	-	94.68± 0.47	5.73	12	0.81± 0.04
G86	5.24± 0.48	4.11± 0.18	10.13± 0.07	73.58± 0.23	1.45± 0.05	-	94.54± 0.50	5.98	12	0.78± 0.04
G101	4.14± 0.05	3.52± 0.05	11.12± 0.08	74.32± 0.68	0.11± 0.01	-	94.49± 0.84	5.87	6	1.05± 0.04
G102	4.47± 0.39	4.03± 0.07	12.09± 0.14	74.35± 0.67	0.25± 0.02	-	95.21± 0.50	6.29	13	1.04± 0.03
G103	4.47± 0.53	3.96± 0.04	11.80± 0.09	72.66± 0.38	0.49± 0.03	-	93.39± 0.89	5.77	13	1.02± 0.02
G104	4.80± 0.08	4.13± 0.03	12.07± 0.15	73.51± 0.58	0.70± 0.02	-	95.21± 0.51	5.64	5	0.98± 0.03
G105	4.55± 0.37	3.87± 0.05	11.76± 0.21	73.40± 0.54	0.97± 0.03	-	94.55± 0.62	6.08	13	1.01± 0.04
G106	4.43± 0.26	3.82± 0.18	11.20± 0.19	73.54± 0.54	1.47± 0.09	-	94.40± 0.51	5.83	13	0.99± 0.04

**ASI = Al/(Na+K) in mol*

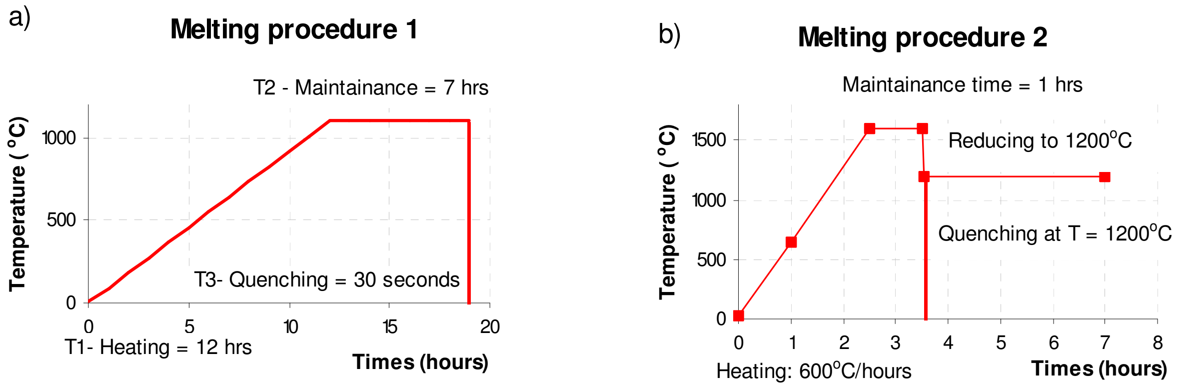

Figure 2.1. Temperature profile for glass synthesis. (a) Decarbonisation and (b) melting

2.1.2. Hydrothermal growth of monazite and xenotime

The respective oxide of REE (99.9% purity, Chempur chemicals) was mixed with an excess of H_3PO_4 to synthesis monazite and xenotime hydrothermally following the reactions:

$$REE_2O_3 + 2\ H_3PO_4 = 2\ REE\ PO_4 + 3\ H_2O \qquad \text{(Eq. 2.1)}$$

where REE stands for all rare earth elements, except Ce and Tb where oxides of different stoichiometry were used:

$$2\ CeO_2 + 2\ H_3PO_4 = 2\ CePO_4 + 3\ H_2O + ½\ O_2 \qquad \text{(Eq. 2.2)}$$

$$Tb_4O_7 + 4\ H_3PO_4 = 4\ TbPO_4 + 6\ H_2O + 1/2O_2 \qquad \text{(Eq. 2.3)}$$

In this study, all syntheses were carried out at 800 °C and 2 kbar in 18- 30 days. The experimental batches were prepared such that a 20 % excess of H_3PO_4 (55-75 %) was injected into the bottom of a gold capsule, and 20 – 50 mg of pure REE oxide was placed on the top. Either small gold capsules (25 mm long x 6 outer diameter x 0,1 mm wall thick) or big capsules (35 x 5 x 0,25 mm) were used. The capsules were welded shut and placed into oven at 150°C overnight, and re-weighted to check for leaks. The experiments were run in cold seal pressure vessels with the Ni-CrNi thermocouples inside the bombs close to the sample position.

After run, the gold capsules were opened and excess H_3PO_4 was rinsed away by distilled water. The crystals were then analyzed by optical microscopy (LEICA DMRX), scanning electron microscopy (SEM), Raman spectroscopy, electron microprobe (JEOL 8900) and X-ray powder diffractometry (Philips PW 1050/25) (for details, see below).

For EMPA analysis, crystals were embedded in epoxy resin and polished. The crystals were pure REE phosphates with monazite or xenotime structure, no other phases were detected. The colour of monazite changed from sample to sample, depending on its composition. Ce-monazite formed white crystal, La-monazite formed brown ones, Pr-monazite is plate blue, Nd-monazite is violet, Sm-monazite is light yellow, Eu-, Gd-, Tb- and Dy-rare earth phosphate crystals are milky white, and Er-xenotime has pink colour.

Raman spectra showed that the structure of starting material rare earth phosphate was different for the light and heavy REE (Figure 2.2). The X-ray diffraction confirmed that the rare earth phosphate crystals were either pure monazite or xenotime, except for gadolinium phosphate. No other solid phases were present (Figure 2.3) and (Figure 2.4). Since $GdPO_4$ formed both structures, a Rietveld refinement was carried out for sample $GdPO_4$ using TOPAS v.3 software (www.bruker-axs.com). Basic principles about this method can be found in detail somewhere else (Rietveld, 1969).

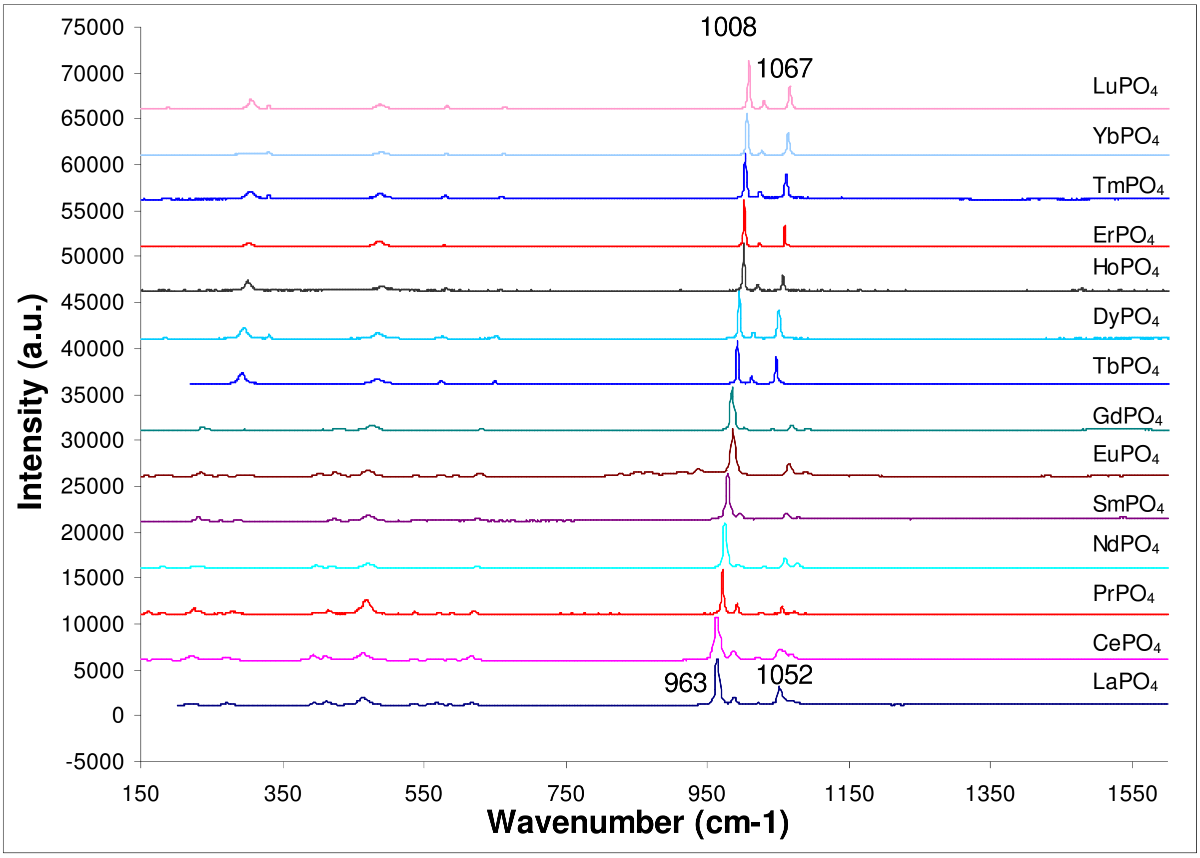

Figure 2.2. *Raman data showing changes in the crystal structure of the synthetic REE phosphates. Spectra were obtained using Labram2 Raman spectrometer equipped with Olympus microscope.*

Structure data of pure single monazite ($GdPO_4$) and of xenotime ($TbPO_4$) (Ni et al., 1995) were used as standard for the refinement. Xenotime ($TbPO_4$) was used instead of xenotime ($GdPO_4$) because there was no available data for pure xenotime ($GdPO_4$) in the literature and because the ion radius of Tb is close to Gd. In addition, the amount of sample is very small, leading to the low quality of the X-ray diffraction data. Thus, the result is only approximately estimated with a very low refinement R_{wp} (sometimes also referred as wR2 = weighted R-value) of less than 0.3, in most of the trial refinement performances. The refinement showed that, the $GdPO_4$ formed a mix of separate crystals with about 80-90 wt% monazite and 10-20 wt% xenotime, respectively (Figure 2.5).

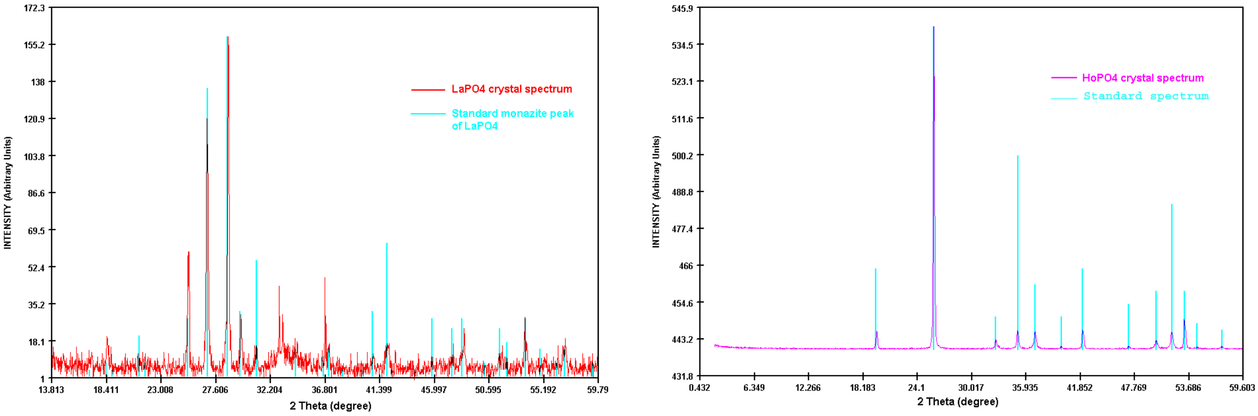

Figure 2.3. Typical samples of monazite ($LaPO_4$) and xenotime ($HoPO_4$) X-ray diffraction patterns

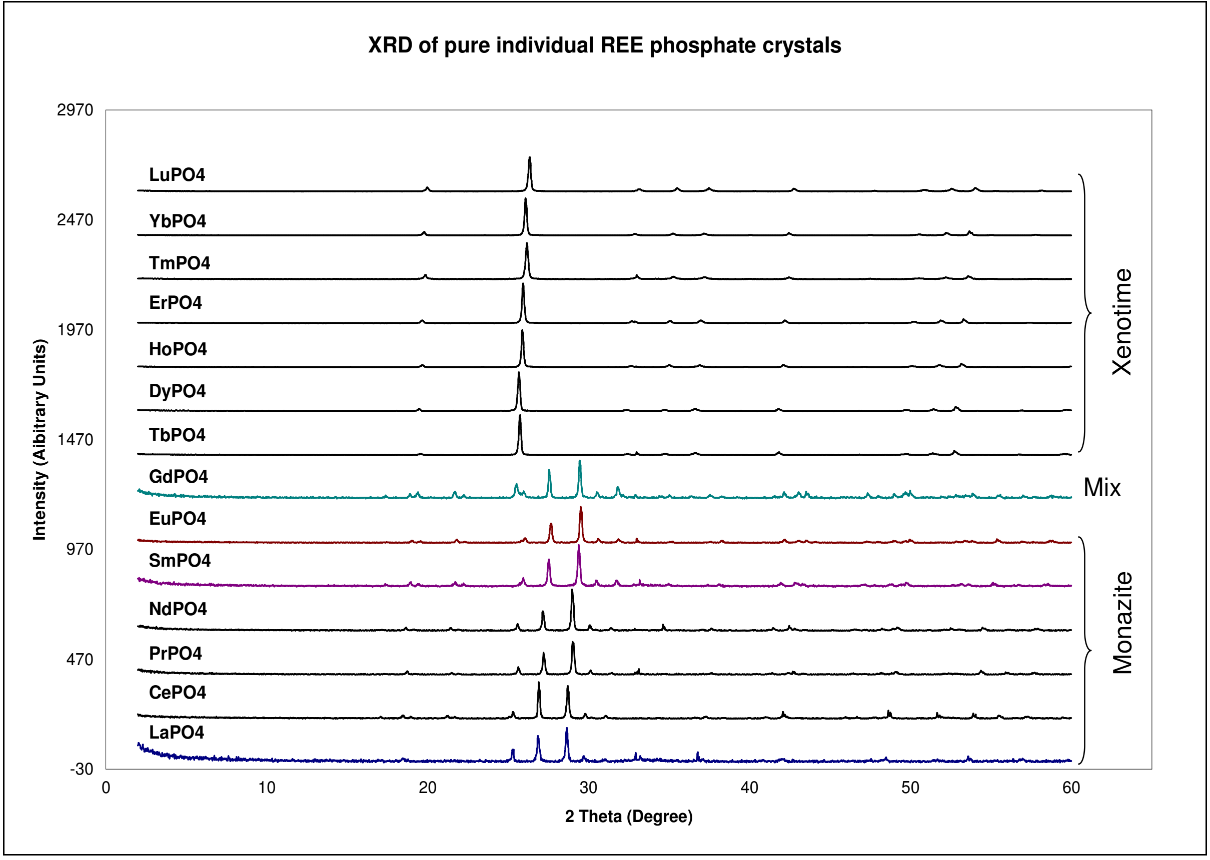

Figure 2.4. XRD data for different crystal structures of the synthetic REE phosphates

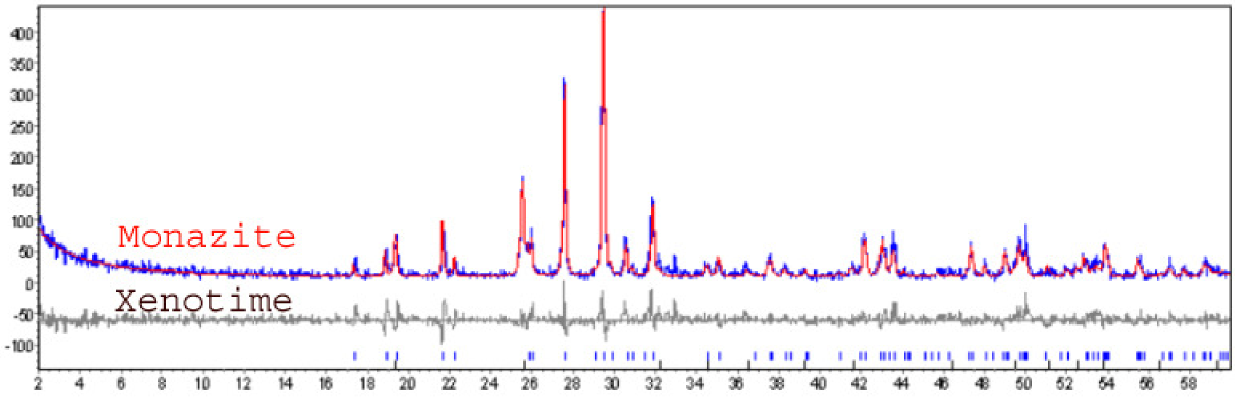

Figure 2.5. Rietveld refinement of the $GdPO_4$ sample using XRD data yielded a mix of separate crystals with 80-90 wt% monazite and 10-20 wt% xenotime, respectively (performed by V. Presser).

The monazite/xenotime crystals produced in this study were generally large (Figure 2.6), the average size was 30-50 µm, the biggest one was up to 120 µm in size, and the smallest one was around 10-20 µm in length for the runs of less than 20 days. In the runs that lasted more than 20 days, some big crystals were formed, with size up to 167 µm in sample M2.

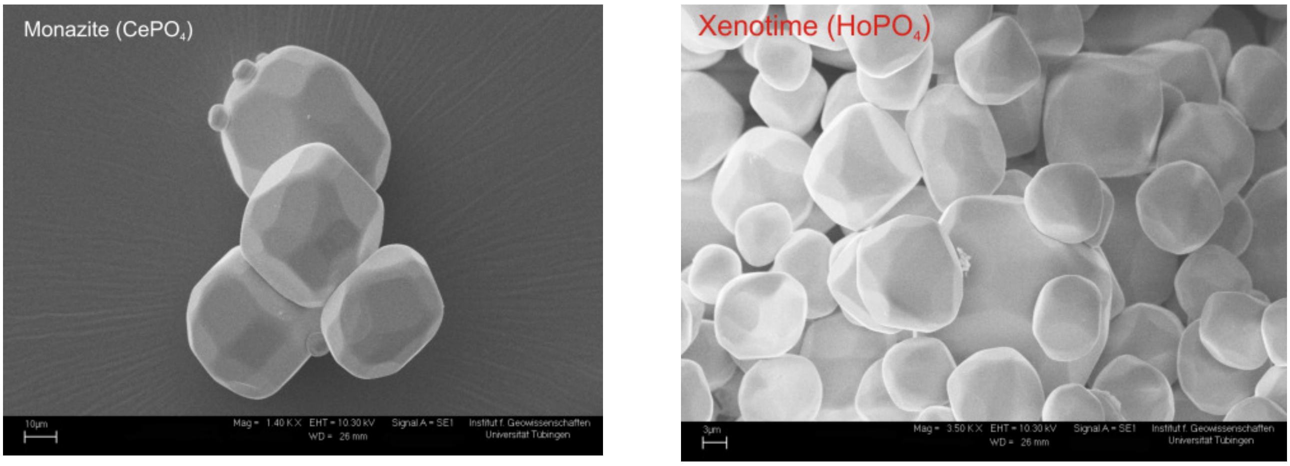

Figure 2.6. Monazite ($CePO_4$) and xenotime ($HoPO_4$) imaged by SEM

The crystals produced in this study were larger than those reported by Montel (1986) and Andrehs and Heinrich (1998) who observed crystal sizes smaller than 1 µm and from 1 to 20 µm, respectively. In some cases the samples in this study contained some very big crystals and the remaining crystals were small, ranging from some µm to 30-40 µm. Samples without big crystals were usually more uniform in grain size (40-50 µm), The larger crystal size obtained in our study may be related to the higher fluid/solid ratio as compared to previous work. Monazite always formed bigger crystal than xenotime at the same growing condition.

2.1.3. Preparation of sample capsules for monazite and xenotime solubility experiments

The solubility experiments were all prepared by carefully mixing 90 wt% of water saturated haplogranite glass powder and 10 wt% of pure single rare earth phosphate crystals. This mixture was then welded shut in small gold capsules of 25 mm length and 2,5 mm diameter with 0,25 mm wall thickness. Most of them were dissolution experiments in a slow-quench cold seal system (CSS) with 1-2 months run duration (see below). One series of dissolution experiments was run at high temperature conditions (1100°C) using platinum (Pt) capsules (15 mm long, 5 mm outer diameter and 0.2 mm wall thickness) in internal heated pressure vessels (IHPV) (see below). The run products of this high temperature dissolution experiment were then used as starting material for reverse runs in cold seal bombs at 800°C and 2 kbar for 2 months. Capsules were checked for leaks before use.

2.2. High pressure apparatus and technique

2.2.1. Cold seal systems (CSS)

Cold seal systems are among of the most popular techniques for high-pressure and temperature experimentation. For details, see Huebner (1971), Edgar (1973), and Kerrick (1987). Cold seal systems in their modern version were first designed by Tuttle (1949). The main component of the cold seal system in Tuebingen is a cylindrical pressure vessels ("bomb") and a closure assembly shown in Figure 2.7. The cold seal pressure vessels of 39 mm outer diameter, 7 mm inner diameter, and 235 mm length are made from "superalloys", which can be exposed at elevated temperatures and pressure because of their ability to retain most of their strength and resistance to oxidation even after long exposure times at high pressure and temperature.

Superalloys are based on Group VIIIB elements and usually consist of various combinations of Fe, Ni, Co, and Cr, as well as lesser amounts of W, Mo, Ta, Nb, Ti, and Al. The three most popular classes of superalloys are nickel-, iron- and cobalt-based alloys (these designation reflect the dominant chemical elements of the alloy), in which nickel-based classes have been used a lot and are particularly well suited for many applications because of their stability and corrosion resistance at the highest temperatures. For cold seal system, a variety of alloys may be used to examine a wide-range of processes at the pressure and temperature of the Earth's crust. Stellite 25, a cobalt-based and Rene 41, a nickel-based alloy are commonly used for cold seal vessels. However, these alloys have showed some limitations when they were used at high pressure and temperature in long runs. According to our experiences, the Rene 41 vessels were expanded about 0.02-0.1 mm after 1-2 months run at 800^{o}C and 2 kbar. Thus we have tried to use new superalloys of NIMONIC 105 and IN 713LC. Those materials showed good stability after long run durations at 800^{o}C and 2 kbar. Compositions of those alloys are given in Table 2.5.

Experiments were started by loading a sealed capsule into the bottom of a cold seal bomb, and pressuring the autoclave with H_2O. The capsule was close to the internal thermocouple. A nickel filler rod was used to reduce thermal gradients (Figure 2.7). Oxygen fugacity of the experiments was not strictly controlled, but it was believed to be close to that of Ni-NiO equilibrium, buffered by the oxidation reaction of the pressure medium (water) with the Ni-rich alloy of the pressure vessels and the nickel filler rod. All experiments were performed at condition of 800^{o}C and 2 kbar. The dissolution experiments lasted 1-2 months and reverse crystallization experiments were performed in 2 months. Pressure inside the vessel was measured with strain-gauges calibrated against a Heise gauge with the accuracy ± 0.03 kbar.

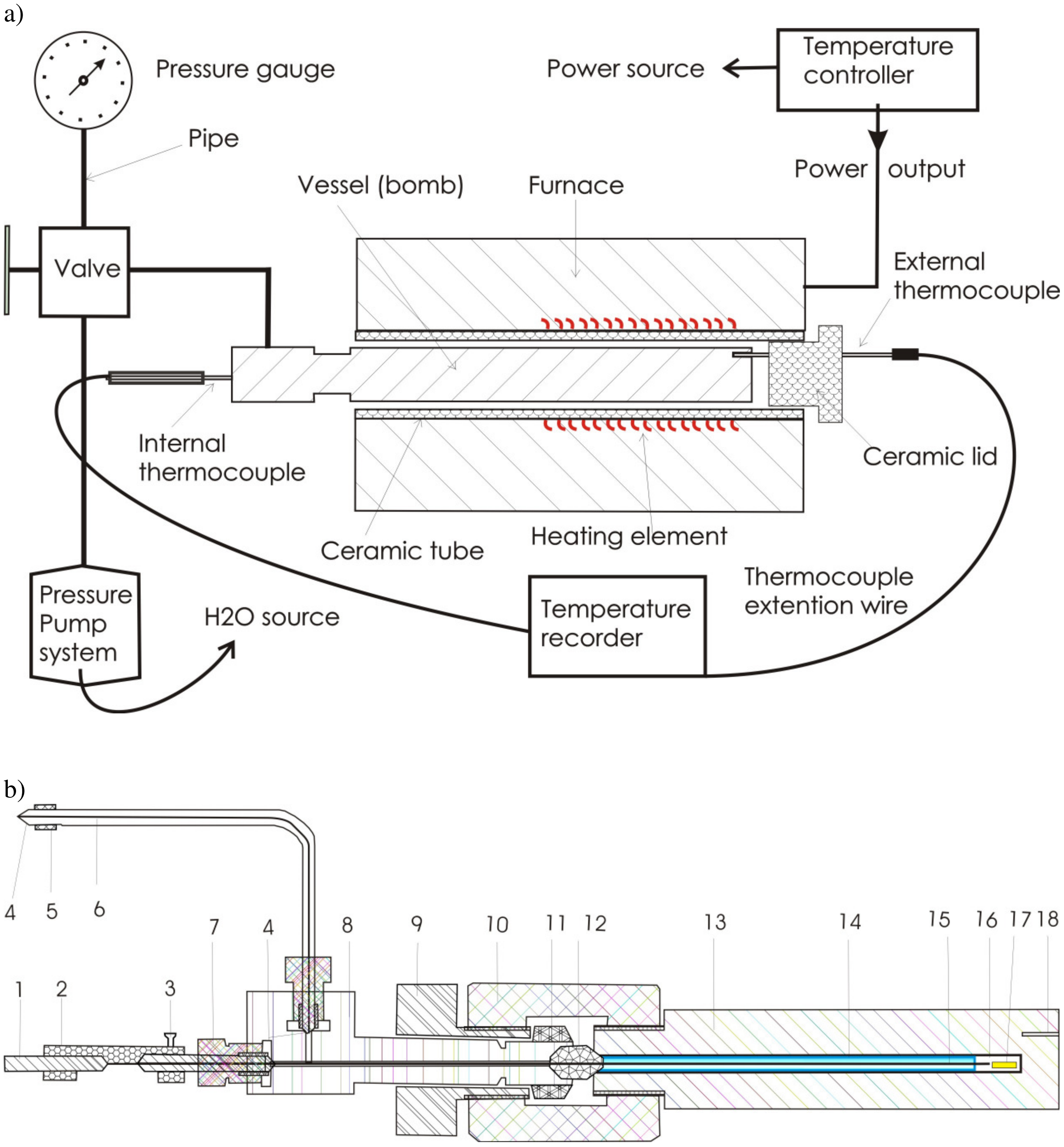

Figure 2.7. (a) Schematic overview of a cold seal system. (b) Cross section of a cold seal vessel (bomb): 1- Socket for internal thermocouple; 2- Thermocouple mount; 3- Screw; 4- Closure cone; 5- small retainer ring; 6- Pressured tubing; 7- Compression seal; 8- Metal adaptor; 9- Closure bolt; 10- Closure nut; 11-Retainer collar; 12-Double sealing cone; 13- Pressure vessel (outer - ∅ 39 mm); 14- Filler rod (nickel); 15- Type-K internal thermocouple; 16- Sample chamber (∅ 7 mm); 17- Capsule; 18 – External thermocouple well.

Table 2.5. Material of the vessels

Elements	NIM 105	IN 713LC	Rene 41
Aluminium	4.5 – 4.9	6,00	1.40-1.80
Boron	0.003 - 0.01	0.007	
Carbon	0.12 max	0,05	
Chromium	14-15.7	12,00	18.00-20.00
Cobalt	18-22		10.00-12.00
Copper	0.2max		
Iron	1 max		5.00 max
Manganese	1max		
Molybdenum	4.5-5.5	4,50	9.00-10.50
Niobium		2,00	
Nickel	Balance	74,75	Remainder
Silicon	1max		
Sulphur	0.01max		
Titanium	0.9-1.5	0,70	3.00-3.30
Zirconium	0.15max		
		Plus other minor impurities	Plus other minor impurities

Pressures were estimated to be accurate to ± 0.1 kbar for all runs. After loading the bomb, the vessel was first charged with H_2O up to the initial pressure of about 1 kbar, then it was isolated from the H_2O reservoir and water pump. The pressure inside the vessel was then increased to the final pressure of 2 kbar by using the pressure intensifier and oil pump. The vessel was then completely isolated from the pressure pumping system. The loaded bombs were left over night at 2 kbar to check for leaks. They were then isobarically heated in 2 hours to reach the final run condition at 800^{o}C. Temperatures were controlled by a K-type NiCr-Ni thermocouple placed either inside close to the capsules or outside of the vessel in an external thermocouple well close to the hot spot zone. The vessels were calibrated periodically and the temperature was known within of ± 15^{o}C.

On completion, the experiments were quenched by removing the vessel from the furnace and blowing compressed air around the vessels. Right after removing the vessel from the furnace, the pressure inside the bomb was first isothermally increased up to 2.5 kbars to avoid bubble nucleation. During the isobaric quenching in air, the temperature inside the vessel dropped to ~ 200^{o}C after 4-5 minutes, then decreased to room condition in 15-20 minutes.

After quenching, the capsules were taken out the vessel, cleaned, dried, weighed and then put into oven at 150^{o}C over night to check for leaks. Most capsules gained a small amount of weight during the run, probably due to alloying of the gold capsule with nickel.

2.2.2. Internally heated pressure vessels (IHPV)

High temperature dissolution experiments were performed at the Institute for Mineralogy, Hannover University, Germany by using an internally-heated pressure vessels. This system is described in detail by Berndt et al (2002). The general features of the technique are also presented somewhere else (Holloway, 1971; Lofgren, 1987). This series of experiments was performed at pressures of 2 kbar and 1100°C in 7 days at quartz-fayalite-magnetite (QFM) buffer conditions controlled by a hydrogen gas buffer (f_{H_2}). The samples were fixed to a Pt-wire and were loaded into the sample chamber in hot spot. After loading the IHPV and flushing with pure hydrogen, the vessel was first charged with hydrogen up to the initial P_{H_2}, and then isolated from the H_2-reservoir. After that the vessel was loaded with Ar up to 1 kbar. The vessel was then completely isolated from the Ar pressure line. The H_2-line was evacuated before raising the temperature to 1100°C. The heating rate was about 30°C/min and controlled by using Eurotherm 906 EPC controller. The insulation of the heater consisted of steel foil, mullite, and quartz wool. The errors of temperature were less than 5°C along the sample capsule; temperature was controlled by five S-type thermocouples. Two of them, connected to the Eurotherm unit, were used to control the power supply of the two furnace windings. Three additional thermocouples were inserted into the ceramic tube surrounding the samples and were positioned about 2 mm from the capsules to determine the exact temperature of the samples hanging inside the ceramic tube.

At the end of the experiment, the quench Pt-wire in the hot spot of the furnace was fused electrically and the samples dropped down to the copper block unit of the cold quench area that was in direct contact to the water cooled vessel body. The temperature of the cold-quench area was 20–25°C continuously measured by a K-type thermocouple placed on the bottom of the copper block unit. The quenching rate was about 150°C/s. Temperature decreased from 1100°C to 500°C within 1 minute and then decreased slowly to room temperature in 15 minutes. All temperatures and pressures of the IHPV were logged automatically by a LabView computer monitoring system, National Instruments, Austin, Texas and showed no oscillations or other transient failures during the run and quenching.

2.3. Investigation of run products

2.3.1. Electron Microprobe Analyses (EMPA)

Quantitative electron microprobe analyses (EMPA) were performed at Tübingen University on a JEOL 8900 equipped with five wavelength dispersive spectrometers. Table 2.6 shows the typical measuring conditions for the run products. Analyses were all performed at 20 kV accelerating voltage and 50 nA beam current with a defocused beam of 20 µm diameter. A large-diameter spot was used to minimize volatilization (especially of Na). Test measurements showed that the Na signal was almost stable within 4 seconds. This result was slightly different from Wolf and London (1995), who suggested that no Na loss occurs only for total analysis times up to 2 seconds. However, the shorter time measurement will produce larger errors, thus, 4 seconds for Na measurement was considered to be a reasonable solution. The following synthetic and natural standards were used for the calibration (Table 2.6): Albite (Na), synthetic blank glass in REE block (Si), sanadine (K), fluorite (F), apatite (P) and individual rare earth synthesis glass (REE and Al). Counting time for Na was set at 4 and 2 seconds for peak and background, respectively. For F, counting time was 60 and 15 seconds for peak and background. For K and P, it was set at 30 seconds for peak and 15 seconds for background. Analytical time for Al and Si were 16 and 8 seconds for peak and background respectively. The REE were analyzed 120 seconds at the peak and 60 seconds for background on each side of the peak. There was a minor overlap of the P peak with some peaks from HREE and of the F peak with some peaks from P, K and/or REE. For these particular cases, a systematic correction for P and F was applied during the calibration. The calibration was tested routinely using synthetic REE bearing glasses prepared by Drake and Weill (1972). We also used our individual pure $REEPO_4$ crystals to test the calibration. About 25 random analyses for each experiment were obtained for calculating the average content of REE in the sample and at least 3 profile sections were analyzed to fit diffusion profiles. The measuring positions were chosen at the center of areas consisting of pure glass (Figure 2.8 – MH302). The profile analyses were performed in the “cleanest” areas, where the concentration of REE was thought to be controlled by the two monazite/xenotime crystals at both ends of the profile. During measurement, however, the profiles were always slightly shifted away from the desired line (Figure 2.8 – MH412). Analyses were obtained up to a distance of > 10 µm from monazite/xenotime crystals. Fluorescence by the monazite/xenotime crystals will be a problem if the analytical point was < 10 µm from the monazite/xenotime crystals.

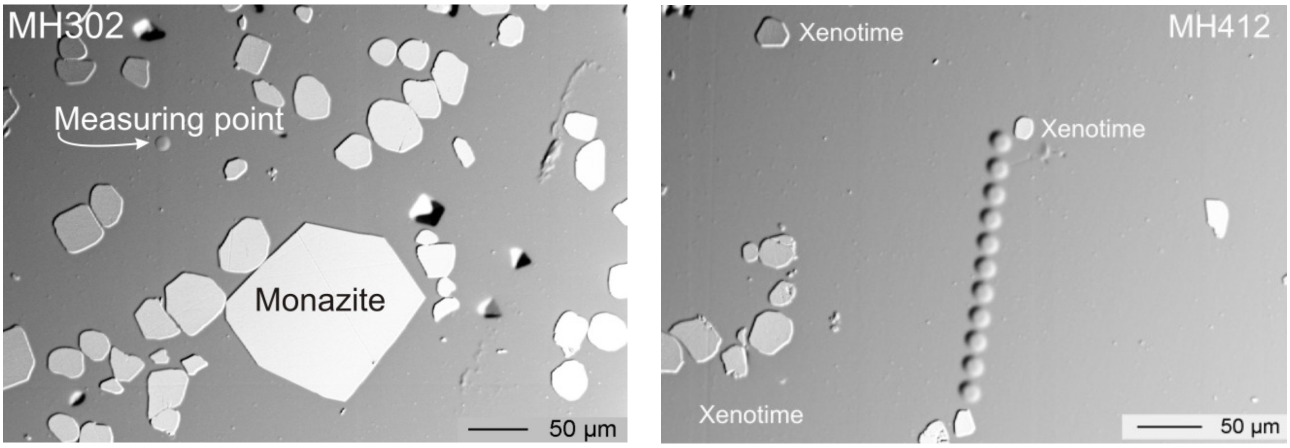

Figure 2.8. Measuring point (MH302) and measuring profile (MH412) of run product at 800°C and 2 kbar. Step interval away from the crystal glass interface is 20.05 µm

Table 2.6. Typical EMPA measurement conditions at 20 kV accelerating voltage and 50 nA beam current with a defocused beam of 20 μm diameter

Elements	X-ray line	Channel	Crystal	Standard	Spectrum position	Measured time (s)		Detection limits
					(mm)	Peak	Background	(ppm)
Na	Kα	2	TAP	Albite	129.714	4	2	102
K	Kα	3	PETJ	Sanidine	119.731	30	15	46
Al	Kα	2	TAP	REE_glass	90.889	16	8	71
Si	Kα	2	TAP	Blank_glass	77.664	16	8	103
F	Kα	1	LDE1	Fluorite	86.222	60	15	89
P	Kα	3	PETJ	Apatite	197.229	30	15	72
La	Lα	4	LIFH	La glass	185.326	120	60	79
Ce	Lα	4	LIFH	Ce glass	178.098	120	60	74
Pr	Lα	4	LIFH	Pr glass	171.267	120	60	62
Nd	Lα	4	LIFH	Nd glass	164.961	120	60	57
Sm	Lα	4	LIFH	Sm glass	153.132	120	60	72
Eu	Lα	4	LIFH	Eu glass	147.546	120	60	68
Gd	Lα	4	LIFH	Gd glass	142.391	120	60	77
Tb	Lα	4	LIFH	Tb glass	137.647	120	60	71
Dy	Lα	4	LIFH	Dy glass	132.815	120	60	82
Ho	Lα	4	LIFH	Ho glass	128.394	120	60	65
Er	Lα	4	LIFH	Er glass	124.368	120	60	73
Tm	Lα	4	LIFH	Tm glass	120.368	120	60	76
Yb	Lα	4	LIFH	Yb glass	116.559	120	60	88
Lu	Lα	4	LIFH	Lu glass	112.801	120	60	69

2.3.2. Powder X-ray diffraction (XRD)

In order to confirm the phases present in the samples, representative samples were analyzed by X-ray diffraction. The X-ray investigation of the powder samples was performed on a Philips PW 1050/25 diffractometer at Tuebingen University at room temperature using a curved germanium monochromator in Debye-Scherrer geometry. The samples were first crushed to 1-30 μm particle size in mortar/pestle, and then pressed on a silicon sample holder. Measurement was set up at condition of 40kV / 20mA, Cu Kα, 0,05° 2θ-scan with step size 0.05° and scan rate 0.05°/4 sec.

2.3.3. Near Infrared (FTIR) measurement of hydrous glasses

Water contents of the starting water-saturated haplogranite glasses were measured in Tübingen by a Bruker IFS 125 HR Fourier transform infrared spectrometer (FTIR), using a tungsten light source (W lamp), Si-coated CaF_2 beam splitter and a high-sensitivity, narrow-band mercury cadmium tellurium (MCT) detector. The spectrometer is coupled with a Bruker IR microscope containing an all-reflecting Cassegranian optics that allows measurements of small areas with apertures down to 10 µm. Each spectrum with a resolution 4 cm^{-1} was accumulated from hundreds of scans and was obtained in the wavenumber range from 1000 to 10000 cm^{-1} (Figure 2.9). During the measurement, the optics of the spectrometer was evacuated and the microscope was purged with a stream of H_2O and CO_2-free purified air.

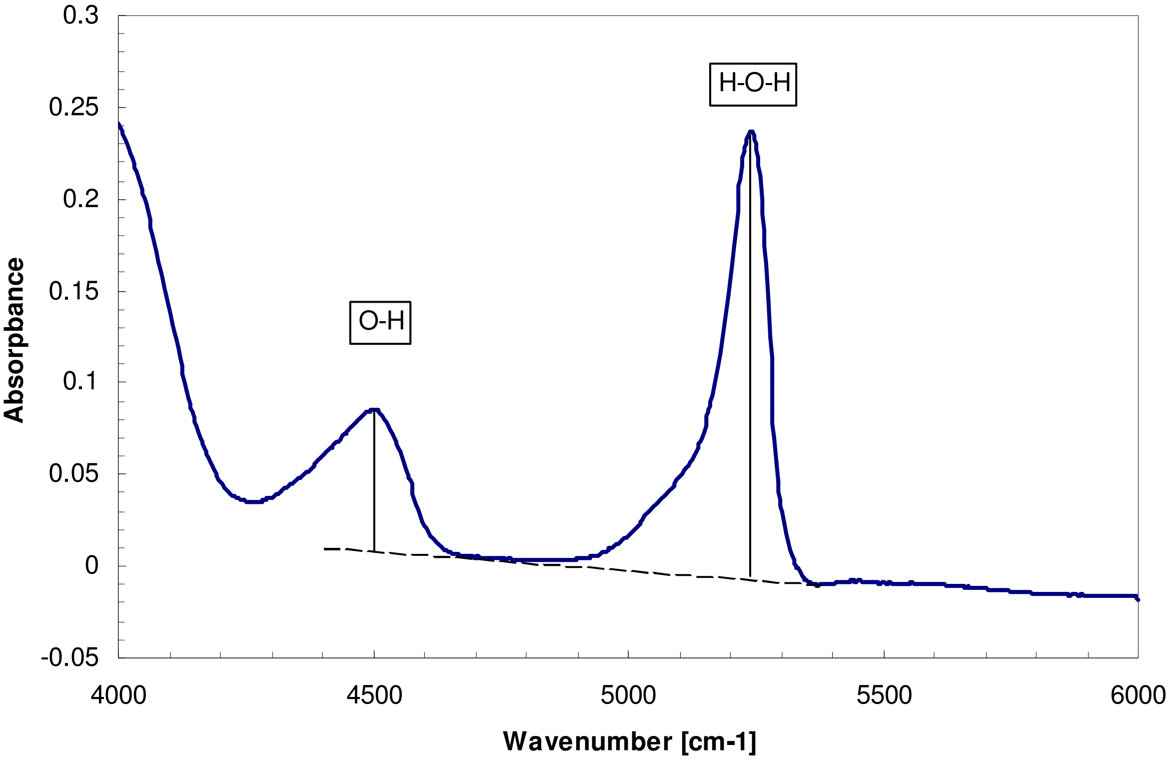

Figure 2.9. Near-infrared absorption spectra obtained from a haplogranitic glass containing 6 wt% water. Sample thickness: 224 µm. Dashed line is linear baseline

The background correction of absorbance spectra was carried out using a spline fit of the baseline defined by points outside the OH stretching region. For quantitative infrared absorbance measurements, a flat (planar on a micron scale) doubly polished sections of the volatile-containing glass was prepared ranging in thickness from several tens to several thousands µm.

Sample chips were mounted in “crystal-bond”, and glued to microscope slides, then they were ground and polished with alumina and diamond paste or diamond-impregnated paper (water and cutting oil were used as lubricants). The last polish was applied with 1 µm diamond paste. After polishing, samples were removed from the microscope slides and cleaned by acetone. Because the volatile content was measured in the bulk sample, traces of adsorbed atmospheric water or CO_2 did not affect the results. However, special care had to be used for samples with high alkali content, which react substantially with atmospheric water and CO_2.

After polishing, the sample thickness was carefully measured with a micrometer, or by visual determination under a calibrated microscope. The error of the micrometer measurements was about 2-3 µm. For some samples, the thickness was determined by focusing with a microscope on the upper and lower surface of the doubly-polished slab. The thickness was then calculated from the scale of the vertical fine-adjustment of the microscope, with an uncertainty of 3 – 6 µm.

To avoid the high error of the microscopic technique and the substantial error for the thinnest samples when using the micrometer, both methods were combined. Firstly, the maximum thickness of the sample was measured by micrometer and secondly, at each spot used for infrared measurements, the thickness of the sample was measured with the microscope, and then calibrated against the maximum thickness of the sample.

The density of the hydrous glasses was calculated using equation (Eq.2.4) given by Sowerby and Keppler (1999) for haplogranite $Qz_{28}Ab_{34}Or_{38}$ glasses which refers to a composition similar to those relevant for this study .

$$\rho_{g/l} = 2347 - 12.6\ (C_{H2O}) \qquad \text{(Eq. 2.4)}$$

Where: $\rho_{g/l}$ is the density of the sample and C_{H_2O} is the water content of the starting material (in weight %).

The total water concentrations, as well as the concentrations of hydroxyl groups and molecular water in glass were calculated from the heights of the absorbance bands by the Beer-Lambert law (Stolper, 1982):

$$A = \varepsilon \, . \, C \, . \, d \qquad \text{(Eq. 2.5)}$$

$$C = \frac{A}{d\varepsilon} \qquad \text{(Eq. 2.6)}$$

$$\Rightarrow C = \frac{18.015 * A}{d\rho\varepsilon} \qquad \text{(Eq. 2.7)}$$

Where: 18.015 is the molecular weight of H_2O
C: Water content (g/kg)
A: absorbance (unitless)
d: Sample thickness (cm)
ρ: Sample density (g/L)
ε: Molar absorbability (L/mol.cm)

For the total water content, the formula can be rewritten as:

$$C_{Total} = \frac{1}{\in^{*}_{OH}} \frac{18{,}015 A_{OH}}{\rho d} + \frac{1}{\in^{*}_{H_2O}} \frac{18{,}015 A_{H_2O}}{\rho d} \qquad \text{(Eq. 2.8)}$$

Where: C_{Total} is the total water concentration in the sample (g/kg)
A_{HO}, and A_{H_2O} are the integrated absorbance for the OH peak at 4500 cm^{-1} and for the H_2O peak at 5200 cm^{-1}, respectively
ε^*_{HO}, and $\varepsilon^*_{H_2O}$ are the integrated extinction coefficients (L/mol.cm^2)

Values for the integrated extinction coefficients are 1.56 L/mol.cm^2 for ε^*_{HO} for the band at 4500 cm^{-1} and 1.79 L/mol.cm^2 for $\varepsilon^*_{H_2O}$ for the band at 5200 cm^{-1} determined for haplogranite compositions at room temperature (Behrens, 1995; Nowak and Behrens, 1995).

2.3.4. Raman spectroscopy

Raman spectroscopic measurements of samples were mainly performed at Tübingen University on a LABRAM2 spectrometer equipped with a Peltier cooled CCD detector and Olympus optical microscope BX-40, adjustable x-y table, and gratings with 600 and 1800 mm^{-1} grid. The measurements were carried out mainly using the green line (514 nm) of an external Ar-ion laser and the red line (632.8 nm) of an internal He-Ne-laser. Most of the run products were quite fluorescent samples. The blue (488 nm) and green (514 nm) line of the argon laser caused strong fluorescence in most of the samples containing xenotime and swamped any underlying Raman spectrum to such an extent that it was no longer detectable. In these cases, a red laser (632.8 nm and power of 0.4 mW) was used to examine the sample, but the fluorescence was still observed for samples containing $HoPO_4$ and $ErPO_4$ xenotime crystals. These two samples needed to be measured with a near infrared (NIR) laser (785 nm diode). However, this reduced the scattering intensity, so longer integration times were required.

3. Results

3.1. The influence of phosphorus on the solubility of monazite in haplogranitic melts

A series of experiments was carried out to study the effect of phosphorus concentration in the melt on the solubility of monazite. Experiments were carried out at 800°C and 2 kbar starting with pure $GdPO_4$ monazite and hydrous glasses with ASI= 0.8 or ASI = 1.0, containing variable phosphorus contents ranging from 0.1 to 1.5 wt.%. In all successful experiments, beside hydrous glass, monazite was the only phases identified in all run products. Mica appeared accidentally in experiment 4P75 and was confirmed by Raman and XRD powder diffraction analyses (Figure 3.1).

The mica crystals were very small and less than 1-2 μm in size. The concentration of water in the final solubility experiments was assumed to be the same, as in the hydrated glasses used as starting material, ie. about 6 wt.% H_2O. Glasses are homogenous as indicated by low standard deviations of the major element analyses (Table 3.1). Mass balance calculations of the major element melt composition indicate a small Na-loss, which could be an artifact of the microprobe analysis.

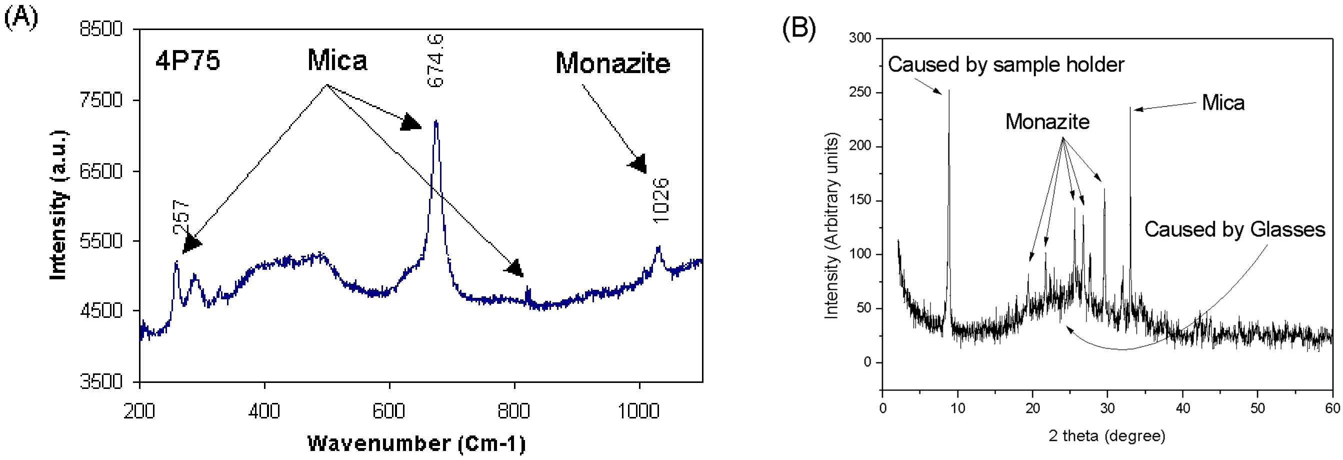

Figure 3.1. Phase identification of mica from sample 4P75 (A) Raman spectrum obtained using a Labram2 spectrometer equipped with Olympus microscope with a red laser at 632.8 nm and (B) XRD result.

The compositions of the run products obtained by EMPA are given in Table 3.1. The relative error limits tabulated with each analytical value are those estimated from the standard deviation (1σ) of replicated analysis. The experimental data at 800°C, 2 kbar and water saturated conditions showed that monazite/xenotime solubilities are a function of phosphorous content in the melt. In addition, there is a contrast between the behaviour of REE in peralkaline and metaluminous melt. The dependence of solubility on phosphorous is less pronounced as compared to the effects of ASI. At metaluminous melt composition (ASI = 1), the solubility of monazite decreases continuously from low phosphorous concentration (P_2O_5 = 0.1wt.%; Gd = 527ppm) to higher phosphorous content (P_2O_5 = 1.5 wt.%; Gd_2O_3 = 261ppm).

Table 3.1. Experimental data on the solubility of $GdPO_4$ in haplogranitic melts (ASI = 0.8 and ASI = 1) with variable phosphorus content at 800^oC and 2 kbar as derived from average microprobe analyses of quenched glasses.

Run No.	Run duration	Starting materials [a]	Run products (wt.%)								n	Phases[b]	Ksp[c]
			Na_2O	K_2O	Al_2O_3	SiO_2	P_2O_5	Gd_2O_3	Total	ASI			$(10^{-5}$ mol^2/kg$^2)$
2P10	30	G81 + $GdPO_4$	5.10±0.09	4.13±0.05	10.74±0.12	73.42±0.38	0.116±0.021	0.158±0.006	93.68±0.30	0.84±0.016	24	M	14.22±2.63
2P25	31	G82 + $GdPO_4$	6.00±0.10	4.39±0.03	10.77±0.09	71.90±0.96	0.307±0.015	0.102±0.008	93.47±1.00	0.74±0.011	19	M	24.40±1.98
2P50	31	G83 + $GdPO_4$	5.67±0.17	4.28±0.03	10.69±0.08	73.42±0.83	0.530±0.035	0.077±0.010	94.67±0.91	0.77±0.017	20	M	31.87±5.18
2P75	31	G84 + $GdPO_4$	6.11±0.11	4.29±0.03	10.64±0.10	73.38±1.09	0.791±0.047	0.057±0.013	95.26±1.21	0.73±0.010	30	M	35.14±8.20
2P100	31	G85 + $GdPO_4$	6.01±0.10	4.19±0.03	10.57±0.05	74.28±0.51	1.006±0.042	0.051±0.009	96.11±0.50	0.74±0.010	25	M	39.68±6.75
2P150	31	G86 + $GdPO_4$	5.99±0.13	4.10±0.03	10.28±0.06	73.15±0.82	1.504±0.049	0.050±0.010	95.08±0.85	0.72±0.012	41	M	58.23±11.2
4P10	30	G101 + $GdPO_4$	4.09±0.12	3.51±0.06	12.12±0.19	73.78±0.99	0.115±0.013	0.056±0.014	93.80±1.19	1.16±0.022	25	M	5.44±1.13
4P25	31	G102 + $GdPO_4$	5.07±0.30	3.92±0.15	12.21±0.11	73.26±1.07	0.250±0.035	0.049±0.010	94.78±1.15	0.98±0.065	25	M	9.71±1.59
4P50	31	G103 + $GdPO_4$	5.01±0.16	3.90±0.04	11.97±0.09	73.54±0.57	0.499±0.030	0.042±0.013	94.96±0.63	0.97±0.024	30	M	15.99±5.76
4P75	30	G104 + $GdPO_4$	5.03±0.18	3.90±0.05	11.92±0.09	74.41±0.59	0.751±0.046	0.036±0.008	94.85±0.70	0.96±0.020	6	M, Mi	20.67±1.68
4P100	31	G105 + $GdPO_4$	5.15±0.15	3.77±0.05	11.77±0.09	73.84±0.67	1.002±0.043	0.035±0.009	95.56±0.76	0.94±0.022	31	M	26.88±6.52
4P150	31	G106 + $GdPO_4$	4.92±0.14	3.68±0.04	11.23±0.09	73.48±0.75	1.516±0.057	0.029±0.009	94.86±0.82	0.94±0.021	21	M	35.39±9.84

[a] *Starting materials: 90 wt.% water-saturated haplogranite, i.e. contained about 6 wt.% H_2O (Glasses G81-G106) + 10 wt.% pure single rare earth phosphate crystals ($GdPO_4$).*

[b] *Phases other than glass present in melt: M – monazite and Mi - mica*

[c] *Solubility products (* Ksp*) for reaction* $REEPO_4^{melt} \Leftrightarrow REE^{melt} + PO_4^{melt}$

Table 3.2. Calculated speciation of $GdPO_4$ (molecular $GdPO_4$ or Gd^{3+}) dissolved in haplogranitic melt at 800^oC and 2 kbar derived from average EMPA data

Run No.	Aver. P_2O_5 *$(10^{-2}$ mol/kg$)$*	Total Gd solubility in melt *(ppm)*	Solubility products (Ksp)* *$(10^{-5}$mol^2/kg$^2)$*	Gd solubility $(10^{-3}$ mol/kg) in:		Mol fraction (MF) between	
				Ion (3+)	*Molecular*	*Gd (3+)*	*Gd (molecular)*
2P10	0.81±0.15	1374±50	14.22±*2.63*	6.21	2.52	0.71	0.29
2P25	2.16±0.10	889±69	24.40±*1.98*	3.13	2.52	0.55	0.45
2P50	3.74±0.25	668±86	31.87±*5.18*	1.72	2.52	0.41	0.59
2P75	5.57±0.33	496±99	35.14±*8.20*	0.63	2.52	0.20	0.80
2P100	7.09±0.29	440±74	39.68±*6.75*	0.28	2.52	0.10	0.90
2P150	10.60±0.34	432±84	58.23±*11.2*	0.22	2.52	0.08	0.92
4P10	0.80±0.09	527±92	5.44±*1.13*	1.68	1.67	0.50	0.50
4P25	1.76±0.25	432±73	9.71±*1.59*	1.08	1.67	0.39	0.61
4P50	3.52±0.21	358±128	15.99±*5.76*	0.61	1.67	0.27	0.73
4P75	5.29±0.21	308±30	20.67±*1.68*	0.29	1.67	0.15	0.85
4P100	7.06±0.30	300±74	26.88±*6.52*	0.24	1.67	0.12	0.88
4P150	10.68±0.40	261±73	35.39±9.84	0.05	1.67	0.03	0.97

* *Solubility product (Ksp) for reaction* $REEPO_4^{melt} \Leftrightarrow REE^{melt} + PO_4^{melt}$

This variation is more clearly seen in the peralkaline composition, where the solubility of monazite is 2-3 times higher than in metaluminous melt at the same phosphorous concentration and decreases significantly from 1374 ppm Gd at P_2O_5 = 0.1 wt.% to 432 ppm Gd at P_2O_5 = 1.5 wt.%.

The line scans and selected mapping measurements showed that the concentration of REE in the melt decreased away from the crystal/melt interface in the experiments even after run durations of 30-64 days demonstrating that the attainment of equilibrium is extremely sluggish. However, the concentration profile of P_2O_5 in glass was much less pronounced, because the amount of P resulting from monazite/xenotime dissolution was low in comparison with the P initially added. Ideally, the best way to demonstrate attainment of equilibrium would be to reverse the experiments (i.e., to also approach equilibrium from crystallization experiments). We did not attempt to reverse these series of experiments out of concern that the equilibrium would not be reached due to slow diffusion kinetics. In order to obtain better estimates of equilibrium solubility, we extrapolated the diffusion profiles observed around a monazite crystal to the crystal/melt interface. According to Rapp and Watson (1986), the dissolution of monazite and xenotime in silicate melt follows Fick's second law of diffusion (Eq. 3.1):

$$C_{x,t} = C_o erfc(\frac{X}{\sqrt{4Dt}}) \qquad \text{(Eq. 3.1)}$$

Where Cx,t is the concentration of diffusion at a distance X (cm) from the interface at time t (s), Co is the concentration at the interface (i.e. the saturation level for the diffusing species), and D is the diffusivity (cm^2/s).

The data can be linearized by inversion through the error function, and the concentration data are recast as:

$$\frac{X}{\sqrt{4Dt}} = \frac{1}{erfc(1-\frac{C_{x,t}}{C_o})} \qquad \text{(Eq. 3.2)}$$

This model requires that one first estimates the value of Co and then the inverse error function for each value of $(1-\frac{C_{x,t}}{C_o})$ is plotted against X. The best-fit line to the data is then determined by the cubic least square regression method. Co at the intercept closest to zero is the best estimate of the saturation concentration. The slope of the best-fit line determined in the manner will be equal to $\frac{1}{\sqrt{4Dt}}$, and since time t is known, the diffusivity D can be directly calculated.

The extrapolation of experimental data using this model can provide information on saturation concentration and diffusivity, which are summarized in Table 3.3. Examples are illustrated in Figure 3.2 and Figure 3.3. Not all concentration profiles could be fitted accurately by the solution of Fick's law, however, the general trend was almost close to the error function. This is due to the fact that the run products contained many small rare earth phosphate crystals (20-150 µm) throughout the quenched melt, leading to interference between the Gd content released from different crystals. The concentration of Gd along the profile was sometimes controlled by other crystals around, not only two crystals at both ends of the profile. In addition, the run duration was relatively long, so that the concentration of REE was already close to equilibrium. In any case, even if the concentration profiles did not always fit well to the theoretical function, the maximum Gd concentration in the glass at the interface, corresponding to the equilibrium solubility value, is quite well constrained. From the dependence of $GdPO_4$ solubilities on P_2O_5 content, some general inferences can be drawn on the speciation of rare earth elements in silicate melts.

Table 3.3. Experimental data (Co) on the solubility of $GdPO_4$ in haplogranitic melts (ASI = 0.8 and ASI = 1) with variable phosphorus content at 800°C and 2 kbar as derived from the extrapolation of measured diffusion profiles.

Run No.	P_2O_5	Co (Gd)[a]	Diffusivities	R^2 (COD)[b]	*Ksp*[c]
	10^{-2} mol/kg	ppm	10^{-11} cm^2/s		*(10^{-5}mol^2/kg^2)*
2P10	0.81±0.15	1496±48	16.32±81.6	0.18	15.48±0.09
2P25	2.16±0.10	1252±48	11.11±3.75	0.44	34.44±0.06
2P50	3.74±0.25	1009±73	7.12±2.87	0.33	47.96±0.23
2P75	5.57±0.33	902±74	2.66±0.85	0.33	63.88±0.31
2P100	7.09±0.29	837±58	3.82±1.30	0.19	75.48±0.22
2P150	10.60±0.34	648±44	5.99±2.28	0.49	87.33±0.19
4P10	0.80±0.09	863±145	4.07±3.38	0.24	8.82±0.16
4P25	1.76±0.25	783±64	3.63±1.54	0.27	17.54±0.20
4P50	3.52±0.21	737±115	1.64±0.92	0.17	32.97±0.31
4P75	5.29±0.21	698±72	3.69±1.65	0.39	46.96±0.19
4P100	7.06±0.30	554±77	2.27±1.23	0.19	49.74±0.30
4P150	10.68±0.40	669±71	1.19±0.37	0.40	90.94±0.36

[a] *Co (Gd) is the estimated saturation concentration of Gd in ppm at the interface between monazite crystal and melts*

[b] *The coefficient of determination (COD) or R^2*

[c] *Solubility product for reaction* $REEPO_4^{melt} \Leftrightarrow REE^{melt} + PO_4^{melt}$

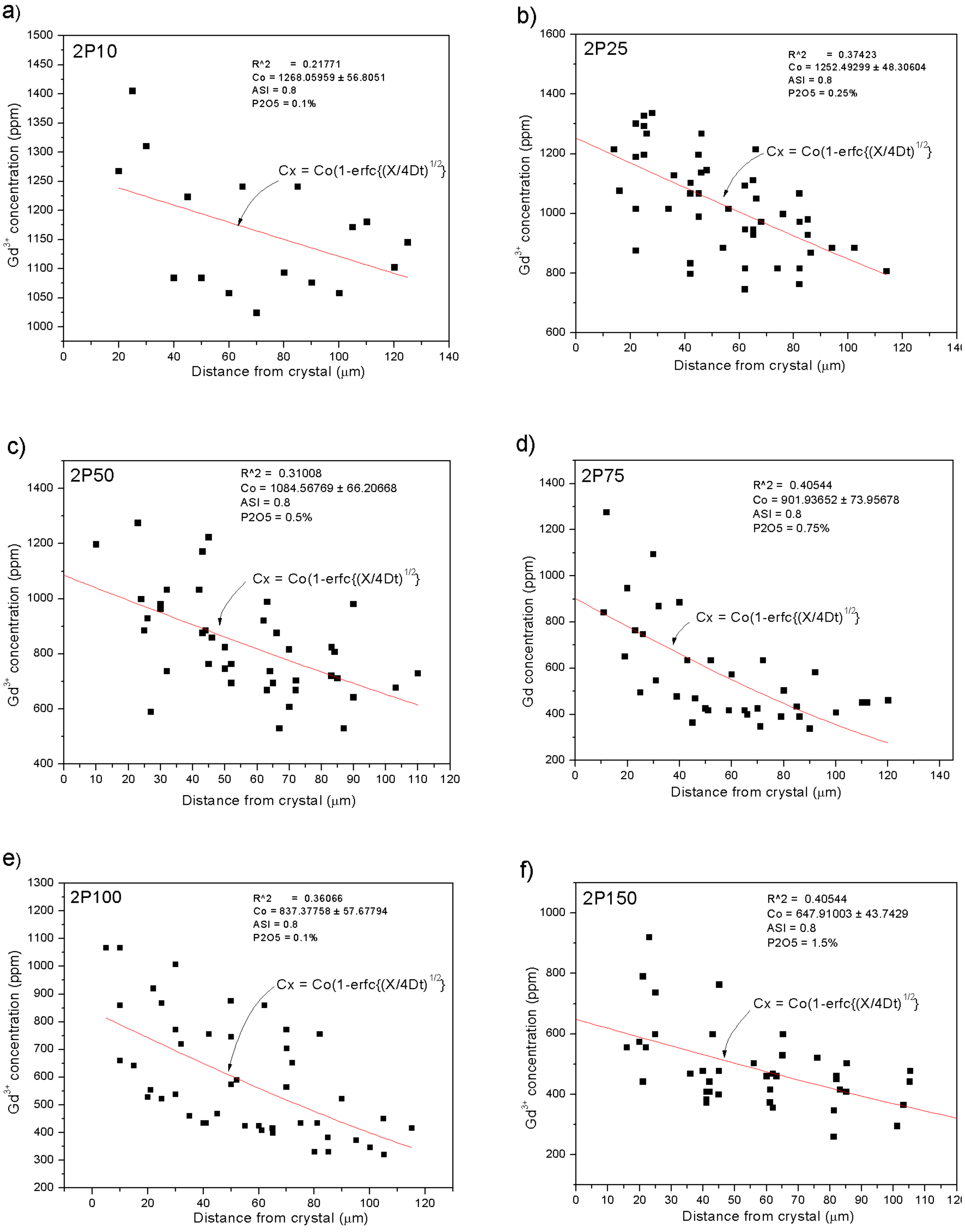

Figure 3.2. Gadolinium concentration profile in glass adjacent to a monazite crystal at 800°C and 2 kbar for 30-31 days. The solid curve represents the best-fit line of the diffusion model. The model provides an estimated saturation concentration of REE (Co) in alkaline haplogranite (ASI =0.8)

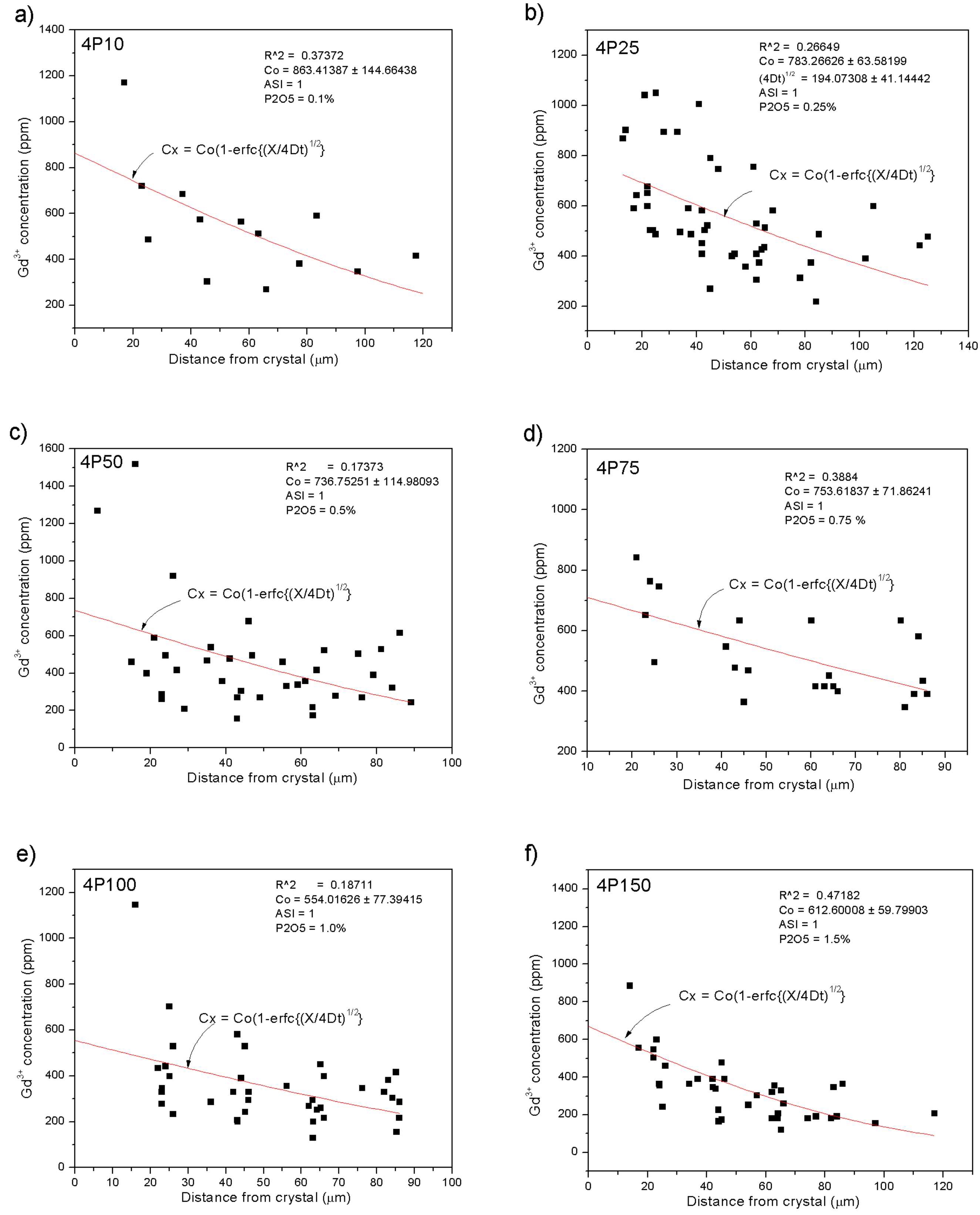

Figure 3.3. Gadolinium concentration profile in glass adjacent to a monazite crystal at 800°C and 2 kbar for 30-31 days. The solide curve represents the best-fit line of the diffusion model. The model provides an estimated saturation concentration of REE (Co) in metaluminous haplogranite (ASI =1)

In a silicate melt, the rare earth phosphates may either dissolve as undissociated species, or they may dissociate into rare earth and phosphate ions. In the most general case, both types of species will coexist. This can be treated in the following way by considering two equilibria:

$$REEPO_4^{solid} = REEPO_4^{melt} \qquad \text{(Eq. 3.3)}$$

$$K_1 = \frac{a(REEPO_4^{melt})}{a(REEPO_4^{solid})} = a\left(REEPO_4^{melt}\right) \qquad \text{(Eq. 3.4)}$$

$$REEPO_4^{melt} = REE_{melt}^{3+} + PO_{4melt}^{3-} \qquad \text{(Eq. 3.5)}$$

$$K_2 = \frac{a(REE_{melt}^{3+})(PO_{4melt}^{3-})}{a(REEPO_{4melt})} = \frac{1}{K_1} a(REE_{melt}^{3+})(PO_{4melt}^{3-}\quad) \qquad \text{(Eq. 3.6)}$$

with K = equilibrium constant, a = activities and because in our experiments, rare earth phosphate crystals is pure ($REEPO_4$), a($REEPO_4$) = 1. We now approximate activities a by concentrations []

$$[\mathrm{REE}_{\text{total in melt}}] = [\mathrm{REEPO}_{4\ \text{melt}}] + [\mathrm{REE}^{3+}_{\text{melt}}] = K_1 + K_1 K_2 \frac{1}{\left[PO_{4melt}^{3-}\right]} \qquad \text{(Eq. 3.7)}$$

Therefore, if we plot the REE concentration in the melt versus the inverse of the P concentration in the melt, we should get a straight line. The intercept with the Y-axis gives K_1, the slope of the line K_1 K_2.

The application of Eq. 3.7 is illustrated in Figure 3.4 and Table 3.2. There is again a contrast between peralkaline and metaluminous melt compositions with the equilibrium constant for the solubility of undissociated species (K_1) as 397 ppm (2.52 x10^{-3}mol/kg) and 262 ppm (1.67 x10^{-3}mol/kg), respectively. The dissociation constant K_2 for peralkaline melts (24.02 x10^{-3}mol/kg) is two times higher than that for metaluminous melts (10.30x10^{-3}mol/kg). This means that the rare earth phosphates are more dissociated into REE^{3+} and PO_4^{3-} in peralkaline melts than in metaluminous melts and the higher abundance of ionic species is the main reason for the increase of solubility with peralkalinity. The fraction of Gd dissolved as molecular $GdPO_4$ and as ionic Gd^{3+} species are given for each experiment in Table 3.2 and Figure 3.4 show the same exercise using the rare earth solubility data obtained by extrapolating the diffusion curves around dissolving crystals Table 3.4 and Figure 3.5.

Figure 3.4 clearly shows that the REE content of a silicate melt in equilibrium with monazite depends on the phosphorus content of the melt. The effect of phosphorus on the equilibrium REE concentration is higher for peralkaline than for metaluminous melts. This reflects the fact that in metaluminous melts, the degree of dissociation of $REEPO_4$ in the melt into REE^{3+} and PO_4^{3-} is smaller than for peralkaline melts. If the solubility of monazite is therefore given in ppm of REE or a similar number, such “solubilities” can only be directly compared if the P_2O_5 contents of the corresponding melts are identical.

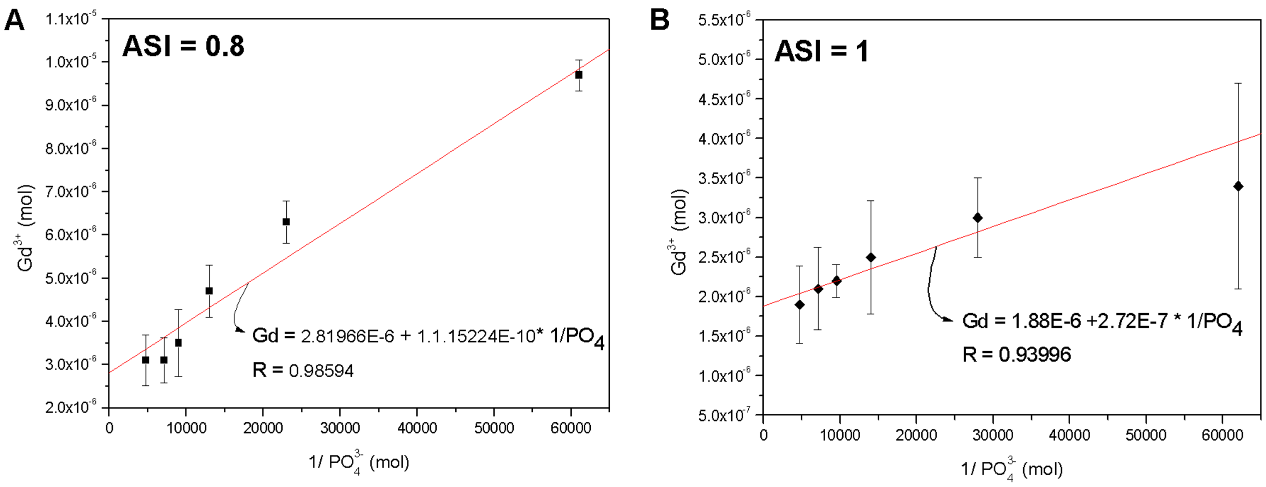

Figure 3.4. Plot of the average phosphate vs. average REE concentration for solubility experiments of monazite in haplogranite. A) peralkaline (ASI = 0.8) and B) metaluminous (ASI = 1) melt composition. The straight line is a fit linear function of y = A + B/x, where x being phosphate concentration, y being a rare earth concentration, and A is the equilibrium constant K1, while B is the product of K1 and K2. Fit function used only data of this study.

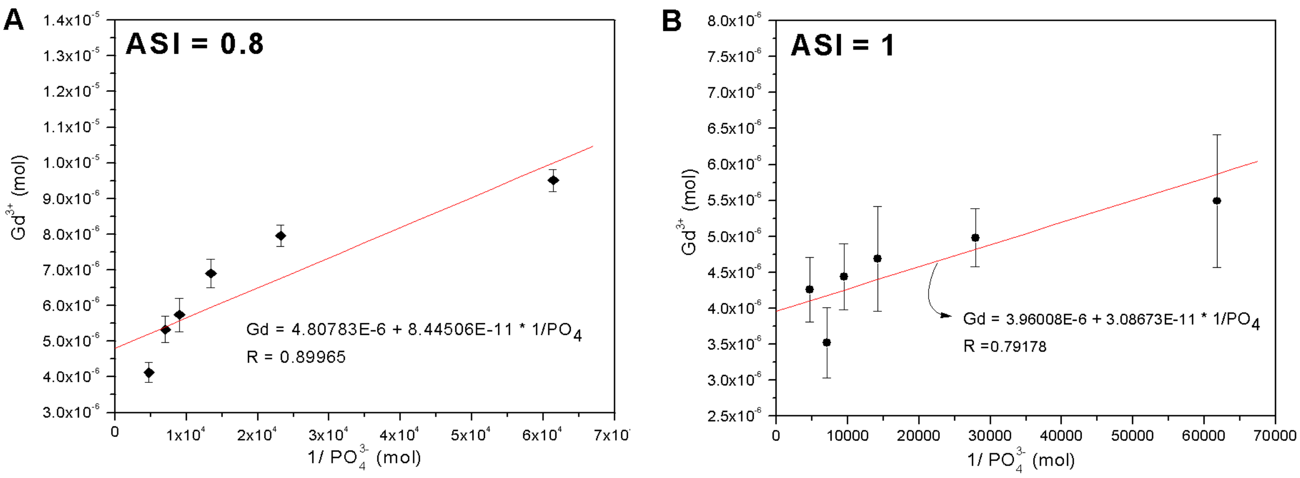

Figure 3.5. Plot of the average phosphate vs. estimated saturation REE concentration for solubility experiments of monazite in haplogranites. A) peralkaline (ASI = 0.8) and B) metaluminous (ASI = 1) melt composition. The straight line is a fit linear function of y = A + B/x, where x being phosphate concentration, y being a rare earth concentration, and A is the equilibrium constant K1, while B is the product of K1 and K2

Figure 3.6 illustrates that the solubility product alone does not appropriately describe the solubility of monazite either. The solubility product is not constant, but it appears to increase with the P_2O_5 content of the melt. This is due to the fact that molecular $GdPO_4$ contributes significantly to the bulk solubilities.

3.2. *The effect of the alkali/aluminium ratio on monazite and xenotime solubility in haplogranitic melts*

This series of experiments was performed to study the effect of the alkali/aluminum ratio of the melt on the solubility of monazite and xenotime. Experiments were carried out at 800°C and 2 kbar.

Table 3.4. Estimated saturation concentration Gd in melt and calculated values of mol fraction of rare earth phosphate solubility in silicate melts, coordination with phosphor at 800°C and 0.2GP.

Run No.	Gd solubility (10^{-3} mol/kg) in		Mol fraction between	
	Ion (3+)	Molecular	Gd (3+)	Gd (molecular)
2P10	*4.67*	4.83	0.49	0.51
2P25	*2.07*	4.83	0.30	0.70
2P50	*0.90*	4.83	0.16	0.84
2P75	*0.90*	4.83	0.16	0.84
2P100	*0.49*	4.83	0.09	0.91
2P150		4.83		
4P10	*1.48*	4.01	0.27	0.73
4P25	*0.98*	4.01	0.20	0.80
4P50	*0.68*	4.01	0.15	0.85
4P75	*0.44*	4.01	0.10	0.90
4P100		4.01		
4P150	*0.25*	4.01	0.06	0.94

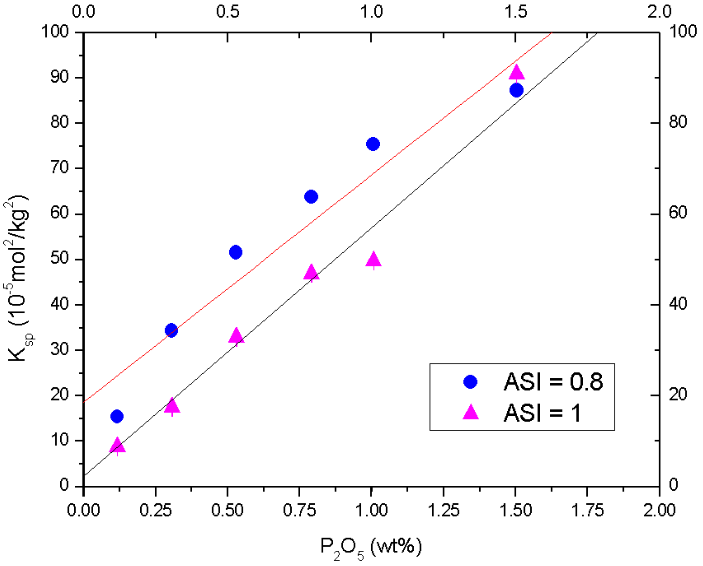

Figure 3.6. The effect of P_2O_5 on the apparent solubility product of monazite in water saturated haplogranite melt at 2 kbar and 800°C. ASI refers to the molar Al/(Na+K) of the melt. The error bars (1σ) are smaller than the symbol size.

starting with pure phosphates of one rare earth element and hydrous glasses with ASI ranging from 0.7 to 1.2. Most experiments were carried out with a run duration of one month, but one series of experiments was also carried out with two months run duration. As additional test for equilibrium, a series of reversed experiments was carried out, where the samples were first run at 1100°C for one week and then re-run at 800°C for two months. In all experiments, the hydrous glasses contained 0.1 wt. % P_2O_5 at the beginning of the run. Monazite was the starting materials for all runs with LREE, while xenotime was used for other runs with HREE. The starting material for $GdPO_4$ solubility experiments consisted of a mixture of $GdPO_4$ with monazite and xenotime structure.

The results of this series of experiments are summarized in Table 3.5. The homogeneity of the glasses can be seen from the low standard deviations. There is no significant difference in major element composition between starting hydrous glass and the glasses of the final run products. The water content was not determined directly, but was assumed to be the same as the water content of the hydrous haplogranite glasses used as starting material (about 6 wt.%). Run products contained mainly hydrous glass and monazite for runs with LREE or xenotime for runs with HREE, respectively. In some cases, others phases such as mica (Mi), alkali feldspar (Fk) or quartz (Q) were present in small quantities. These phases appeared in sample MH104, a not fully successful run; they may have formed when pressure decreased from 2 kbar to about 1.8 kbar due to the expansion of the bomb.

Successful runs of the 1 month series lasted from 29 to 38 days and the successful runs of the 2 months series lasted 60-64 days. Five runs MH101, MH104, MH112, MH212 and MH213, which were not fully successfully, were also used in this study. These runs were terminated earlier than other runs due to the expansion of the bomb. The runs number MH101 and MH112 ended after 24 and 25 days, and the runs number MH212 and MH213 ended after 26 and 27 days, respectively. Run number MH104 ended after 28 days. They were all quenched at about 1.8 kbar instead of 2 or 2.5 as usual. The capsules were in good condition after the run and showed no weight loss, except capsule MH104, which was visibly broken after the experiment. It probably had ruptured at the time of the bomb expanded, since the capsule was inflated. The samples that were quenched at 2 kbar or less contained larger bubbles, leading to more scatter in the EMPA analyses using a defocused beam. Most of the capsules gained a small amount of weight (< 0.4 wt.%) during the run, probably due to uptake of nickel.

Chemical analyses of the run products showed that the relative proportion of Na, K, Al and Si were virtually identical to the hydrous starting materials. The ASI varies slightly as compared to the starting material values. These variations were mainly observed in the not fully successful runs or in the samples that were quenched at 2 kbar or less. For example, in the series of experiment at ASI = 0.7, the runs MH104 and MH112 were quenched at 1.8 kbar and the ASI in the quenched glasses was higher than normal, possibly due to errors during analysis caused by bubbles in the samples or due to alkali loss to the fluid during the exsolution of water (Table 3.5 and Table 3.6).

Table 3.5. Experimental data on the solubility of rare earth phosphates (monazite and xenotime) in haplogranitic melts with variable alkali saturation index (ASI) at 800°C and 2 kbar as derived from average microprobe analyses of quenched glasses.

No.	Starting material[a]		Runs	Quench pressure	Na_2O	K_2O	Al_2O_3	SiO_2	P_2O_5	REE_2O_3	Total	n	ASI[b]	Phases[c]	Ksp[d]
	Mix	*Formula*	*Days*	*Kbar*	*(%)*	*(%)*	*(%)*	*(%)*	*(%)*	*(%)*	*(%)*				*(10^{-5} mol^2/kg^2)*
MH101	G1+M	$LaPO_4$	24	1.8	5.23±0.08	5.31±0.03	10.38±0.04	72.31±0.19	0.34±0.01	0.025±0.005	93.63±0.22	25	0.73±0.01	M, Mi, Q	7±2
MH102	G1+M	$CePO_4$	30	2	4.36±1.03	5.35±0.07	10.90±0.42	74.62±2.06	0.16±0.01	0.103±0.011	95.54±1.39	17	0.74±0.01	M, Q	14±2
MH103	G1+M	$PrPO_4$	31	2	5.16±0.05	5.32±0.06	10.39±0.09	71.00±0.80	0.15±0.02	0.138±0.018	92.19±0.86	26	0.74±0.01	M	18±2
MH104	G1+M	$NdPO_4$	28	1.8	4.51±0.21	4.86±0.04	10.43±0.18	71.60±1.00	0.11±0.02	0.391±0.038	91.85±1.23	23	0.83±0.03	M	36±7
MH106	G11+M	$SmPO_4$	30	2.5	4.92±0.13	5.30±0.04	10.43±0.04	72.51±0.16	0.20±0.02	0.248±0.014	93.68±0.17	26	0.76±0.01	M	41±5
MH107	G1+M	$EuPO_4$	29	2	5.22±0.07	5.34±0.02	10.41±0.03	70.93±0.49	0.26±0.02	0.336±0.012	92.54±0.52	10	0.73±0.01	M	69±5
MH108	G1+M/X	$GdPO_4$	33	2	5.55±0.19	5.69±0.19	11.20±0.20	71.35±0.66	0.23±0.02	0.632±0.028	94.71±0.56	26	0.74±0.01	M, X	115±11
MH109	G1+X	$TbPO_4$	31	2	4.55±0.25	5.10±0.13	10.60±0.21	72.96±0.91	0.27±0.02	0.283±0.012	93.80±1.37	26	0.82±0.03	X, Fk	58±5
MH110	G11+X	$DyPO_4$	30	2.5	5.27±0.09	5.32±0.03	10.42±0.07	72.27±0.29	0.34±0.03	0.547±0.007	94.21±0.36	26	0.73±0.01	X	139±10
MH111	G11+X	$HoPO_4$	30	2.5	5.37±0.09	5.35±0.06	10.62±0.04	72.48±0.16	0.36±0.02	0.666±0.034	94.90±0.22	26	0.73±0.01	X	176±13
MH112	G1+X	$ErPO_4$	23	1.8	4.25±0.90	5.16±0.07	10.48±0.14	71.77±0.65	0.29±0.06	0.464±0.100	92.61±0.86	26	0.81±0.03	X	100±33
MH113	G11+X	$TmPO_4$	30	2.5	5.16±0.18	5.37±0.05	10.60±0.07	72.85±0.28	0.38±0.03	0.759±0.062	95.15±0.37	26	0.75±0.02	X	209±24
MH114	G11+X	$YbPO_4$	35	2.5	5.20±0.16	5.40±0.08	10.44±0.10	72.25±1.21	0.37±0.02	0.927±0.044	94.61±1.29	24	0.73±0.02	X	244±19
MH115	G1+X	$LuPO_4$	31	2	5.08±0.14	5.35±0.10	10.63±0.18	74.60±2.21	0.44±0.03	0.849±0.029	94.58±1.26	26	0.75±0.01	X	263±26
MH201	G2+M	$LaPO_4$	30	2.5	4.78±0.23	4.30±0.09	10.96±0.10	73.33±0.28	0.37±0.04	0.019±0.009	93.77±0.57	25	0.88±0.03	M, Q	5.9±2.9
MH202	G12+M	$CePO_4$	31	2.5	4.83±0.08	4.36±0.03	10.94±0.06	73.50±0.36	0.12±0.01	0.043±0.008	93.81±0.42	26	0.87±0.01	M	4.4±0.8
MH203	G12+M	$PrPO_4$	31	2.5	4.92±0.07	4.21±0.05	11.50±0.30	72.40±0.81	0.13±0.02	0.030±0.008	92.72±0.91	26	0.87±0.01	M, Mi	3.3±1.0
MH204	G12+M	$NdPO_4$	31	2.5	4.74±0.09	4.29±0.05	11.03±0.08	73.31±0.55	0.12±0.02	0.058±0.022	93.57±0.66	26	0.89±0.01	M	6.0±2.6
MH206	G12+M	$SmPO_4$	31	2.5	4.18±1.47	3.72±1.30	10.58±3.72	73.66±0.35	0.15±0.01	0.065±0.022	94.35±0.40	16	0.98±0.01	M, Mi	7.3±2.4
MH207	G2+M	$EuPO_4$	30	2	5.17±0.08	4.42±0.04	11.54±0.30	72.95±0.88	0.15±0.02	0.137±0.027	93.75±1.08	26	0.85±0.01	M	16.5±4.2
MH208	G2+M/X	$GdPO_4$	32	2	4.61±0.28	4.43±0.04	11.64±0.27	74.62±0.06	0.16±0.02	0.158±0.010	95.61±0.07	25	0.95±0.05	M, X	19.8±2.5
MH209	G12+X	$TbPO_4$	31	2.5	4.76±0.17	4.42±0.07	10.78±0.05	73.61±0.29	0.19±0.02	0.139±0.015	93.93±0.44	26	0.86±0.02	X	20.8±2.9
MH210	G2+X	$DyPO_4$	30	2	6.12±0.29	4.69±0.09	11.71±0.04	76.45±0.20	0.18±0.02	0.212±0.031	99.39±0.41	26	0.78±0.03	M, Mi	28.6±7.0
MH211	G12+X	$HoPO_4$	31	2.5	5.14±0.04	4.55±0.08	11.64±0.14	74.95±0.20	0.18±0.02	0.231±0.022	95.73±0.37	26	0.88±0.01	X	31.2±3.8
MH212	G2+X	$ErPO_4$	26	1.8	4.12±0.62	5.10±0.11	10.67±0.26	72.08±0.87	0.20±0.05	0.257±0.100	92.61±1.19	26	0.88±0.06	X	38.1±22.4
MH213	G2+X	$TmPO_4$	27	1.8	4.81±0.09	4.35±0.03	11.06±0.07	73.27±0.40	0.19±0.01	0.236±0.011	93.93±0.50	21	0.88±0.01	X	32.8±2.51
MH214	G12+X	$YbPO_4$	30	2.5	4.67±0.19	4.36±0.06	10.90±0.06	73.40±0.89	0.19±0.02	0.356±0.057	93.89±0.94	26	0.89±0.02	X	49.1±11.1
MH215	G2+X	$LuPO_4$	29	2	5.02±0.08	4.33±0.06	11.37±0.24	71.83±0.40	0.22±0.02	0.339±0.028	93.13±0.62	24	0.88±0.02	X, Mi	52.1±8.01
MH301	G13+M	$LaPO_4$	31	2.5	4.50±0.10	4.10±0.07	11.64±0.09	73.22±0.19	0.38±0.09	0.016±0.008	93.86±0.29	18	0.99±0.02	M	5.43±3.28
MH302	G13+M	$CePO_4$	30	2.5	4.44±0.30	4.11±0.04	11.63±0.05	73.59±0.24	0.10±0.02	0.038±0.012	93.93±0.45	26	1.00±0.05	M	3.29±1.13
MH303	G13+M	$PrPO_4$	31	2.5	4.57±0.10	4.08±0.03	11.66±0.09	72.60±0.28	0.11±0.03	0.021±0.013	93.00±0.51	25	0.98±0.01	M	2.04±1.75
MH304	G13+M	$NdPO_4$	31	2.5	4.70±0.07	4.10±0.02	11.86±0.07	73.59±0.45	0.12±0.02	0.027±0.012	94.43±0.51	23	0.98±0.01	M	2.60±1.16
MH306	G13+M	$SmPO_4$	31	2.5	4.62±0.08	4.14±0.07	11.73±0.07	73.81±0.30	0.11±0.01	0.047±0.006	94.47±0.33	26	0.98±0.01	M, Fk	4.06±0.84
MH307	G3+M	$EuPO_4$	30	2	4.54±0.07	4.09±0.04	12.44±0.65	73.34±0.29	0.12±0.02	0.040±0.009	93.83±0.29	25	0.99±0.01	M	4.24±1.15
MH308	G3+M/X	$GdPO_4$	32	2	4.79±0.11	4.12±0.07	12.16±0.24	73.31±0.46	0.12±0.02	0.045±0.014	94.56±0.53	26	0.99±0.02	M, X	4.25±1.34
MH309	G13+X	$TbPO_4$	30	2.5	4.59±0.12	4.13±0.05	11.61±0.06	73.47±0.09	0.11±0.01	0.042±0.005	93.97±0.23	21	0.97±0.02	X	3.48±0.28
MH310	G13+X	$DyPO_4$	30	2.5	4.51±0.07	4.09±0.05	11.67±0.06	73.62±0.12	0.11±0.02	0.073±0.011	94.11±0.21	22	0.99±0.01	X	6.37±1.15
MH311	G13+X	$HoPO_4$	30	2.5	4.67±0.08	4.43±0.13	12.27±0.10	74.54±0.21	0.11±0.02	0.053±0.013	95.10±0.56	26	0.99±0.01	X	4.51±1.29
MH312	G13+X	$ErPO_4$	30	2.5	4.50±0.13	4.16±0.03	11.83±0.11	73.71±0.93	0.13±0.03	0.099±0.022	94.46±0.94	26	1.00±0.02	X	9.43±3.23
MH313	G13+X	$TmPO_4$	34	2.5	4.05±0.34	4.24±0.05	11.77±0.10	74.09±0.63	0.12±0.03	0.099±0.022	94.34±0.90	26	1.03±0.04	X	8.88±2.96
MH314	G13+X	$YbPO_4$	30	2.5	4.51±0.10	4.13±0.06	11.73±0.15	73.42±0.62	0.12±0.02	0.208±0.035	94.24±0.78	26	0.99±0.02	X	17.31±3.46
MH315	G3+M	$LuPO_4$	29	2	4.82±0.05	4.21±0.05	11.48±0.21	74.11±0.82	0.12±0.02	0.143±0.024	94.90±0.77	26	0.93±0.02	X	12.54±3.00

Table 3.5 *(Continued)*

No.	Starting material[a]		Runs	Quench pressure[b]	Na_2O	K_2O	Al_2O_3	SiO_2	P_2O_5	REE_2O_3	Total	n	ASI[c]	Phases[d]	Ksp[e]
	Mix	*Formula*	*Days*	*Kbar*	*(%)*	*(%)*	*(%)*	*(%)*	*(%)*	*(%)*	*(%)*				*(10^{-5} mol^2/kg^2)*
MH401	G4+M	$LaPO_4$	31	2.5	4.11±0.15	3.74±0.25	12.18±0.12	74.49±0.57	0.22±0.07	0.024±0.011	94.55±0.84	21	1.14±0.04	M, Mi	4.73±2.52
MH402	G14+M	$CePO_4$	38	2.5	4.05±0.06	4.22±0.06	12.18±0.08	74.34±0.10	0.12±0.03	0.046±0.009	94.70±0.13	26	1.09±0.01	M	4.90±1.19
MH403	G4+M	$PrPO_4$	30	2.5	3.96±0.74	3.59±0.11	12.10±0.07	72.23±0.41	0.11±0.02	0.028±0.015	91.96±0.73	26	1.14±0.01	M	2.68±1.70
MH404	G14+M	$NdPO_4$	31	2.5	4.22±0.07	3.98±0.03	12.45±0.07	74.81±0.32	0.11±0.02	0.025±0.013	95.43±0.41	26	1.11±0.01	M	2.36±1.26
MH406	G14+M	$SmPO_4$	30	2.5	3.95±0.10	3.92±0.04	11.60±0.07	74.29±0.14	0.11±0.01	0.059±0.009	93.97±0.26	26	1.09±0.02	M	5.53±1.12
MH407	G14+M	$EuPO_4$	30	2.5	3.78±0.19	3.52±0.07	12.07±0.15	73.67±0.71	0.12±0.02	0.047±0.015	93.34±1.02	20	1.21±0.04	M	4.38±1.47
MH408	G4+M/X	$GdPO_4$	30	2.5	4.08±0.09	4.02±0.06	11.56±0.18	73.85±0.92	0.12±0.01	0.057±0.015	93.82±1.17	26	1.05±0.02	M, X	5.25±1.73
MH409	G4+X	$TbPO_4$	30	2.5	4.07±0.20	3.95±0.13	11.90±0.41	74.64±2.22	0.13±0.03	0.044±0.016	94.86±2.92	26	1.09±0.01	X	4.17±1.41
MH410	G4+X	$DyPO_4$	30	2.5	4.82±0.25	4.15±0.05	13.22±0.08	73.29±0.29	0.12±0.01	0.055±0.018	95.63±0.55	25	1.06±0.02	X	4.71±1.55
MH411	G4+X	$HoPO_4$	31	2.5	4.08±0.07	3.85±0.06	11.97±0.07	74.63±0.36	0.11±0.02	0.045±0.015	94.84±0.49	26	1.11±0.01	X	3.68±1.65
MH412	G14+X	$ErPO_4$	30	2.5	4.21±0.07	4.00±0.05	12.23±0.12	74.63±0.77	0.11±0.02	0.065±0.021	94.64±0.56	24	1.09±0.02	X	4.71±1.88
MH413	G14+X	$TmPO_4$	30	2.5	3.95±0.28	3.38±0.21	11.90±0.13	76.95±0.42	0.10±0.02	0.085±0.011	96.04±1.00	20	1.16±0.05	X	6.52±1.50
MH414	G14+X	$YbPO_4$	30	2.5	4.01±0.15	3.48±0.06	11.84±0.18	74.30±0.96	0.10±0.02	0.139±0.019	94.32±1.00	22	1.15±0.03	X	9.65±2.42
MH415	G14+X	$LuPO_4$	31	2.5	4.14±0.07	3.91±0.04	11.67±0.08	72.94±0.71	0.11±0.02	0.117±0.025	93.02±0.80	26	1.06±0.01	X	9.15±2.61
MH501	G5+M	$LaPO_4$	30	2.5	4.00±0.09	3.77±0.06	12.42±0.14	73.83±0.72	0.26±0.16	0.018±0.009	94.32±0.77	23	1.17±0.01	M, Q	4.14±2.85
MH502	G15+M	$CePO_4$	31	2.5	3.86±0.12	3.91±0.20	12.41±0.08	73.60±0.21	0.10±0.01	0.037±0.016	93.78±0.21	25	1.15±0.00	M	3.27±1.54
MH503	G15+M	$PrPO_4$	31	2	4.03±0.07	3.87±0.08	12.82±0.15	74.67±1.18	0.13±0.03	0.023±0.009	95.05±0.83	25	1.19±0.02	M	2.54±1.05
MH504	G15+M	$NdPO_4$	31	2.5	4.03±0.09	4.03±0.03	12.37±0.22	71.47±1.53	0.11±0.01	0.026±0.011	91.76±1.76	24	1.13±0.02	M	2.37±1.06
MH506	G15+M	$SmPO_4$	30	2.5	4.01±0.08	3.95±0.04	12.30±0.04	74.15±0.28	0.11±0.02	0.061±0.011	94.39±0.50	26	1.14±0.01	M	5.29±1.59
MH507	G5+M	$EuPO_4$	33	2.5	4.00±0.10	4.14±0.10	12.12±0.06	73.16±0.44	0.13±0.03	0.034±0.015	93.69±0.54	26	1.10±0.01	M	3.68±1.84
MH508	G5+M/X	$GdPO_4$	30	2	3.83±0.17	4.22±0.11	12.15±0.19	74.15±0.60	0.12±0.01	0.032±0.015	94.54±0.86	25	1.13±0.04	M, X	2.89±1.49
MH509	G5+X	$TbPO_4$	30	2.5	3.78±0.09	3.84±0.05	12.18±0.11	75.69±1.06	0.12±0.03	0.057±0.019	95.71±0.94	25	1.18±0.01	X	5.30±2.36
MH510	G5+X	$DyPO_4$	30	2.5	4.01±0.08	3.42±0.04	12.20±0.07	74.32±0.18	0.11±0.02	0.039±0.026	94.14±0.29	21	1.19±0.02	X	3.84±2.30
MH511	G5+X	$HoPO_4$	30	2.5	3.73±0.13	3.91±0.14	12.06±0.24	74.69±0.63	0.11±0.01	0.026±0.011	94.03±0.45	25	1.16±0.04	X	2.15±0.86
MH512	G15+X	$ErPO_4$	27	2.5	4.01±0.07	3.83±0.05	12.31±0.07	74.33±0.24	0.10±0.02	0.065±0.019	94.68±0.31	22	1.15±0.02	X	5.07±1.91
MH513	G5+X	$TmPO_4$	31	2.5	3.82±0.08	3.74±0.08	12.50±0.06	73.59±0.25	0.11±0.02	0.085±0.027	93.87±0.30	21	1.22±0.02	X	6.82±1.95
MH514	G15+X	$YbPO_4$	29	2.5	3.91±0.12	3.84±0.11	12.44±0.12	73.55±1.06	0.11±0.03	0.144±0.021	93.82±1.23	26	1.18±0.02	X	11.13±3.53
MH515	G5+X	$LuPO_4$	31	2	4.02±0.12	3.68±0.03	12.74±0.20	73.03±0.54	0.11±0.02	0.090±0.049	93.72±0.75	22	1.21±0.03	X	7.22±4.66
MH601	G16+M	$LaPO_4$	30	2.5	3.67±0.07	3.58±0.05	12.65±0.17	73.27±0.68	0.21±0.08	0.022±0.010	93.46±0.89	25	1.28±0.02	M	3.77±2.14
MH602	G16+M	$CePO_4$	31	2.5	3.68±0.16	3.76±0.20	12.81±0.07	73.81±0.21	0.11±0.02	0.047±0.009	94.14±0.25	26	1.24±0.01	M	4.32±0.97
MH603	G16+M	$PrPO_4$	30	2.5	3.70±0.28	3.39±0.19	12.60±0.32	71.37±1.51	0.13±0.02	0.031±0.016	93.69±2.10	25	1.30±0.07	M	3.34±1.55
MH604	G16+M	$NdPO_4$	30	2.5	3.72±0.09	3.54±0.04	13.07±0.06	74.14±0.21	0.11±0.01	0.034±0.013	94.64±0.33	26	1.32±0.02	M	3.19±1.17
MH606	G16+M	$SmPO_4$	30	2.5	3.67±0.12	3.58±0.04	12.86±0.05	73.31±0.25	0.12±0.02	0.068±0.011	93.52±0.52	26	1.30±0.03	M	6.61±1.33
MH607	G16+M	$EuPO_4$	33	2.5	3.81±0.15	3.63±0.03	13.05±0.05	73.96±0.78	0.12±0.02	0.049±0.018	94.69±0.72	25	1.29±0.03	M	4.57±2.17
MH608	G6+M	$GdPO_4$	30	2	3.68±0.08	3.60±0.08	12.62±0.11	73.22±0.49	0.12±0.01	0.069±0.014	93.38±0.65	25	1.28±0.02	M, X	6.69±1.55
MH609	G16+M	$TbPO_4$	30	2.5	3.63±0.15	3.52±0.06	12.88±0.09	73.15±0.43	0.14±0.03	0.059±0.016	93.40±0.52	26	1.33±0.03	X	7.53±3.21
MH610	G6+M	$DyPO_4$	30	2.5	4.04±0.34	3.84±0.17	13.32±0.27	73.66±0.40	0.12±0.01	0.043±0.023	95.10±0.69	26	1.25±0.08	X	3.42±2.50
MH611	G6+M	$HoPO_4$	30	2.5	3.76±0.07	3.99±0.03	12.99±0.06	73.88±0.35	0.11±0.02	0.052±0.020	94.46±0.41	20	1.24±0.01	X	4.23±2.00
MH612	G16+M	$ErPO_4$	31	2.5	3.70±0.07	3.64±0.04	12.74±0.16	74.19±0.25	0.11±0.01	0.081±0.014	94.52±0.39	25	1.28±0.02	X	6.29±1.06
MH613	G6+M	$TmPO_4$	38	2.5	3.49±0.15	3.61±0.09	13.09±0.18	76.91±0.86	0.11±0.02	0.099±0.024	97.40±1.02	26	1.36±0.04	X	7.70±2.17
MH614	G6+M	$YbPO_4$	31	2.5	3.64±0.23	3.75±0.05	12.39±0.05	73.82±0.12	0.11±0.03	0.122±0.022	93.85±0.25	26	1.24±0.05	X	9.96±3.50
MH615	G6+M	$LuPO_4$	31	2	3.59±0.15	3.59±0.10	12.45±0.13	74.77±1.68	0.12±0.01	0.088±0.030	94.67±1.81	25	1.28±0.06	X	7.20±2.21

[a] *Starting materials: 90% water-saturated haplogranite glass (ASI =0.7-1.2), i.e. containing about 6% H_2O + 10% pure individual rare earth phosphate crystals (monazite (M) or xenotime (X)).*

[b] *The pressure during the run (2kbar) was increased to this pressure just immediately before the quench to avoid bubble nucleation*

[c] *Aluminum saturation index (ASI) = Al /(Na+K) in mol*

[d] *Phase present other than glass: M = monazite, X = xenotime, Mi = mica, Q = quartz and Fk = alkali feldspar*

[e] *Solubility product (Ksp) for reaction* $REEPO_4^{melt} \Leftrightarrow REE^{melt} + PO_4^{melt}$

Table 3.6. Experimental data on the solubility of rare earth phosphates (monazite and xenotime) in haplogranitic melts with an alkali saturation index (ASI) of 1.1 at 800°C and 2 kbar as derived from average microprobe analyses of quenched glasses from experiments with two months duration. The pressure during the run was increased to 2.5 kbar just immediately before the quench to avoid bubble nucleation.

No.	Starting material[a]		Na_2O	K_2O	Al_2O_3	SiO_2	P_2O_5	REE_2O_3	Total	n	ASI[b]	Phases[c]	(Ksp)[d]
	Mix	Formula	(%)	(%)	(%)	(%)	(%)	(%)	(%)				(10^{-5} mol^2/kg^2)
T8201	MH401	$LaPO_4$	3.97±0.12	4.40±0.03	12.05±0.06	74.13±0.09	0.24±0.09	0.025±0.018	94.85±0.36	23	1.08±0.02	M, Mi	5.38±4.44
T8202	MH402	$CePO_4$	3.86±0.25	4.06±0.04	11.69±0.05	74.78±0.37	0.11±0.02	0.041±0.011	93.38±0.50	25	1.10±0.04	M	3.94±1.29
T8203	MH403	$PrPO_4$	4.11±0.15	3.91±0.04	11.99±0.14	72.90±0.38	0.10±0.03	0.029±0.013	93.22±0.28	20	1.10±0.03	M	2.35±1.19
T8204	MH404	$NdPO_4$	3.90±0.12	3.97±0.03	12.17±0.05	73.01±0.31	0.12±0.02	0.033±0.014	93.34±0.39	22	1.15±0.02	M	3.34±1.58
T8206	MH406	$SmPO_4$	4.00±0.62	4.34±0.13	12.35±0.15	72.16±1.44	0.09±0.03	0.044±0.009	93.01±2.30	14	1.11±0.13	M,Mi	3.36±1.59
T8207	MH407	$EuPO_4$	3.83±0.10	3.77±0.07	12.01±0.09	74.17±0.61	0.11±0.02	0.055±0.004	94.08±0.75	22	1.17±0.02	M	4.90±1.14
T8208	MH408	$GdPO_4$	3.68±0.21	3.86±0.09	12.05±0.07	75.18±0.74	0.12±0.02	0.062±0.017	95.10±1.01	23	1.19±0.05	M/X	5.87±2.05
T8209	MH409	$TbPO_4$	3.92±0.13	3.99±0.11	11.85±0.28	75.00±1.63	0.15±0.06	0.050±0.014	95.08±2.08	25	1.11±0.02	X	5.74±2.83
T8210	MH410	$DyPO_4$	3.52±0.27	4.08±0.19	11.66±0.44	74.67±3.63	0.12±0.02	0.062±0.004	94.09±4.40	22	1.14±0.03	X	5.44±1.08
T8211	MH411	$HoPO_4$	3.83±0.19	4.08±0.10	11.21±0.41	74.86±2.20	0.11±0.02	0.051±0.015	94.28±2.83	23	1.05±0.03	X	4.11±1.23
T8212	MH412	$ErPO_4$	3.99±0.12	3.46±0.09	12.27±0.32	74.51±1.65	0.11±0.02	0.084±0.033	94.63±2.16	19	1.20±0.02	X	6.19±0.51
T8213	MH413	$TmPO_4$	3.67±0.32	4.01±0.14	11.40±0.50	73.31±2.51	0.12±0.02	0.086±0.023	92.77±3.25	20	1.10±0.04	X	7.36±2.28
T8214	MH414	$YbPO_4$	4.20±0.07	4.08±0.05	12.24±0.11	73.22±0.56	0.11±0.02	0.129±0.020	94.11±0.70	21	1.09±0.02	X	10.27±2.88
T8215	MH415	$LuPO_4$	3.85±0.09	3.93±0.09	11.60±0.22	73.71±1.12	0.12±0.02	0.093±0.021	93.45±1.45	22	1.10±0.02	X	7.74±2.24

[a] *Starting materials: 90% water-saturated haplogranite glass (ASI =1), i.e. containing about 6% H_2O + 10% pure individual rare earth phosphate crystals (monazite (M) or xenotime (X)).*

[b] *Aluminum saturation index (ASI) = Al /(Na+K) in mol*

[c] *Phase present other than glass: M = monazite, X = xenotime, Mi = mica, Q = quartz and Fk = alkali feldspar*

[d] *Solubility product (Ksp) for reaction* $REEPO_4^{melt} \Leftrightarrow REE^{melt} + PO_4^{melt}$

Table 3.7. Experimental data on the solubility of rare earth phosphates (monazite and xenotime) in haplogranitic melts with an alkali saturation index (ASI) of 1.2 at 1100°C and 2 kbar as derived from average microprobe analyses of quenched glasses. Run duration was 7 days.

No.	Starting material[a]		Na_2O	K_2O	Al_2O_3	SiO_2	P_2O_5	REE_2O_3	Total	n	ASI[b]	Phases[c]	(Ksp)[d]
	Mix	Formula	(%)	(%)	(%)	(%)	(%)	(%)	(%)				(10^{-5} mol^2/kg^2)
T1101	G24+M	$LaPO_4$	4.07±0.29	3.45±0.04	12.28±0.11	74.41±0.21	0.17±0.01	0.117±0.010	94.52±0.47	22	1.18±0.05	M	17.16±1.98
T1102	G24+M	$CePO_4$	4.07±0.43	3.43±0.03	12.37±0.07	74.64±0.16	0.18±0.02	0.168±0.014	94.89±0.44	9	1.21±0.11	M	24.94±3.34
T1103	G24+M	$PrPO_4$	4.11±0.11	3.45±0.04	12.12±0.12	74.27±0.34	0.14±0.03	0.203±0.031	94.34±0.51	19	1.16±0.02	M	25.86±2.61
T1104	G24+M	$NdPO_4$	4.23±0.09	3.41±0.04	12.38±0.08	74.25±0.22	0.18±0.02	0.158±0.011	94.62±0.28	26	1.17±0.02	M	23.43±3.12
T1106	G24+M	$SmPO_4$	4.10±0.10	3.36±0.09	12.36±0.10	73.78±0.37	0.19±0.02	0.212±0.012	94.03±0.54	26	1.20±0.02	M	31.84±4.25
T1107	G24+M	$EuPO_4$	4.24±0.09	3.41±0.02	12.45±0.07	73.95±0.35	0.22±0.02	0.254±0.020	94.54±0.36	26	1.18±0.02	M	43.95±5.75
T1108	G24+M/X	$GdPO_4$	4.13±0.12	3.37±0.09	12.12±0.12	74.21±0.35	0.21±0.02	0.253±0.018	94.33±0.60	23	1.17±0.03	M/X	40.62±4.62
T1109	G24+X	$TbPO_4$	4.05±0.11	3.38±0.05	12.22±0.10	74.07±0.25	0.25±0.03	0.239±0.022	94.25±0.35	22	1.19±0.02	X	46.17±6.09
T1110	G24+X	$DyPO_4$	4.13±0.09	3.39±0.03	12.30±0.05	74.11±0.21	0.21±0.02	0.315±0.024	94.48±0.29	16	1.18±0.02	X	49.14±5.07
T1111	G24+X	$HoPO_4$	4.16±0.12	3.45±0.03	12.37±0.06	74.49±0.22	0.19±0.02	0.269±0.040	94.96±0.35	18	1.18±0.02	X	38.22±7.49
T1112	G24+X	$ErPO_4$	4.12±0.08	3.45±0.03	12.23±0.09	73.62±0.62	0.19±0.02	0.272±0.028	93.91±0.75	18	1.17±0.01	X	39.06±6.01
T1113	G24+X	$TmPO_4$	4.08±0.09	3.44±0.02	12.41±0.04	74.43±0.28	0.20±0.03	0.284±0.050	94.86±0.32	17	1.20±0.02	X	41.37±11.2
T1114	G24+X	$YbPO_4$	4.00±0.06	3.40±0.05	12.30±0.02	74.56±0.08	0.21±0.01	0.369±0.022	94.86±0.14	19	1.21±0.02	X	55.99±5.87
T1115	G24+X	$LuPO_4$	4.07±0.09	3.38±0.04	12.28±0.08	74.22±0.71	0.20±0.02	0.328±0.035	94.56±0.71	14	1.19±0.02	X	45.41±6.51

[a] *Starting materials: 90% water- saturated haplogranite glass (ASI =1), i.e. containing about 6% H_2O + 10% pure individual rare earth phosphate crystals*

[b] *Aluminum saturation index (ASI) = Al /(Na+K) in mol*

[c] *Phase present other than glass: M = monazite, X = xenotime*

[d] *Solubility product (Ksp) for reaction* $REEPO_4^{melt} \Leftrightarrow REE^{melt} + PO_4^{melt}$

Table 3.8. Experimental data on the solubility of rare earth phosphates (monazite and xenotime) in haplogranitic melts with an alkali saturation index (ASI) of 1.2 at 800°C and 2 kbar as derived from average microprobe analyses of quenched glasses from 2 months reversed experiments. The pressure during the run was increased to 2.5 kbar just immediately before the quench to avoid bubble nucleation

No.	Starting material[a]		Na_2O	K_2O	Al_2O_3	SiO_2	P_2O_5	REE_2O_3	Total	n	ASI[b]	Phases[c]	(Ksp)[c]
	Mix	*Formula*	*(%)*	*(%)*	*(%)*	*(%)*	*(%)*	*(%)*	*(%)*				*(10^{-5} mol^2/kg^2)*
R8201	T1101	$LaPO_4$	3.91±0.18	3.39±0.11	12.47±0.10	75.25±0.46	0.13±0.04	0.046±0.026	95.25±0.76	26	1.23±0.02	M	5.18±3.53
R8202	T1102	$CePO_4$	4.15±0.31	3.39±0.06	12.37±0.05	74.86±0.20	0.15±0.03	0.062±0.012	93.86±0.34	15	1.19±0.06	M	7.08±2.06
R8203	T1103	$PrPO_4$	3.96±0.21	3.41±0.12	12.31±0.15	74.16±0.52	0.12±0.03	0.073±0.018	93.81±0.87	25	1.21±0.06	M	7.21±3.01
R8204	T1104	$NdPO_4$	4.11±0.06	3.43±0.06	12.37±0.07	74.09±0.23	0.14±0.02	0.055±0.013	94.23±0.30	26	1.19±0.01	M	6.31±1.41
R8206	T1106	$SmPO_4$	3.89±0.15	3.37±0.17	11.99±0.47	72.78±1.99	0.14±0.02	0.079±0.014	91.81±2.27	26	1.19±0.05	M	9.01±2.03
R8207	T1107	$EuPO_4$	4.06±0.09	3.42±0.08	12.28±0.11	73.89±0.24	0.16±0.03	0.080±0.033	93.93±0.34	25	1.19±0.02	M	8.46±3.15
R8208	T1108	$GdPO_4$	3.86±0.20	3.37±0.10	12.45±0.25	75.12±0.85	0.17±0.09	0.103±0.028	95.15±0.99	25	1.25±0.03	M/X	10.66±5.80
R8209	T1109	$TbPO_4$	3.81±0.15	3.47±0.02	12.33±0.04	74.63±0.11	0.24±0.04	0.104±0.041	94.67±0.21	23	1.24±0.03	X	18.11±9.16
R8210	T1110	$DyPO_4$	3.77±0.15	3.49±0.09	12.43±0.19	75.15±0.84	0.18±0.09	0.091±0.023	95.27±1.02	25	1.26±0.04	X	9.83±3.97
R8211	T1111	$HoPO_4$	4.12±0.10	3.43±0.02	12.36±0.08	74.37±0.26	0.15±0.03	0.119±0.025	94.59±0.36	25	1.18±0.01	X	13.37±4.09
R8212	T1112	$ErPO_4$	4.05±0.11	3.43±0.04	12.29±0.10	74.18±0.40	0.17±0.02	0.124±0.037	94.28±0.50	25	1.19±0.02	X	15.77±5.87
R8213	T1113	$TmPO_4$	3.73±0.15	3.77±0.07	12.50±0.06	73.50±0.20	0.11±0.02	0.103±0.017	93.74±0.32	20	1.23±0.03	X	8.15±1.59
R8214	T1114	$YbPO_4$	3.69±1.12	3.42±0.06	12.43±0.09	74.56±0.61	0.19±0.02	0.243±0.049	94.56±0.69	10	1.37±0.50	X	33.00±9.03
R8215	T1115	$LuPO_4$	3.60±0.51	3.40±0.01	11.92±0.05	72.65±0.25	0.20±0.03	0.218±0.056	92.13±0.36	26	1.27±0.16	X	30.27±9.49

[a] *Starting materials: 90% water-saturated haplogranite glass (ASI =1), i.e. containing about 6% H_2O + 10% pure individual rare earth phosphate crystals.*

[b] *Aluminum saturation index (ASI) = Al /(Na+K) in mol*

[c] *Phase present other than glass: M = monazite, X = xenotime.*

[d] *Solubility product (Ksp) for reaction* $REEPO_4^{melt} \Leftrightarrow REE^{melt} + PO_4^{melt}$

Table 3.9. Experimental data on the solubility of rare earth phosphates (monazite and xenotime) in haplogranitic melts with variable alkali saturation index (ASI) at 800°C and 2 kbar as derived from the extrapolation of measured diffusion profiles (Co).

Run No.	Run	ASI	Aver. REE	Co (REE)	Diffusivities	Ksp*
	duration		*(ppm)*	*(ppm)*	*(10^{-11} cm^2/s)*	*(10^{-5} mol^2/kg^2)*
MH101	24	0.73±0.01	212±45	267±17	3±1	9.35±0.02
MH102	30	0.74±0.01	877±92	978±25	129±98	15.52±0.04
MH103	31	0.74±0.01	1177±154	1212±69	705±272	18.20±0.12
MH104	28	0.83±0.03	3356±325	3582±151	216±327	38.13±0.27
MH106	30	0.76±0.01	2137±125	2385±121	78±87	45.59±0.23
MH107	29	0.73±0.01	2905±103	3225±111	92±74	76.70±0.16
MH108	33	0.74±0.01	5448±233	5665±90	852±819	119.08±0.14
MH109	31	0.82±0.03	2457±108	3016±238	21±21	71.59±0.41
MH110	30	0.73±0.01	4768±63	5925±345	21±13	173.25±0.76
MH111	30	0.73±0.01	5816±299	6077±105	464±310	184.29±0.18
MH112	23	0.81±0.03	4055±878	5270±600	15±14	130.23±3.25
MH113	30	0.75±0.02	6650±547	7223±209	64±36	227.14±0.50
MH114	35	0.73±0.02	8144±385	8389±216	1086±198	251.52±0.42
MH115	31	0.75±0.01	7469±251	8015±204	246±211	282.11±0.57
MH201	30	0.88±0.03	158±76	414±50	0.9±0.2	15.45±0.18
MH202	31	0.87±0.01	366±69	589±70	5.8±3.5	7.17±0.09
MH203	31	0.87±0.01	255±65	410±54	10.6±8.0	5.28±0.13
MH204	31	0.89±0.01	493±190	598±86	19.9±23	7.19±0.14
MH206	31	0.98±0.01	563±191	788±93	2.9±1.4	10.79±0.10
MH207	30	0.85±0.01	1184±235	1506±263	11.0±14	20.93±0.46
MH208	32	0.95±0.05	1367±83	1496±48	122.3±92	21.70±0.09
MH209	31	0.86±0.02	1211±126	1327±55	88.9±71	22.84±0.10
MH210	30	0.78±0.03	1847±277	2027±139	47.3±41	31.19±0.27
MH211	31	0.88±0.01	2018±196	2219±79	142.7±122	34.38±0.12
MH212	26	0.88±0.06	2274±888	2416±390	72.3±179	45.25±2.33
MH213	27	0.88±0.01	2063±93	2211±62	218.5±226	35.20±0.07
MH214	30	0.89±0.02	3137±509	3469±203	52.5±40.9	54.02±0.35
MH215	29	0.88±0.02	2981±243	3366±134	107.3±83.8	58.72±0.26
MH301	31	0.99±0.02	136±64	301±44	1.6±0.7	11.58±0.42
MH302	30	1.00±0.05	331±104	447±53	8.0±5.8	4.44±0.09
MH303	31	0.98±0.01	183±110	479±136	3.6±3.4	6.47±0.61
MH304	31	0.98±0.01	231±100	472±90	9.8±6.3	5.35±0.19
MH306	31	0.98±0.01	406±53	680±72	4.6±2.2	6.76±0.10
MH307	30	0.99±0.01	345±77	611±75	1.0±0.3	7.09±0.15
MH308	32	0.99±0.02	390±124	496±51	28.4±28.5	5.43±0.09
MH309	30	0.97±0.02	361±42	664±58	6.3±2.8	6.42±0.05
MH310	30	0.99±0.01	638±95	1019±91	16.3±9.6	10.22±0.13
MH311	30	0.99±0.01	463±113	610±48	15.1±8.7	5.94±0.07
MH312	30	1.00±0.02	869±195	1190±196	5.0±4.1	12.83±0.44
MH313	34	1.03±0.04	856±196	1092±55	16.0±6.7	11.28±0.12
MH314	30	0.99±0.02	1826±310	1977±114	78.1±80.1	18.83±0.14
MH315	29	0.93±0.02	1259±212	1704±77	14.2±4.5	16.98±0.13
MH401	31	1.14±0.04	207±95	322±57	5.33±4.21	7.35±0.43
MH402	38	1.09±0.01	311±178	575±116	7.23±7.30	6.94±0.30
MH403	30	1.14±0.01	238±126	423±55	4.55±2.21	4.69±0.11
MH404	31	1.11±0.01	214±110	426±70	2.56±1.35	4.70±0.10
MH406	30	1.09±0.02	511±77	714±70	10.04±7.03	7.69±0.09
MH407	30	1.21±0.04	405±133	640±73	2.37±0.95	6.97±0.12
MH408	30	1.05±0.02	496±134	803±186	3.75±3.78	8.44±0.25
MH409	30	1.09±0.01	392±125	840±116	1.19±0.41	9.03±0.24
MH410	30	1.06±0.02	462±142	775±114	2.96±1.42	7.90±0.10
MH411	31	1.11±0.01	390±130	695±126	3.55±2.35	6.43±0.23
MH412	30	1.09±0.02	523±197	925±186	4.79±4.90	8.35±0.30
MH413	30	1.16±0.05	748±96	1135±82	10.16±4.01	9.81±0.11
MH414	30	1.15±0.03	1219±171	1592±128	14.73±11.5	12.61±0.21
MH415	31	1.06±0.01	1030±221	1478±123	15.31±11.0	13.05±0.15

Table 3.9 *(continued)*

Run No.	Run duration	ASI[a]	Aver. REE *(ppm)*	Co (REE) *(ppm)*	Diffusivities *(10^{-11} cm^2/s)*	Ksp[b] *(10^{-5} mol^2/kg^2)*
MH501	30	1.17±0.01	156±75	311±72	2.12±1.56	8.20±1.18
MH502	31	1.15±0.00	320±128	413±81	1.87±1.23	4.18±0.10
MH503	31	1.19±0.02	197±74	332±67	4.71±3.44	4.32±0.17
MH504	31	1.13±0.02	226±94	339±50	9.04±6.16	3.52±0.07
MH506	30	1.14±0.01	528±94	588±59	17.64±18.7	5.87±0.11
MH507	33	1.10±0.01	291±131	384±67	1.60±0.85	4.80±0.19
MH508	30	1.13±0.04	274±127	392±95	10.84±15.5	4.09±0.11
MH509	30	1.18±0.01	496±167	688±67	5.98±2.86	7.30±0.19
MH510	30	1.19±0.02	391±201	669±68	9.90±5.54	6.40±0.10
MH511	30	1.16±0.04	227±93	407±45	5.15±2.37	3.90±0.06
MH512	27	1.15±0.02	570±166	731±91	3.29±1.64	6.42±0.12
MH513	31	1.22±0.02	743±234	1142±129	7.52±3.82	10.59±0.16
MH514	29	1.18±0.02	1263±186	1602±129	32.50±29.4	14.05±0.30
MH515	31	1.21±0.03	790±431	1208±159	3.47±1.61	10.72±0.26
MH601	30	1.28±0.02	178±80	404±63	2.12±1.56	8.79±0.51
MH602	31	1.24±0.01	402±75	514±42	11.25±7.22	5.53±0.06
MH603	30	1.30±0.07	266±137	421±67	7.02±7.54	5.39±0.12
MH604	30	1.32±0.02	290±111	388±56	9.10±8.48	4.28±0.07
MH606	30	1.30±0.03	590±92	639±66	92.73±208	7.20±0.13
MH607	33	1.29±0.03	421±153	688±54	2.36±0.61	7.31±0.09
MH608	30	1.28±0.02	602±123	842±62	5.65±2.34	9.33±0.06
MH609	30	1.33±0.03	504±162	721±77	22.06±26	10.69±0.29
MH610	30	1.25±0.08	325±226	677±104	3.73±1.93	7.03±0.12
MH611	30	1.24±0.01	454±179	764±112	8.09±6.26	7.02±0.18
MH612	31	1.28±0.02	708±119	896±42	17.84±6.05	8.00±0.03
MH613	38	1.36±0.04	891±207	1111±97	43.52±35.3	9.57±0.12
MH614	31	1.24±0.05	1073±192	1482±57	7.18±1.51	13.65±0.15
MH615	31	1.28±0.06	774±263	1024±102	9.96±6.26	9.63±0.12
T8201	62	1.08±0.02	214±156	411±71	0.72±0.29	9.64±0.71
T8202	61	1.10±0.04	346±96	495±42	4.02±1.71	5.64±0.08
T8203	62	1.10±0.03	244±109	380±54	2.33±1.06	3.77±0.17
T8204	64	1.15±0.02	287±116	450±49	3.60±1.69	5.18±0.09
T8206	62	1.11±0.13	377±76	686±52	2.79±0.75	5.91±0.14
T8207	62	1.17±0.02	475±36	575±39	30.04±26.1	5.92±0.09
T8208	64	1.19±0.05	535±146	587±62	25.58±35.9	6.40±0.13
T8209	62	1.11±0.02	436±122	691±77	8.68±6.50	8.92±0.38
T8210	61	1.14±0.03	539±38	741±64	19.00±12.9	7.45±0.11
T8211	62	1.05±0.03	442±128	792±65	2.98±0.89	7.41±0.10
T8212	64	1.20±0.02	641±67	1045±123	5.02±2.88	9.53±0.15
T8213	62	1.10±0.04	750±204	1055±88	10.26±6.29	10.39±0.12
T8214	61	1.09±0.02	1135±173	1731±133	3.84±1.31	15.96±0.24
T8215	64	1.10±0.02	815±184	1216±199	7.09±6.24	11.46±0.27

[a] *Aluminum saturation index (ASI) = Al /(Na+K) in mol of run product glasses calculated from microprobe data*

[b] *Solubility product (Ksp) for reaction* $REEPO_4^{melt} \Leftrightarrow REE^{melt} + PO_4^{melt}$

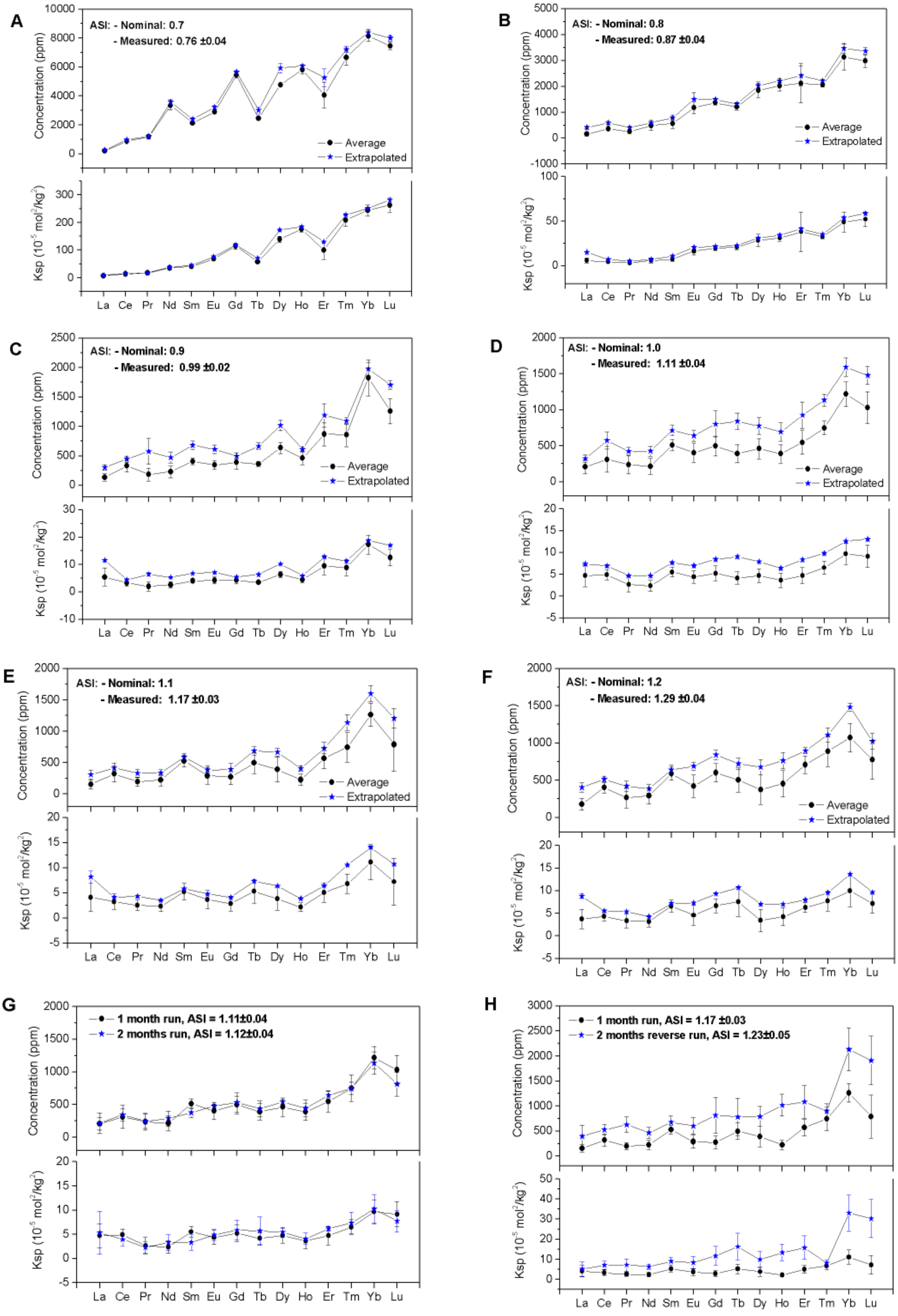

Figure 3.7. Graph showing the solubility of REE phosphates in haplogranite melt with 6 wt.% H_2O from EPMA analyses of the run products at 800°C and 2 kbar. Error bars indicate standard deviations of replicated measurement. Shown are both average microprobe data of the glasses analysed and rare earth concentrations obtained by extrapolating diffusion profiles measured around a crystal to the crystal/melt interface. In subfigures G and H, average data are shown only.

Attainment of equilibrium was checked by runs with different starting materials and by approaching equilibrium from both dissolution and crystallization experiments. The measured solubility of $LaPO_4$ and $CePO_4$ in water-saturated haplogranite melt at 1100°C is similar to the result given by Rapp and Watson (1986), demonstrating attainment of equilibrium at 1100°C within 1 week. However, at 800°C and 2 kbar, attainment of equilibrium is extremely sluggish for the metaluminous and peraluminous compositions and even run duration of 1 – 2 months fail to give identical results if equilibrium is approached from different directions. For the experiments with ASI = 1.1, it is evident that at 800°C and 2 kbar, the concentrations of REE are almost constant after about 1–2 months, and slightly lower than the concentrations observed in the reverse runs, demonstrating that the dissolution of REE is very slow and these runs did not fully reach equilibrium. For that reason, the saturation concentration of the REE in the melts was also estimated by extrapolating diffusion profiles. Extrapolated results for all run products from dissolution experiments are summarized in Table 3.9.

Monazite and xenotime solubilities derived from average microprobe analyses and from the extrapolation of diffusion profiles are plotted in Figure 3.7. In the peralkaline melts average and extrapolated solubilities are nearly identical, implying attainment of equilibrium in these low-viscosity melts. On the other hand, the experiments with metaluminous and peraluminous composition probably did not fully reach equilibrium.

The solubility of REE in each melt composition is shown in Figure 3.7. These graphs demonstrate that the solubility of REE is controlled by the ionic radius and type of REE mineral. The solubility increases with decreasing ionic radius. The solubility of La (1.16 Å), the largest REE, is around 200-400 ppm in all melt compositions (ASI = 0.7-1.2) at 800°C and 2 kbar, while the solubility of the smallest one, Lu (0.977Å) at the same condition, is up to 7000 – 8000 ppm in peralkaline melt. The solubility of monazite in these melts is less compared to that of xenotime at the same condition. This observation is in agreement with the previous experiments (Keppler, 1993; Wolf and London, 1995), who showed that the solubility of xenotime is always greater than that of monazite at the same temperature, pressure and composition. Thus, fractionation of monazite or xenotime leads to REE depletion in the melt.

Inspection of Figure 3.7 shows that monazite and xenotime solubility is not a continuous function of ionic radius or atomic number. This is most obvious for the strongly peralkaline melts where equilibrium was clearly reached. These samples showed virtually no concentration gradients attributable to diffusion, as evident from the close agreement between average and extrapolated REE concentration (Figure 3.1, part A). Also, due to the high bulk solubilities, the analytical uncertainties in these experiments are quite low. The monazite and xenotime solubility shows four maxima at Nd, Gd, Dy/Ho and Yb, i.e. the REE abundance in the melt shows a pronounced “lanthanide tetrad effect”. The fractionation between neighbouring REE often exceeds a factor of 2 and is therefore far outside any analytical error. Towards the less peralkaline , metaluminous and peraluminous compositions, the tetrad effect becomes less clear, which may reflect incomplete attainment of equilibrium, larger analytical uncertainties due to the much lower REE concentrations, or a real reduction of element fractionation. However, some features are seen in virtually all compositions, in particular the increased solubility of Yb compared to Tm and Lu is always visible. A smaller peak near Dy is seen in all except the most peraluminous composition

The composition dependence of REE phosphate solubility was studied for ASI = 0.7 to 1.2 at 800°C and 2 kbar. The data presented in Table 3.5 show that the solubility of the REE phosphates in water-saturated haplogranitic melts decreases rather strongly with increasing ASI. The solubility of REE shows a considerable change in magnitude and ranges from about $1\text{x}10^{-3}$ mol/kg (Pr in peraluminous melt) to more than $40\text{x}10^{-3}$ mol/kg (Yb, Lu in very strong peralkaline melt). Overall, the solubility of REE shows a systematic variation with the melt composition. In some cases, the solubility data are rather scattered, which may result from analytical and experimental problems (see above). The concentration of La in melts is generally very low and shows little dependence on ASI. The solubility of all other REE decreases strongly with increasing ASI of the melt. This decrease of REE solubility with increasing ASI is more pronounced for the HREE than for the LREE. At 800°C and 2 kbar the increase of ASI by about 0.1 leads to a 2 – 5 folds decrease in LREE solubility, whereas the solubility of HREE decreases almost 10 folds. However, this decrease is observed only in the peralkaline to sub-metaluminous range, whereas in peraluminous melt composition the solubility of REE is almost constant. In some cases, the solubility may very slightly increase in the peraluminous range, but the effect is within analytical error.

The most important effect of melt composition on the solubility of monazite and xenotime occurs in the peralkaline range, where the amount of dissolved of REE decreases with increasing ASI (Figure 3.8). In contrast, ASI shows a little effect on the solubility of REE in peraluminous melt. This observation is in agreement with previous experiments (Keppler, 1993; Montel et al., 1993; Rapp and Watson, 1986), suggesting that the treatment of the REE solubility data should be divided into two separated subsets. The logarithm of REE solubility in water-saturated haplogranitic melts decreases linearly with ASI in peralkaline melt composition. The data can be fitted to a linear equation:

$$Y = A + Bx \qquad \text{(Eq. 3.8)}$$

where Y is the log(REE solubility) in ppm and (x) is the ASI. The fitting results using extrapolated data and also including data published by Montel (1986) and Keppler (1993) are summarized in Table 3.10, and the error quoted is one standard deviation.

Table 3.10. Fit parameters for the linear curves describing the dependence of the logarithm of rare earth solubility on aluminium saturation index for peralkaline to metaluminous melts (ASI<1) according to Eq.3.8

Y	A	B	Y	A	B
La	3.43(0.46)	-0.93(0.48)	Tb	5.65(0.06)	-2.86(0.07)
Ce	4.94(0.26)	-2.42(0.33)	Dy	6.28(0.30)	-3.33(0.34)
Pr	4.40(0.25)	- 1.76(0.28)	Ho	7.10(0.37)	-4.33(0.42)
Nd	6.39(1.37)	-3.87(1.55)	Er	5.86(0.01)	-2.81(0.01)
Sm	5.07(0.35)	-2.38(0.42)	Tm	6.55(0.38)	-3.58(0.43)
Eu	5.91(0.21)	-3.13(0.23)	Yb	5.99(0.25)	-2.74(0.28)
Gd	6.84(0.49)	-4.11(0.53)	Lu	6.12(0.11)	-2.93(0.13)

In general, the agreement of the few available data for pure REE phosphates with the data of the present study is quite good, in particular, if one considers that the initial phosphorus contents of the melts in these studies were different.

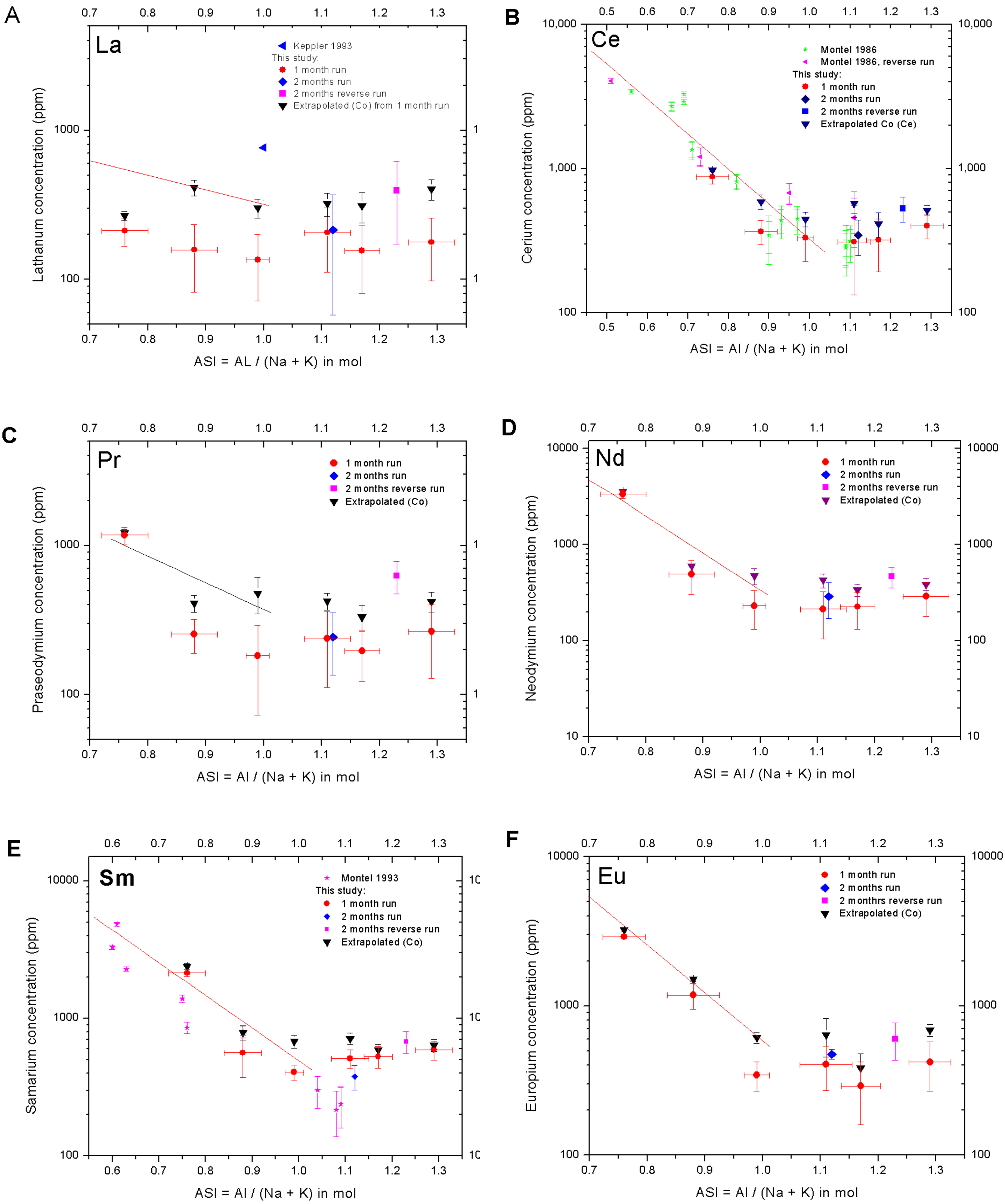

Figure 3.8. Effect of melt composition, represented by ASI as defined in text, on the solubility of REE phosphates in haplogranite melts. Error bars indicate ± 1σ error. The slopes of the linear fitting curves, in the alkaline to sub-metaluminous range (ASI<1), shows the relationship between melt composition and the REE solubility in ppm at 800^{o}C and 2 kbar. Data used for fitting is mainly from this study, except the elements Ce, Sm and Yb, which were coupled with data from Montel (1986) and Keppler (1993). The REE solubility increases with decreasing ASI of the melt quite drastically in the peralkaline range, while it is constant in peraluminous melt.

Figure 3.8 (continued)

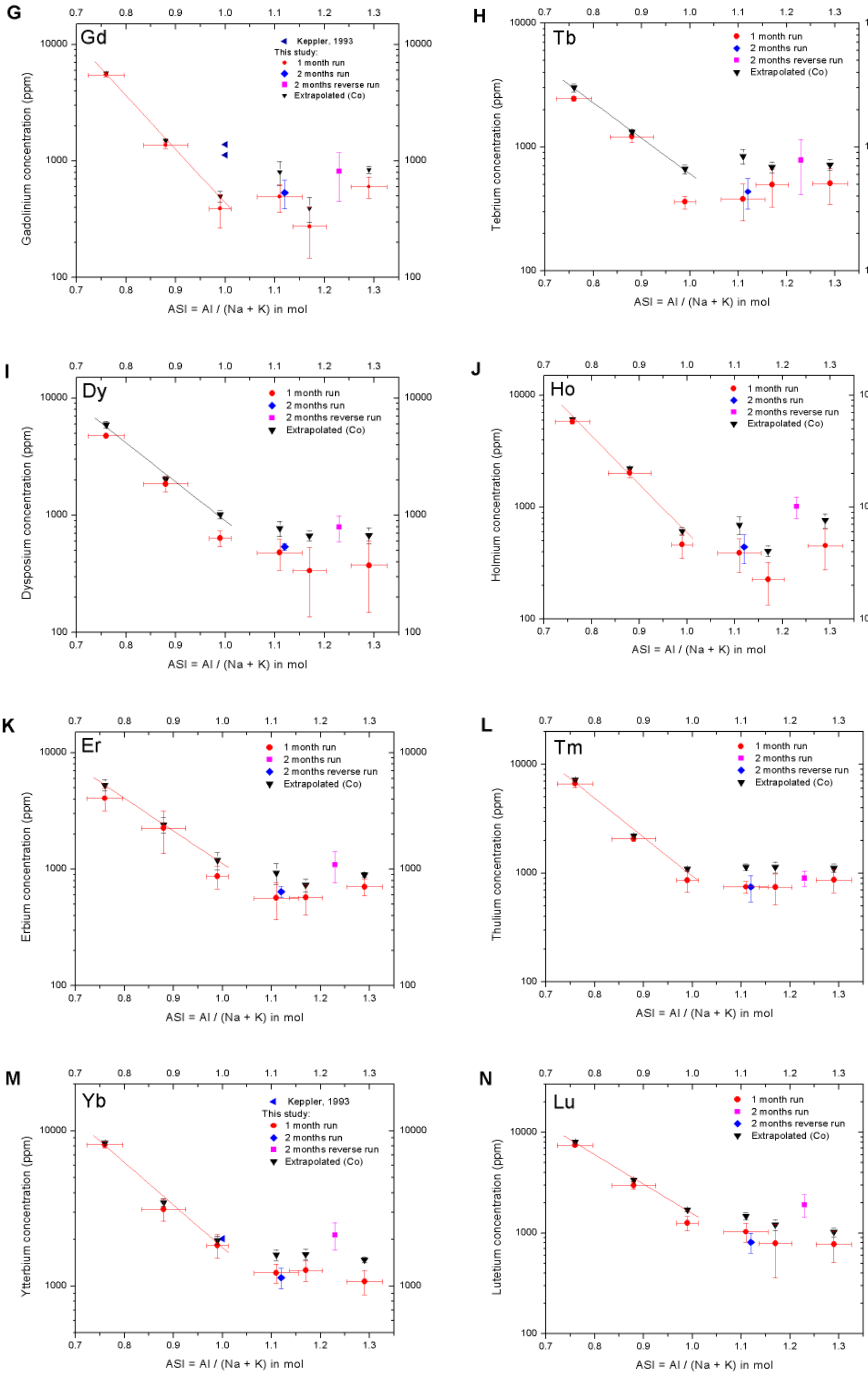

3.3. *The effect of fluorine on REE solubility in haplogranitic melts*

Two series of solubility experiments doped with 2 and 4 wt.% of fluorine were conducted and the results are given in Table 3.11. The extrapolated results from fitting diffusion profiles are summarized in Table 3.12. Mica was observed in sample 2F8. The solubility of REE, however, was not affected by this phase, because the composition of the melt was not significantly changed.

At 800°C and 2 kbar, the solubility of REE in these melts, as expected, increases with decreasing ionic radius (Figure 3.9). The trend of solubility is almost the same as for runs without F. The uncertainty of the analytical results is relatively high (± 100 ppm), especially for the LREE, due to their low solubility in range of 200-400 ppm. Figure 3.9 shows that the REE solubility in F-bearing granitic melt as derived from the extrapolation of measured diffusion profiles is only about 100-200 ppm higher than the average microprobe analyses, implying that these experimental data are close to the equilibrium. Their solubility, however, is a little bit lower than in the melt without F. This is possibly related to the enhancement of diffusion rates by fluorine. The data show a very week fluorine dependence of the REE solubility in granitic melts. Keppler (1993) already concluded that fluorine has virtually no effect on monazite and xenotime solubility. The data from Keppler (1993), however, show more scatter and they are generally higher than those of the present study.

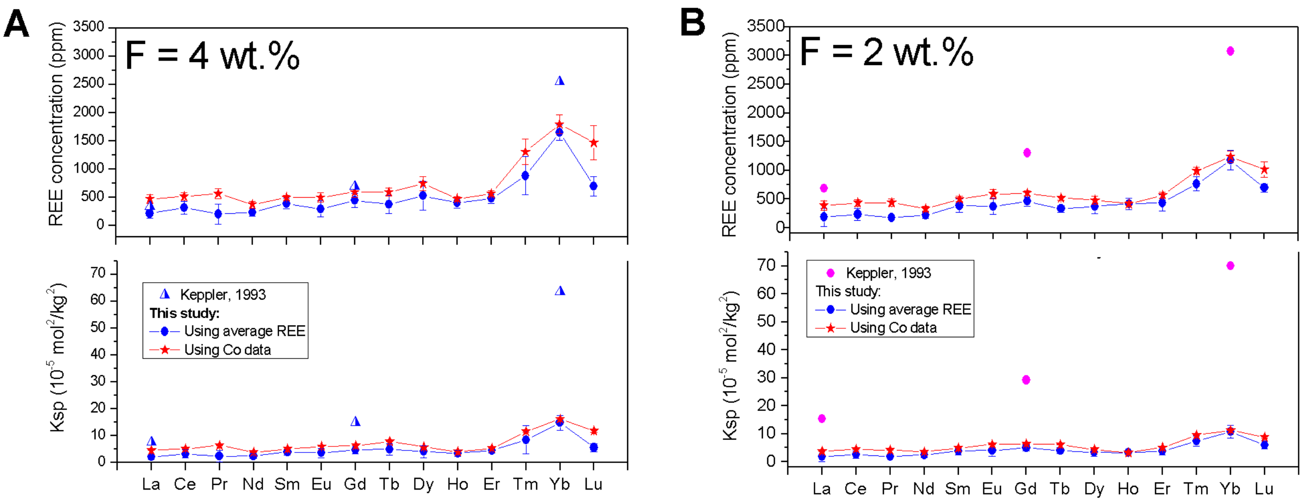

Figure 3.9. Monazite and xenotime solubility in hydrous haplogranitic melt doped with 2 and 4 wt.% at 800°C and 2 kbar

Figure 3.10 directly compares the solubility of individual REE phosphates with and without fluorine. In general, the results show a slight decrease of REE solubility with increasing F. The relationship between monazite or xenotime solubility and fluorine content can be described by a linear equation.

$$\mathbf{Y = A + Bx} \qquad \textbf{(Eq. 3.9)}$$

where: Y is the log Ksp (mol^2/kg^2) and X is the F concentration in wt.%. The fitting results are listed in Table 3.13 and illustrated in Figure 3.10

Table 3.11. . Experimental data on the solubility of rare earth phosphates (monazite and xenotime) in haplogranitic melts doped with 2 and 4 wt.% F at 800^{o}C and 2 kbar as derived from average microprobe analyses of quenched glasses from experiments of 30 -31 days duration. The pressure during the run was increased to 2.5 kbar just immediately before the quench to avoid bubble nucleation. The relative error limits were estimated from the standard deviation (1σ) based on replicate analysis (n).

No.	Starting material [a]		Na_2O	K_2O	Al_2O_3	SiO_2	P_2O_5	F	REE	Total	n	ASI[b]	Phases[c]	Ksp[d]
	Mix	Formula	(%)	(%)	(%)	(%)	(%)	(%)	(ppm)	(%)				(10^{-5} mol^2/kg^2)
2F1	AF2 + 10% M	LaPO4	4.62±0.17	4.65±0.07	12.59±0.10	69.45±0.71	0.09±0.02	1.84±0.02	187±159	93.28±0.80	42	1.00±0.03	M	1.87±1.96
2F2	AF2 + 10% M	CePO4	4.15±0.92	4.27±0.62	12.62±0.19	69.81±0.86	0.10±0.02	1.86±0.05	235±107	92.85±1.09	39	1.16±0.27	M	2.45±1.30
2F3	AF2 + 10% M	PrPO4	4.16±0.25	4.37±0.12	12.06±0.65	68.95±1.02	0.10±0.02	1.87±0.16	177±40	92.29±1.17	17	1.05±0.06	M	1.69±0.49
2F4	AF2 + 10% M	NdPO4	4.69±0.13	4.69±0.04	13.13±0.15	70.10±1.65	0.11±0.02	1.69±0.11	223±57	94.45±1.68	34	1.03±0.02	M	2.39±0.83
2F6	AF2 + 10% M	SmPO4	4.39±0.22	4.65±0.04	13.04±0.09	70.15±0.97	0.10±0.01	1.70±0.11	386±122	94.10±0.91	28	1.07±0.03	M	3.76±1.35
2F7	AF2 + 10% M	EuPO4	4.28±0.32	4.58±0.07	12.08±0.10	71.09±0.47	0.11±0.02	1.80±0.09	373±141	94.01±0.53	30	1.02±0.05	M	4.02±2.07
2F8	AF2 + 10% M-X	GdPO4	3.42±0.30	4.11±0.10	11.35±0.19	71.04±0.85	0.12±0.02	1.81±0.26	459±83	91.92±1.14	34	1.14±0.07	M/X, Mi	4.85±1.13
2F9	AF2 + 10% X	TbPO4	4.02±0.33	4.66±0.13	12.25±0.40	69.83±0.50	0.13±0.02	1.79±0.21	330±58	92.24±1.15	45	1.06±0.05	X	3.88±1.05
2F10	AF2 + 10% X	DyPO4	4.12±0.28	4.66±0.06	11.43±0.16	70.05±1.21	0.11±0.03	1.81±0.03	371±123	92.24±1.27	28	0.97±0.05	X	3.37±1.45
2F11	AF2 + 10% X	HoPO4	4.48±0.30	4.70±0.03	12.15±0.10	69.80±0.81	0.11±0.01	1.89±0.03	394±119	93.17±0.89	62	0.98±0.04	X	3.48±0.98
2F12	AF2 + 10% X	ErPO4	4.47±0.37	4.71±0.03	12.13±0.09	70.49±1.16	0.10±0.02	1.84±0.08	434±145	93.62±0.98	49	0.98±0.05	X	3.81±1.37
2F13	AF2 + 10% X	TmPO4	4.26±0.22	4.18±0.06	12.15±0.07	71.22±0.66	0.11±0.02	1.82±0.02	763±122	93.64±0.72	37	1.06±0.04	X	7.31±1.84
2F14	AF2 + 10% X	YbPO4	3.49±0.18	4.32±0.05	11.20±0.11	72.87±0.96	0.11±0.02	1.91±0.03	1178±172	94.07±1.12	29	1.08±0.03	X	10.70±2.40
2F15	AF2 + 10% X	LuPO4	4.37±0.16	4.67±0.02	12.19±0.04	70.74±0.72	0.11±0.02	1.81±0.02	692±75	93.98±0.83	15	1.00±0.02	X	5.98±1.45
4F1	AF4 + 10% M	LaPO4	3.94±0.13	4.53±0.18	12.07±0.22	68.03±1.20	0.10±0.02	3.91±0.05	218±78	92.62±1.35	31	1.07±0.02	M	2.09±0.83
4F2	AF4 + 10% M	CePO4	4.18±0.23	4.21±0.09	11.91±0.18	68.03±1.71	0.10±0.02	3.99±0.13	317±116	93.31±1.28	38	1.05±0.04	M	3.23±1.44
4F3	AF4 + 10% M	PrPO4	4.26±0.14	4.26±0.02	12.91±0.07	67.91±0.45	0.11±0.02	3.85±0.03	207±180	93.36±0.55	16	1.12±0.02	M	2.36±2.09
4F4	AF4 + 10% M	NdPO4	4.37±0.17	4.30±0.02	11.84±0.13	68.21±1.37	0.11±0.02	3.89±0.14	236±72	92.78±1.53	20	1.01±0.02	M	2.43±0.86
4F6	AF4 + 10% M	SmPO4	3.80±0.23	4.21±0.03	11.77±0.05	70.16±0.29	0.11±0.01	3.86±0.02	393±91	93.99±0.41	23	1.10±0.03	M	4.00±1.13
4F7	AF4 + 10% M	EuPO4	4.25±0.19	4.24±0.03	11.85±0.18	68.44±1.31	0.13±0.01	4.50±0.03	296±144	93.46±1.45	28	1.03±0.03	M	3.60±1.79
4F8	AF4 + 10% M-X	GdPO4	3.99±0.25	4.24±0.15	11.87±0.06	69.25±0.22	0.12±0.01	3.93±0.01	447±126	93.57±0.26	10	1.07±0.04	M/X	4.74±1.48
4F9	AF4 + 10% X	TbPO4	3.67±0.29	3.97±0.05	11.79±0.07	69.31±0.26	0.15±0.02	3.78±0.03	378±158	92.77±0.46	21	1.15±0.05	X	4.98±2.16
4F10	AF4 + 10% X	DyPO4	4.22±0.21	4.24±0.12	11.73±0.38	68.01±1.08	0.09±0.02	4.28±0.35	529±257	92.66±1.65	32	1.02±0.03	X	4.08±2.25
4F11	AF4 + 10% X	HoPO4	3.95±0.25	4.23±0.12	11.88±0.41	69.92±1.01	0.10±0.02	3.86±0.10	405±99	94.01±1.70	40	1.08±0.04	X	3.48±1.15
4F12	AF4 + 10% X	ErPO4	4.18±0.20	4.27±0.03	11.95±0.11	69.30±0.83	0.11±0.02	3.86±0.03	480±82	93.75±0.98	53	1.05±0.03	X	4.54±1.10
4F13	AF4 + 10% X	TmPO4	4.66±0.22	4.15±0.05	12.64±0.42	67.67±0.81	0.11±0.02	3.92±0.04	882±339	93.32±0.88	29	1.05±0.05	X	8.51±5.24
4F14	AF4 + 10% X	YbPO4	3.79±0.18	4.20±0.02	11.54±0.07	70.11±0.39	0.11±0.02	3.86±0.05	1649±137	93.81±0.45	14	1.08±0.03	X	14.89±2.77
4F15	AF4 + 10% X	LuPO4	4.48±0.41	4.16±0.13	12.40±0.42	67.71±0.86	0.10±0.02	4.24±1.38	699±173	93.18±1.75	30	1.05±0.04	X	5.55±1.57

[a] *Starting materials: 90% water-saturated haplogranitic glass, containing about 6% H_2O (all glasses contained 0.1% P_2O_5; glasses AF4 doped with 4 wt.% F and AF2 doped with 2wt.% F) + 10% pure individual rare earth phosphate crystals.*

[b)] *Aluminum saturation index (ASI) = Al /(Na+K) in mol*

[c)] *Phase present other than glass: M = monazite, X = xenotime, Mi = mica, Fk = feldspar*

[d)] *Solubility product (Ksp) for reaction* $REEPO_4^{melt} \Leftrightarrow REE^{melt} + PO_4^{melt}$

Table 3.12. Experimental data on the solubility of rare earth phosphates (monazite and xenotime) in haplogranitic melts doped with 2 and 4 wt.% F at 800^{o}C and 2 kbar as derived from the extrapolation of measured diffusion profiles (Co).

Run No.	Average (REE) (ppm)	Co (REE) (ppm)	Diffusivities (10^{-11} cm^2/s)	Solubility product (Ksp)* (10^{-5} mol^2/kg^2)
2F1	187±159	388±85	0.82±0.41	3.72±0.14
2F2	235±107	436±58	3.02±1.43	4.50±0.11
2F3	177±40	437±62	1.21±0.42	4.12±0.09
2F4	223±57	329±41	2.58±1.22	3.51±0.08
2F6	386±122	502±50	5.66±3.06	4.86±0.06
2F7	373±141	588±79	3.76±2.17	6.16±0.16
2F8	459±83	607±41	19.55±14.7	6.41±0.06
2F9	330±58	519±36	5.85±2.22	6.07±0.07
2F10	371±123	482±66	2.85±1.45	4.34±0.15
2F11	394±119	417±36	9.44±4.12	3.21±0.03
2F12	434±145	571±56	8.20±5.27	5.04±0.08
2F13	763±122	992±59	8.07±3.82	9.48±0.10
2F14	1178±172	1238±102	5.04±3.24	11.22±0.14
2F15	692±75	1014±139	5.25±4.32	8.72±0.23
4F1	218±78	472±74	1.50±0.70	4.58±0.14
4F2	317±116	517±64	4.79±2.39	5.21±0.13
4F3	207±180	564±88	0.43±0.13	6.40±0.15
4F4	236±72	376±59	5.88±4.42	3.90±0.11
4F6	393±91	501±41	8.36±4.84	5.09±0.06
4F7	296±144	498±84	3.39±2.10	6.06±0.10
4F8	447±126	598±91	7.09±6.32	6.33±0.07
4F9	378±158	593±72	3.70±1.73	7.82±0.11
4F10	529±257	744±122	5.48±5.43	5.80±0.19
4F11	405±99	478±31	40.43±26.5	4.08±0.05
4F12	480±82	568±48	46.32±54.7	5.37±0.08
4F13	882±339	1308±225	5.19±4.82	11.59±0.31
4F14	1649±137	1796±167	8.27±7.21	16.21±0.24
4F15	699±173	1469±301	1.61±0.98	11.80±0.53

* Solubility product using reaction $REEPO_4^{melt} \Leftrightarrow REE^{melt} + PO_4^{melt}$

Table 3.13. Fit parameters for the linear equation (Eq.3.9) relating REE phosphate solubility to fluorine content.

LREE: Y = -3.42*(0.13)*-0.33*(0.01)*X					**HREE: Y = -3.17*(0.15)*-0.34*(0.03)*X**				
	A	Error	B	Error		A	Error	B	Error
La	-3.54	0.17	-0.32	0.06	Tb	-3.26	0.24	-0.33	0.12
Ce	-3.34	0.07	-0.35	0.04	Dy	-3.28	0.08	-0.39	0.05
Pr	-3.58	0.22	-0.36	0.11	Ho	-3.33	0.08	-0.36	0.04
Nd	-3.55	0.20	-0.33	0.10	Er	-3.22	0.03	-0.33	0.03
Sm	-3.36	0.20	-0.32	0.10	Tm	-3.18	0.06	-0.33	0.04
Eu	-3.34	0.17	-0.34	0.09	Yb	-2.93	0.23	-0.29	0.11
Gd	-3.25	0.18	-0.33	0.09	Lu	-2.99	0.23	-0.38	0.12

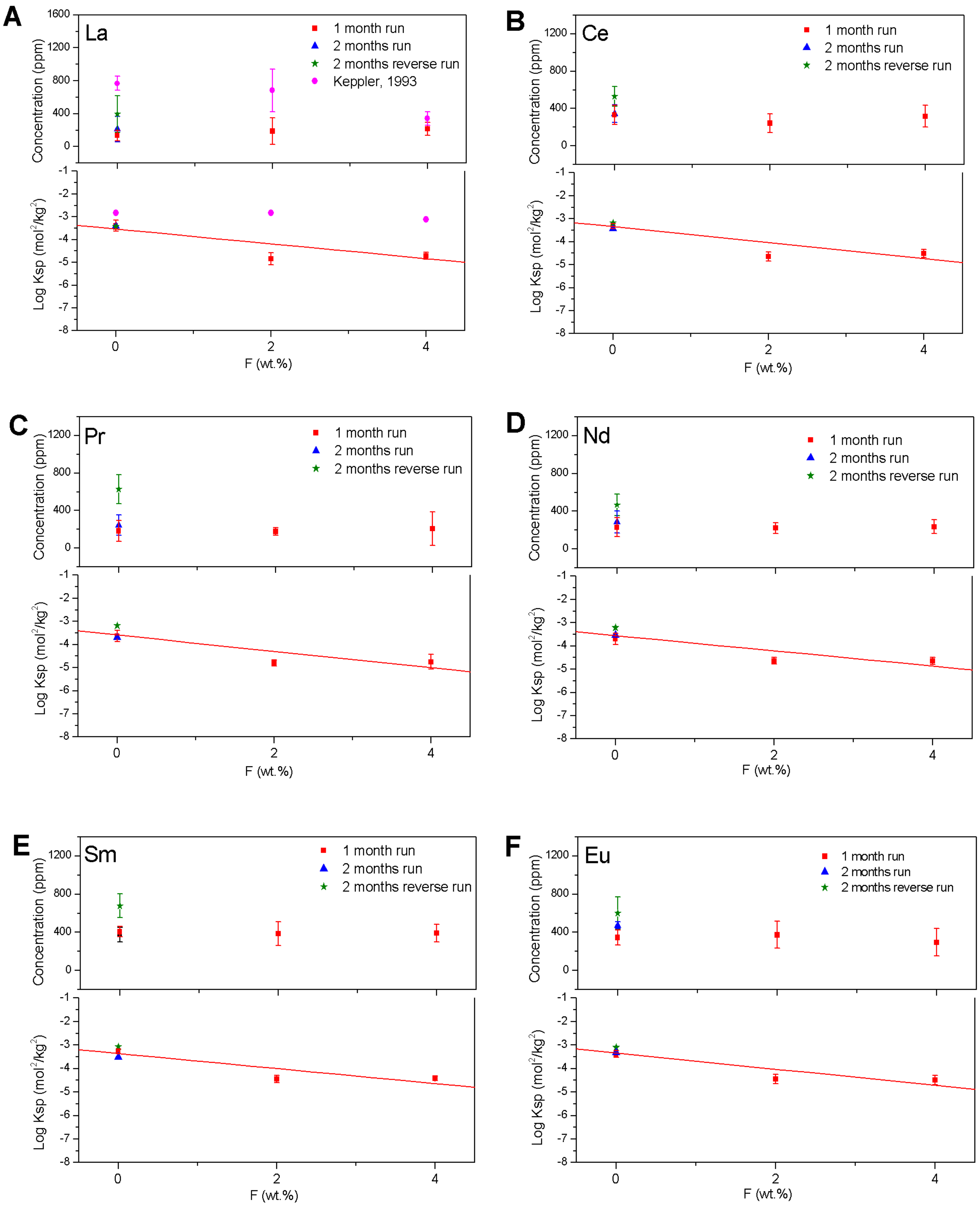

Figure 3.10. Comparison of the solubility of REE phosphates in metaluminous, water saturated haplogranitic melts (ASI=1; 6 wt.% H_2O) at 800°C and 2 kbar with and without fluorine. Vertical error bars represent 1σ error.

Figure 3.10 (continued)

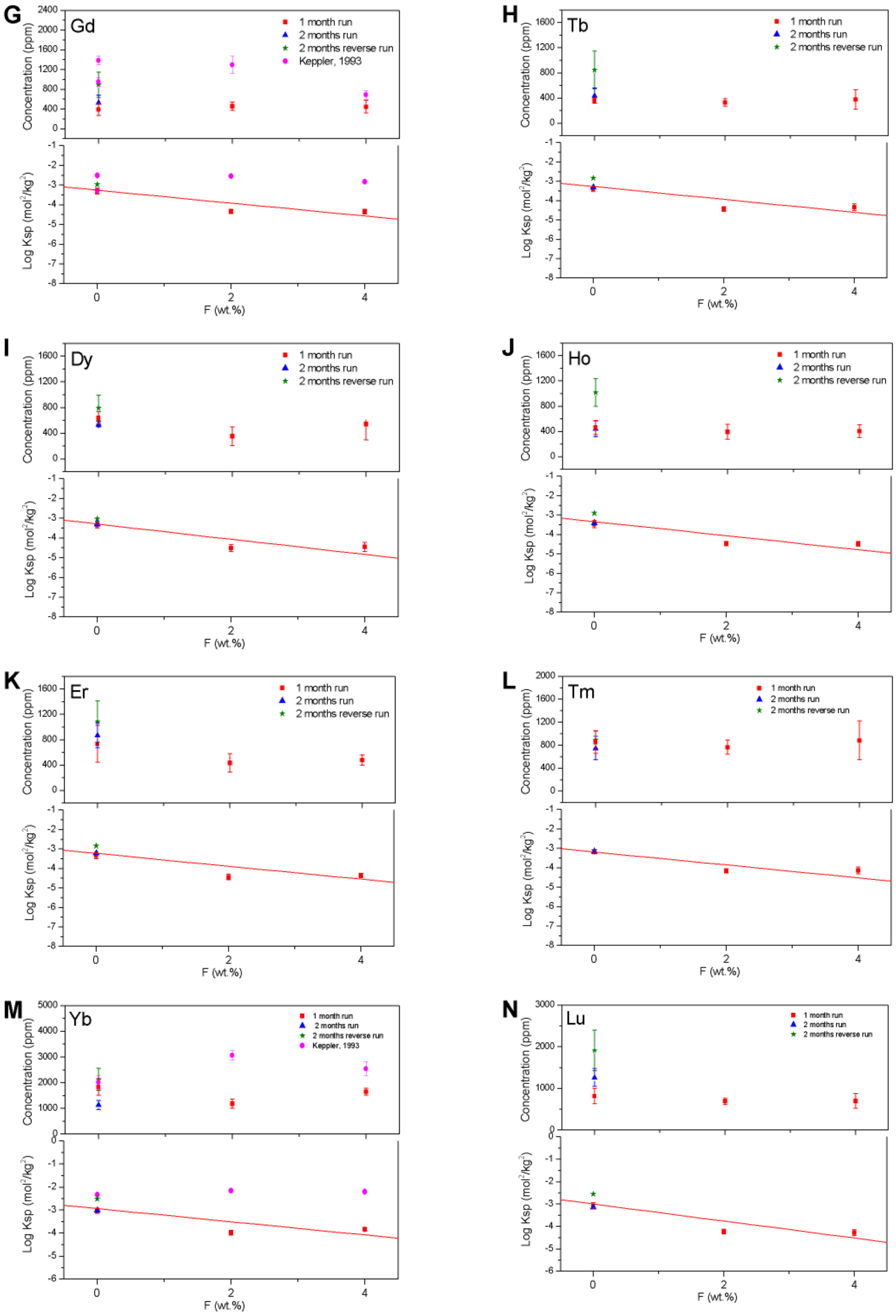

3.4. The effect of temperature on solubility

For the composition with ASI = 1.1 – 1.2, two sets of experiments were carried out at 1100 °C and 800 °C. The results are compared in Figure 3.11. The data at 1100°C are very likely close to equilibrium. They show an increase of solubility from La to Lu with a superimposed tetrad effect.

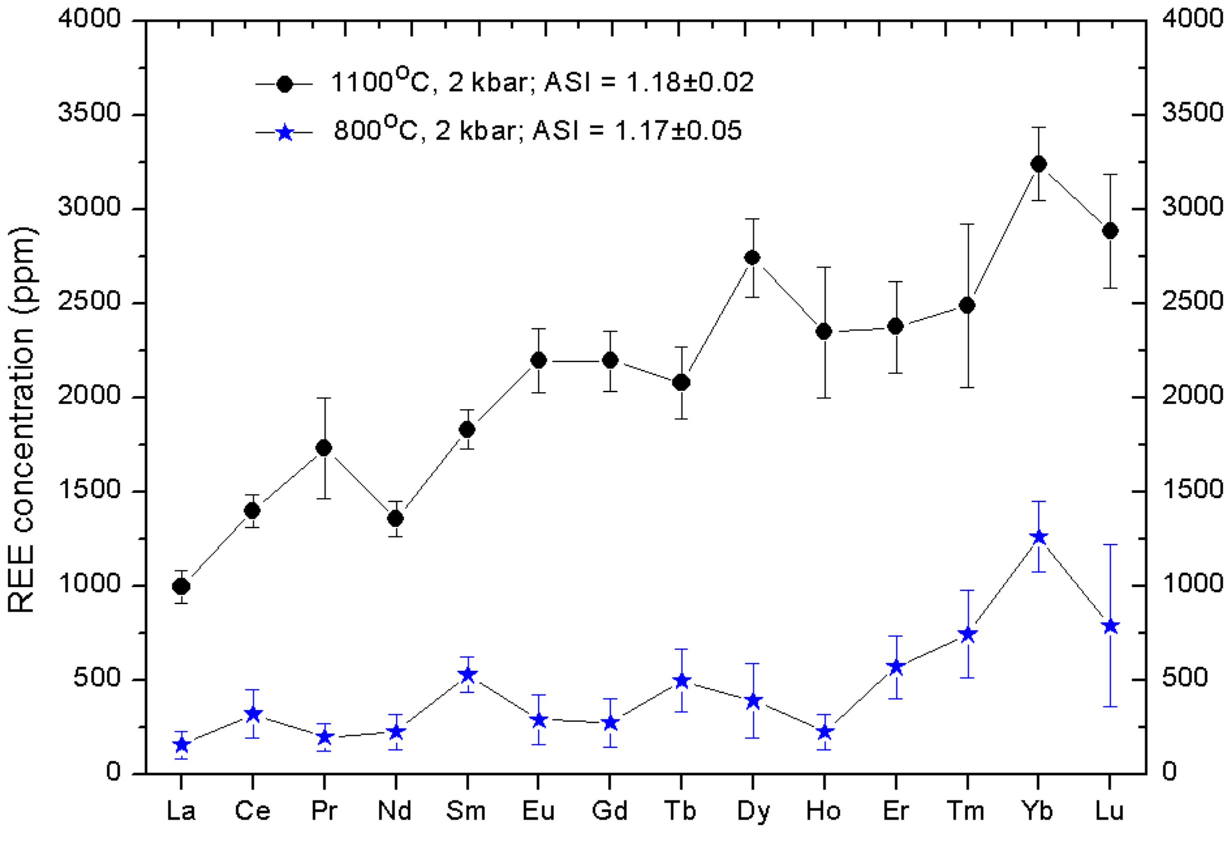

Figure 3.11. Monazite and xenotime solubility in hydrous haplogranitic melts at 800 and 1100 °C as derived from average electron microprobe analyses of run products. Error bars indicate standard deviations of replicated measurement.

Previous experimental solubility data of monazite and xenotime in silicate melt in a wide range of temperature from 1000-1400°C (Hahn et al., 2005; Rapp and Watson, 1986), through 800-1000°C (Keppler, 1993; Montel, 1986; Montel et al., 1993; Rapp and Watson, 1986), to 750°C (Wolf and London, 1995) are roughly in agreement with this study and show that temperature is the most important parameter affecting the solubility of monazite/xenotime in the melt. A small variation of temperature can cause a significant change in monazite solubility in melt (Figure 3.11 and Figure 3.12).

The REE solubility increases with increasing temperature by about two orders of magnitude from 800°C to 1400°C. The temperature dependence can be described by the equation:

$$\mathbf{Y = A + Bx} \qquad \textbf{(Eq. 3.10)}$$

where: Y is the log REE (ppm) and X is the 10^4/T in Kelvin. The fitting results are listed in Table 3.14 and illustrated in Figure 3.12.

Table 3.14. Fit parameters for the linear equation (Eq.3.10) describing the temperature dependence of monazite solubility in hydrous, metaluminous granitic melts.

	A	Error	B	Error	R^2		A	Error	B	Error	R^2
La	5.95	0.21	-0.40	0.03	0.96	Sm	5.75	0.31	-0.33	0.04	0.91
Ce	5.94	0.19	-0.37	0.03	0.95	Gd	5.54	0.51	-0.31	0.06	0.88

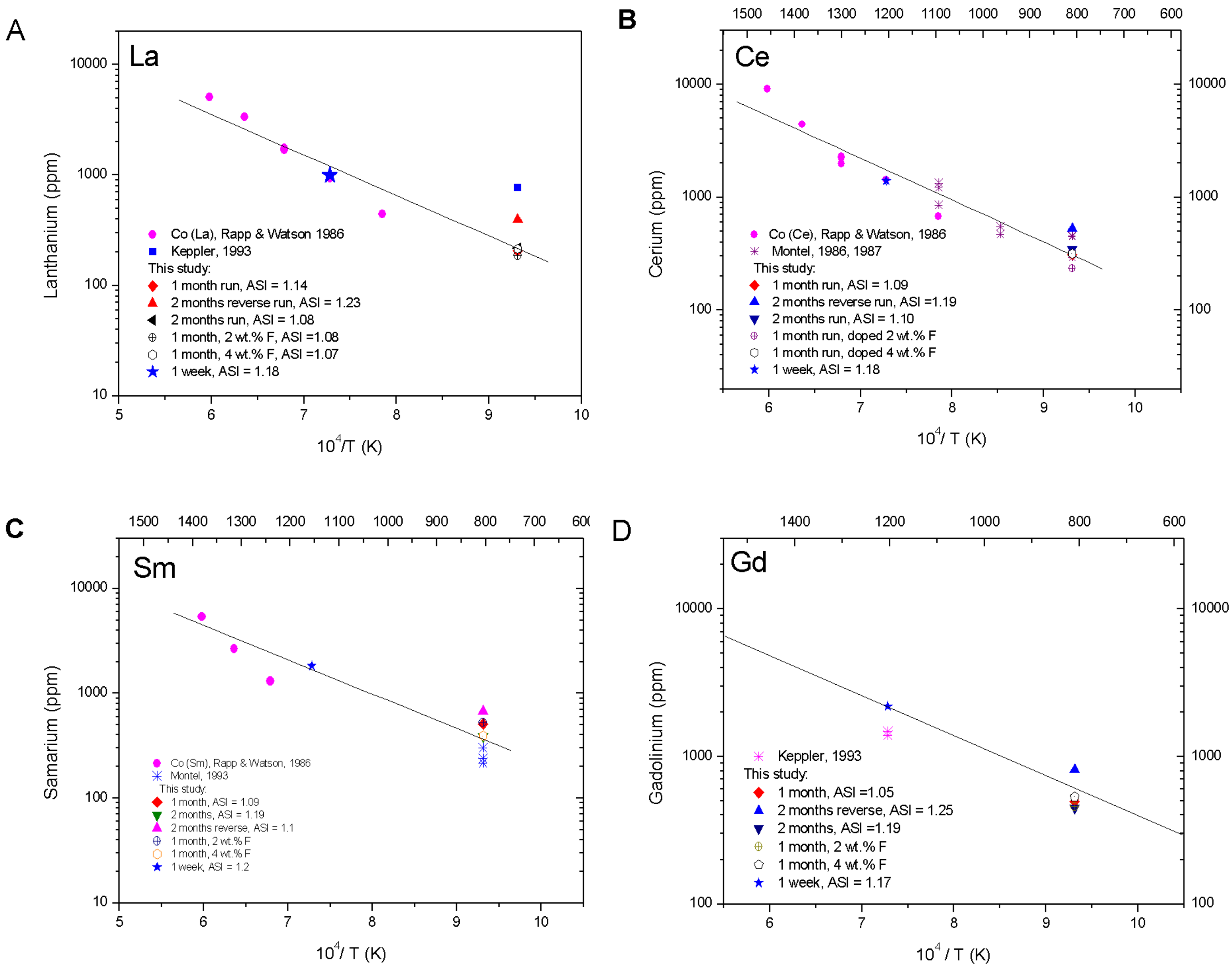

Figure 3.12. The effect of temperature on REE solubility in hydrous granitic melts. ASI refers to the molar Al/(Na+K) ratio of the melt. The nominal composition of starting materials has ASI = 1.

4. Discussion and geological applications

4.1. The dissolution mechanism of monazite and xenotime in haplogranitic melts

One important result of this study is that monazite solubility depends on the phosphorus content of the melt. As pointed out in chapter 3.1., the dependence can be fully described by a model, which assumes that the REE dissolves partially as undissociated $REEPO_4$ species and only a part of them dissociates into REE^{3+} and PO_4^{3-}. Also, the constants, which describe both dissolution mechanisms, depend on composition.

Monazite and xenotime solubility increase strongly with the per-alkalinity of the melt. As noted in chapter 3.1, this increase is primarily due in the concentration of ionic species, i.e. the REE^{3+} cations. Such cations can only be dissolved in a silicate melt, if suitable anions are available for charge balance. A water-free haplogranitic melt with a Al/(Na+K) = 1 is fully polymerized, and no non-bridging oxygen atoms are available to charge-compensate dissolved REE^{3+} ions. If excess Na_2O or K_2O are introduced into the melt, non-bridging oxygen atoms are produced by depolymerization:

$$- Si - O - Si - + Na_2O = - Si - O - Na + Na - O - Si - \qquad \text{(Eq. 4.1)}$$

The non-bridging oxygen atoms which are originally coordinated with Na can then easily exchange Na^+ against REE^{3+} and thereby stabilize rare earth cations in the silicate melt:

$$3\,(- Si - O - Na) + REE^{3+} = (- Si - O -)_3REE + 3\,Na^+ \qquad \text{(Eq. 4.2)}$$

The enhanced solubility of monazite and xenotime in peralkaline melts is therefore not surprising and similar mechanisms have been invoked to explain the increase of the solubility of minerals such a zircon or rutile in peralkaline melts.

More difficult to explain is the fact that monazite and xenotime solubility does not increase significantly in peraluminous melts, i.e. with an excess of Al_2O_3 over Na_2O and K_2O, since this excess should also lead to a depolymerization of the melt and the formation on non-bridging oxygen atoms according to

$$3\,(- Si - O - Si -) + Al_2O_3 = 2\,(- Si - O -)_3Al \qquad \text{(Eq. 4.3)}$$

However, the non-bridging oxygen atoms formed by this reaction are not coordinated by Na^+ or K^+, but by Al^{3+}. Because of the smaller size and higher charge of Al^{3+} as compared to Na^+ and K^+, the chemical bond between Al^{3+} and the non-bridging oxygen atoms is likely to be much stronger and these Al^{3+} ions are therefore not easily exchanged by REE^{3+} as the equation:

$$(-\mathrm{Si}-\mathrm{O}-)_3\mathrm{Al} + \mathrm{REE}^{3+} = (-\mathrm{Si}-\mathrm{O}-)_3\mathrm{REE} + \mathrm{Al}^{3+} \qquad \text{(Eq. 4.4)}$$

In other words, the reaction (Eq.4.4) probably does not easily proceed to the right hand side and therefore, REE^{3+} ions are not easily dissolved in peraluminous melts.

The data in Figure 3.12 and 3.13 shows that fluorine has only a very minor effect on monazite and xenotime solubility. While Keppler (1993) suggested that the solubility does not change with fluorine at all, the new data actually suggest that fluorine actually slightly reduces monazite and xenotime solubility, a rather surprising result. This observation clearly rules out any complexing of REE by fluorine in the melt, as complexing would always increase solubility. The decrease in solubility must be due to some indirect effects, possibly related to coordination changes of Al in the melt, which have been demonstrated in nuclear magnetic resonance (NMR) studies of quenched haplogranitic glasses (e.g. Schaller et al., 1992).

4.2. Rare earth element fractionation by monazite and xenotime

The partition coefficients of individual REE between monazite or xenotime and melt can be calculated from the solubility data obtained in this study, if one assumes that the various REE in monazite or xenotime mix nearly ideally. In the light of the identical charge and very similar ionic radius of the light REE entering monazite and of the heavy REE entering xenotime, this is probably a very reasonable assumption. The solubility data (in ppm REE) shown in Figure 3.7 and several subsequent figures are therefore approximately proportional to the inverse of the monazite/melt and xenotime/melt partition coefficients, i.e. they show directly the relative enrichment pattern that is to be expected for a melt coexisting with monazite and xenotime. Those REE with a higher solubility of the pure individual $REEPO_4$ in the melt will partition more strongly into the melt when it is in equilibrium with a monazite or xenotime solid solution. On the other hand, those REE with lower solubility of the corresponding pure phosphate will partition less into the melt.

Rare earth elements are normally incompatible, with the exception of some heavy REE that are compatible in garnet and only mildly incompatible in clinopyroxene and amphibole (see chapter 1 and references therein). Fractionation of normal ferromagnesian minerals will therefore lead to an enrichment of the light REE in the residual melt. The effect of monazite and xenotime on REE fractionation, as shown by the experimental data in chapter 3, is opposite to this trend. The rare earth phosphates of the heavy REE are more soluble than the light REE. This means that in equilibrium with a monazite or xenotime solid solution, the heavy REE will partition more strongly into the melt phase.

This means that it should be easy to distinguish whether some feslsic magma has already fractionated monazite or not. Monazite fractionation as well as the simultaneous fractionation of monazite and xenotime should ultimately lead to an REE pattern with distinct enrichment of the heavy REE over the light REE. However, when interpreting the actual REE pattern of a granitic magma, it should be kept in mind that most primary magmas have probably inherited a light REE enrichment from their source. Partial melting of a primitive mantle source leads to a light REE enrichment in the magma an subsequent fractionation of ferromagnesian minerals will further enhance this LREE enrichment. Therefore, most protoliths for the generation of granitic magmas will be LREE enriched, even if the granite is not of the A type which can sometimes be traced back to the direct differentiation of a mantle-derived magma.

The most likely effect of monazite or combined monazite or xenotime fractionation is therefore that it will gradually change a REE pattern with light REE enrichment into a more or less flat pattern until finally a heavy REE enriched pattern is obtained. This change in slope of the REE pattern is indeed seen in some highly evolved granites when they are compared to their primitive types (e.g. Irber, 1999). Interestingly, the granites with flat or heavy REE enriched patterns often show a clear lanthanide tetrad effect.

4.3. The origin of the lanthanide tetrad effect in granitic rocks

Some highly evolved granites show rare earth abundance patterns that are not smooth; sometimes these patterns appear to be separated into four segments, the “tetrades”(e. g. Masuda & Akagi 1989, Lee et al. 1994, Kawabe 1995, Bau 1996, Jahn et al. 2001, Liu & Zhang 2005). This “lanthanide tetrad effect” has been reported since a long lime, but it was sometimes dismissed as analytical artifact. With recent advances in trace element analyses, however, it is unquestionable that the effect is real. Since it usually occurs in volatile-rich, highly fractionated granites, the lanthanide tetrad effect has often been attributed to fluid interaction (e.g. Bau 1996). Sometimes the appearance of such a tetrad effect was even believed to be diagnostic for granitic magmas that have interacted with a fluid. In an experimental study, Veksler et at. (2005) observed some weak lanthanide tetrad effect in the partitioning of REE between silicate melts and fluoride melts and suggested that immiscible fluoride melts are responsible for the origin of the tetrad effect in natural granites. However, field evidence for such immiscible fluoride melts has never been observed.

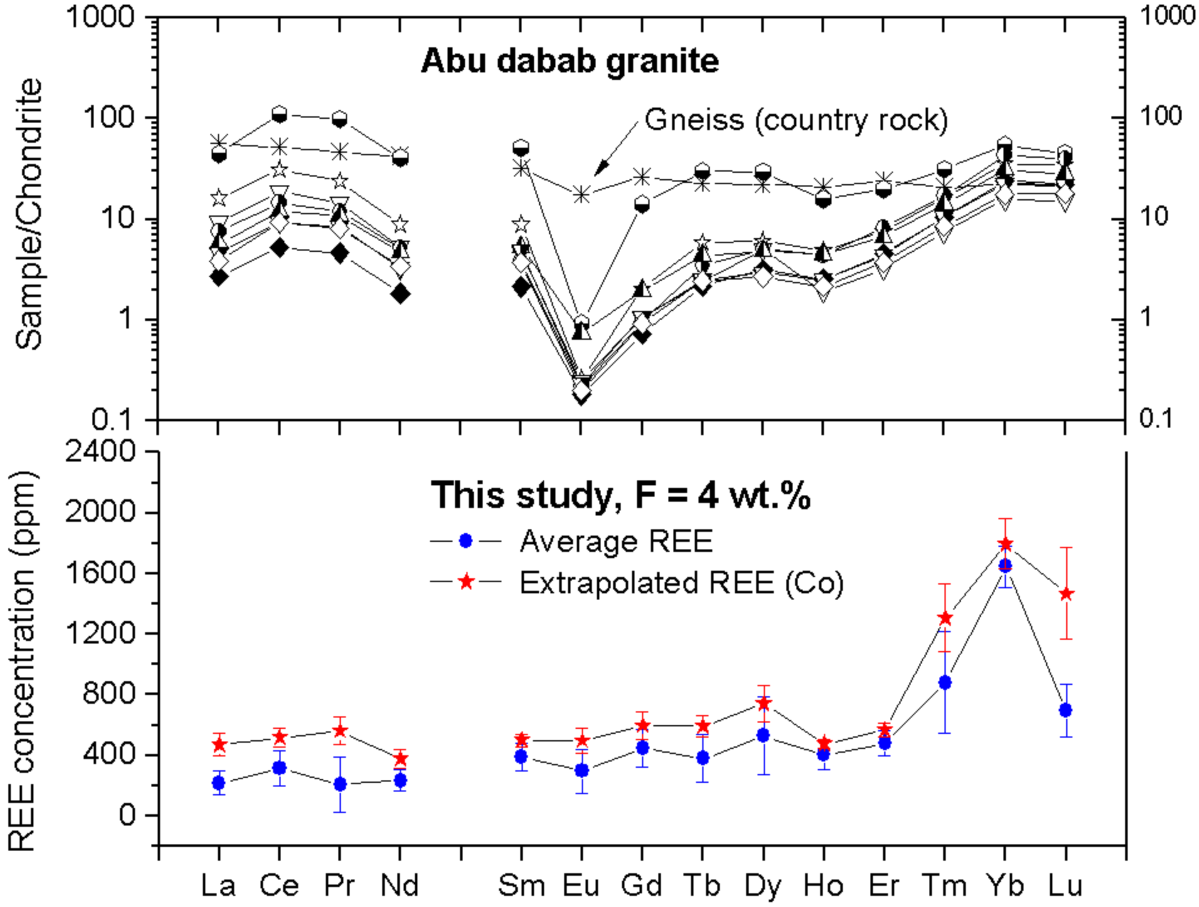

Figure 4.1. Comparison of the REE abundance in the Abu Dabbab granite from Egypt with clear tetrad pattern (after Bau, 1996) and the monazite and xenotime solubility of a fluorine-bearing, slightly peraluminous hydrous haplogranite. Assuming ideal miscibility in the monazite and xenotime crystals, the solubilities are directly proportional to the melt/monazite and melt/xenotime partition coefficients of the respective REE. The similarity between the two patterns is striking. The negative Eu anomaly seen in the Abu Dabbab pattern is due to plagioclase fractionation and therefore does not occur in the solubility pattern.

The origin of the lanthanide tetrad effect needs to be completely reconsidered in the light of the present study. As shown in chapter 3, monazite and xenotime solubility is not a smooth function of atomic number or ionic radius of the REE, but it rather shows pronounced tetrad patterns. These patterns are particularly obvious for peralkaline melts, but they are also clearly seen in some fluorine-bearing melts. Figure 4.1 compares the REE pattern of the Abu Daddad granite in Egypt, famous for its lanthanide tetrad pattern, with the solubility data of monazite and xenotime measured for a slightly peraluminous, fluorine-bearing haplogranitic melt. The similarity of the two patterns is striking. Moreover, some of the prominent features observed in the Abu Daddad pattern as well as in the REE patterns of many highly evolved granites are seen in virtually all experimental data on monazite and xenotime solubility, irrespective of melt composition. In particular, the solubility maximum at ytterbium is virtually always visible.

From the experimental data presented in this study, one can therefore conclude that the lanthanide tetrad effect in highly evolved granites can be explained by monazite and xenotime fractionation. In fluorine-bearing, volatile-rich granites the effect may be particularly strong, because the high fluorine and water content strongly reduces the viscosities of these magmas and therefore facilitates gravitative settling of crystals. There is no need to invoke any exotic agents such as immiscible fluoride melts in order to explain the origin of the tetrad effect. Moreover, the tetrad effect can certainly not be used as an indicator of fluid-rock or fluid-melt interaction.

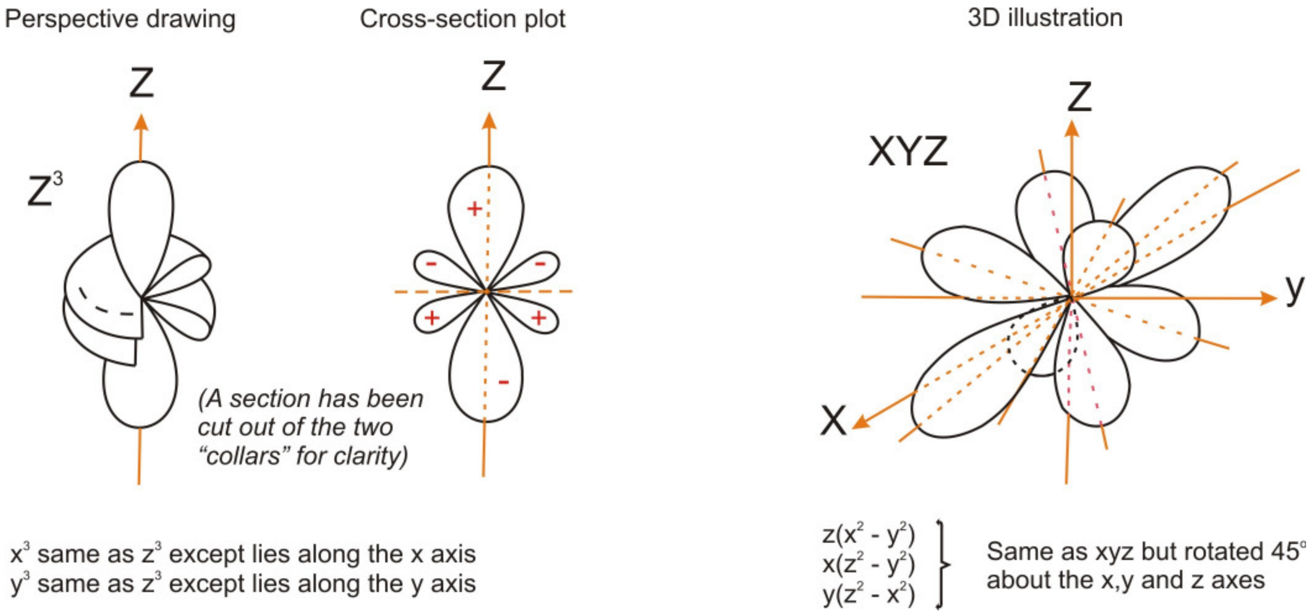

Figure 4.2. Shapes of f-orbitals (after Huheey, 1983)

The lanthanide tetrad effect can probably be traced back to the electrostatic repulsion between partially filled f-orbitals of REE cations and the surrounding anions (oxygen atoms). For this, the shapes of the f orbitals need to be considered. There are a total of seven f orbitals and their shapes fall into two groups, which are depicted in Figure 4.2. One group (x^3, y^3 and z^3 orbitals) has maxima of charge density in the direction of the three Cartesian coordinate axes. The other four orbitals have maxima of charge density in between the coordinate axes. Now consider a REE cation in an octahedral environment. An octahedron can be inscribed into a Cartesian coordinate system in such a way that the six anions (oxygen atoms) are sitting on the coordinate axes. This means that for example, there will be strong repulsion between these anions and the x^3, y^3 and z^3 f-orbitals, because their negative charge is concentrated on the coordinate axes and therefore directly points towards the anions. On the other hand, the charge density of a xyz f-orbital (Fig. 4.2) is concentrated between the coordinate axes, therefore the repulsion with the surrounding anions in octahedral coordination will be small. In an octahedral coordination environment, a REE cation with filled x^3, y^3 or z^3 f-orbitals will therefore be less stable than a REE ion with filled xyz orbital. However, for a cubic, eight-fold coordination, the situation is reversed: the eight lobes of the xyz f-orbital (Fig. 4.2) point exactly into the corner of a cube, where the coordinating anions are located. Due to electronic repulsion, a REE with a filled yxz orbital is therefore destabilized in an eightfold coordinated environment, while a REE with filled x^3, y^3 or z^3 orbital experiences much less electronic repulsion in cubic coordination geometry.

From the consideration outlined above it is obvious that the preference of a given REE cation for octahedral or cubic coordination will depend on the type of f-orbital filled and the partition coefficients between two phases with different coordination environment will therefore depend on the precise electronic configuration, not just on ionic radius. This is probably the essential physics behind the lanthanide tetrad effect. An essential requirement for this effect to occur is therefore that the coordination geometry of the REE between the phases of interest is different. This explains why monazite or xenotime fractionation produces a tetrad effect. The coordination number of middle and heavy REE in most silicate glasses is around 6 (Ponader and Brown, 1989). In xenotime, however, the REE occupy a very unusual, asymmetric eightfold-coordinated environment and in monazite, they are in a very unusual nine-fold coordination. The appearance of a tetrad effect during the fractionation between these phases and silicate melts is therefore not surprising. On the other hand, in most ferromagnesian minerals, such as clinopyroxene or garnet, the REE occupy octahedral sites similar to their environment in silicate melts and not surprisingly, the partitioning between these phases and the melt is exclusively controlled by ionic radius.

4.4. The use of monazite solubilities as geothermometer

Temperature clearly has a strong effect on monazite solubility in granitic melts (see chapter 3.4). Accordingly, the REE content of a quenched granitic melt that once was in equilibrium with monazite could in principle be used to estimate temperature. Montel (1993) proposed an equation (Eq.1.2) (see chapter 1.7.3), which calculates monazite solubility based on temperature, water content and bulk composition of the melt only.

According to the results of the present study, this equation has a number of problems:

(1) It does not take into account that monazite solubility depends on phosphorus content. As pointed out in chapter 3.1., monazite dissolves in granitic melt as both ionic and molecular species (REE^{3+} and $REEPO_4$). In order to fully describe this reaction, two separate equilibrium constants need to be

known. Both equilibrium constants presumably depend on temperature and also on bulk composition. Any reasonable thermodynamic model for monazite solubility would need to take this into account.

(2) The model does not discriminate between different REE elements. The present study shows that even neighboring rare earth elements sometimes have solubilities that are different by more than a factor of two. Moreover, while the solubility of all other REE phosphates strongly increases with peralkalinity, this effect is not clearly seen for lanthanum.

(3) The equation by Montel would predict a continuous change of solubility with ASI both in the peralkaline and the peraluminous field, while experimental data show no significant variation in the peraluminous field at all.

Therefore, simple models of monazite solubility like the one proposed by Montel (1993) should be used with caution. These models probably allow some approximate estimate of temperature for melts with ASI close to 1 and with "normal" phosphoruus contents around 0.1 wt. % or less. They should not be used for strongly peralkaline or peraluminous melts, or for melts with high phosphorus content. Figure 4.3. gives some idea what kind of errors in temperature can be expected when applying the equation of Montel (1993). In this figure, we show the temperatures calculated from the experimentally observed solubilities in various experiments reported in this study using the model by Montel. In reality, all the experiments were carried out at 800°C (A) and 1100°C (B).

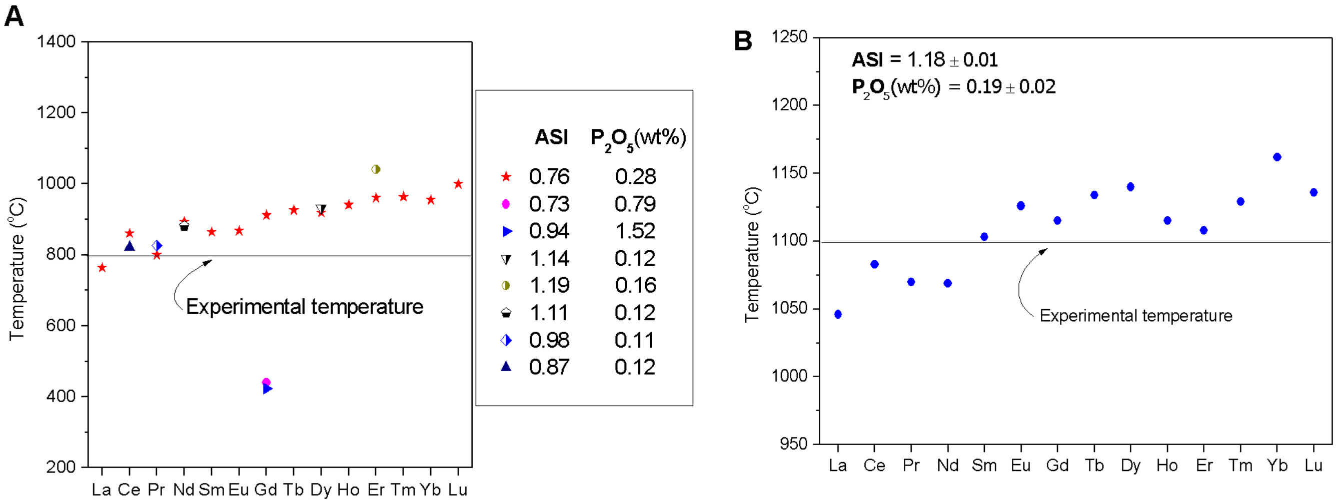

Figure 4.3. Temperatures calculated from experimentally determined monazite solubilities using the model of Montel (1993). In reality, all the experiments were carried out at 800°C (A) and at 1100°C (B)

References

1. Adam J. et al. (1994) The effects of pressure and temperature on the partitioning of Ti, Sr and REE between amphibole, clinopyroxene and basanitic melts. In *Trace-element partitioning with application to magmatic processes*. Elsevier, Amsterdam, Netherlands, pp. 219-233.

2. Adam J., Green T. H., and Ulmer-Peter c. (2003) The influence of pressure, mineral composition and water on trace element partitioning between clinopyroxene, amphibole and basanitic melts. In *Ninth international symposium on Experimental mineralogy, petrology and geochemistry*. Schweizerbart'sche Verlagsbuchhandlung (Naegele u, Obermiller). Stuttgart, Federal Republic of Germany, pp. 831-841.

3. Akagi T., Shabani M., and Masuda A. (1993) Lanthanide tetrad effect in kimuraite [$CaY_2(CO_3)_4.6H_2O$]; implication for a new geochemical index. *Geochimica et Cosmochimica Acta* **57**, 2899-2905.

4. Aller L. H. (1987) Chemical abundances. In Spectroscopy of Astrophysical Plasmas (eds. A. Dalgarno and D. Layzer). Cambridge University Press, pp. 89-124.

5. Anderson A. (1961) Thorium mineralization in the Lemhi Pass area, Lemhi County, Idaho. *Economic Geology and the Bulletin of the Society of Economic Geologists* **56**, 177-197.

6. Anderson D. L., Zhang Y. S., and Tanimoto T. (1992) Plume heads, continental lithosphere, flood basalts and tomography. In *Magmatism and the Causes of Continental Break-up, vol 68* (eds. B.C.Storey, T.Alabaster, and R.J.Pankhurst). Geol. Soc. Lond., London, pp. 99-124.

7. Andreoli M., Smith C., Watkeys M., Moore J., Ashwal L., and Hart R. (1994) The geology of the Steenkampskraal monazite deposit, South Africa; implications for REE-Th-Cu mineralization in charnockite-granulite terranes. *Economic Geology and the Bulletin of the Society of Economic Geologists* **89**, 994-1016.

8. Barth M. G., Foley S. F., and Horn I. (1997) Experimental trace-element partitioning in tonalitic systems. In *Seventh annual V. M. Goldschmidt conference* Lunar and Planetary Institute, Houston, TX, United States, p. 18.

9. Bau M. (1996) Controls on the fractionation of isovalent trace elements in magmatic and aqueous systems: Evidence from Y/Ho, Zr/Hf, and lanthanide tetrad effect. *Contributions to Mineralogy and Petrology* **123**, 323-333.

10. Bau M. (1997) The lanthanide tetrad effect in highly evolved felsic igneous rocks - a reply to the comment by Y. Pan. *Contributions to Mineralogy and Petrology* **128**, 409-412.

11. Bea F. (1996) Residence of REE, Y, Th and U in granites and crustal protoliths; implications for the chemistry of crustal melts. *Journal of Petrology* **37**, 521-552.

12. Bea F. et al. (1994) Mineral/ leucosome trace-element partitioning in a peraluminous migmatite (a laser ablation-ICP-MS study). In *Trace-element partitioning with application to magmatic processes* Elsevier, Amsterdam, Netherlands, pp. 291-312.

13. Beattie P. (1994) Systematics and energetics of trace element partitioning between olivine and silicate melts: Implications for the nature of mineral/melt partitioning. *Chemical Geology* **117**, 57-71.

14. Behrens H. (1995) Determination of water solubilities in high-viscosity melts; an experimental study on $NaAlSi_3O_8$ and $KAlSi_3O_8$ melts. *European Journal of Mineralogy* **7**, 905-920.

15. Berndt J., Liebske C., Holtz F., Freise M., Nowak M., Ziegenbein D., Hurkuck W., Koepke J., ronson-James p., and Bish D. L. (2002) A combined rapid-quench and H_2 -membrane setup for internally heated pressure vessels; description and application for water solubility in basaltic melts. *American Mineralogist* **87**, 1717-1726.

16. Boatner L. A. et al. (1981) Lanthanide orthophosphates for the primary immobilization of actinide wastes. Management of Alpha-Contaminated Wastes. In *Proceedings of the International Symposium.* International Atomic Energy Agency, Vienna, pp. 411 -422.

17. Boatner L. A. et al. (2002) Synthesis, structure, and properties of monazite, pretulite, and xenotime. In *Phosphates; geochemical, geobiological, and materials importance* Mineralogical Society of America and Geochemical Society, Washington, DC, United States, pp. 87-121.

18. Boynton W. V. (1984) Cosmochemistry of the rare earth elements; meteorite studies. In *Rare earth element geochemistry* (ed. P. Henderson). Elsevier Sci, Publ. Co.. Amsterdam, Netherlands, pp. 63-114.

19. Breiter K. et al. (1997) Mineralogical evidence for two magmatic stages in the evolution of an extremely fractionated P-rich rare-metal granite; the Podlesi Stock, Krusne Hory, Czech Republic. In *High level silicic magmatism and related hydrothermal systems; IAVCEI '97 selected papers* Clarendon Press, Oxford, United Kingdom, pp. 1723-1739.

20. Byrne R. and Li B. (1995) Comparative complexation behavior of the rare earths. *Geochimica et Cosmochimica Acta* **59**, 4575-4589.

21. Cetiner Z. S., Wood S. A., and Gammons C. H. (2005) The aqueous geochemistry of rare earth elements. Part XIV. The solubility of rare earth element phosphate from 23 to 150 ^{o}C. *Chemical Geology* **217**, 147-169.

22. Chao E. C. T. et al. (1992) Host-rock controlled epigenetic, hydrothermal metasomatic origin of the Bayan Obo REE-Fe-Nb ore deposit, Inner Mongolia, P.R.C. In *Minerals for future materials* Pergamon, Oxford-New York-Beijing, International, pp. 443-458.

23. Colson R., McKay G., and Taylor L. (1988) Temperature and composition dependencies of trace element partitioning; olivine/ melt and low-Ca pyroxene/melt. *Geochimica et Cosmochimica Acta* **52**, 539-553.

24. Coppin F., Berger G., Bauer A., Castet S., and Loubet M. (2002) Sorption of lanthanides on smectite and kaolinite. *Chemical Geology* **182**, 57-68.

25. Cuney M. and Friedrich M. (1987) Physicochemical and crystal-chemical controls on accessory mineral paragenesis in granitoids; implications for uranium metallogenesis. In *Les mecanismes de concentration de l'uranium dans les environnements geologiques;* colloque international Translated Title: *Mechanisms of uranium concentration in the geologic environment;* international colloquium pp. 235-247.

26. De Baar H. J. W., Bacon M. p., Brewer P. G., and Bruland K. W. (1985) Rare earth elements in the Pacific and Atlantic oceans. *Geochimica et Cosmochimica Acta* **49**, 1943-1959.

27. Drake M. J. and Weill D. F. (1975) Partition of Sr, Ba, Ca, Y, Eu^{2+} , Eu^{3+} , and other REE between plagioclase feldspar and magmatic liquid; an experimental study. *Geochimica et Cosmochimica Acta.* **39**, 689-712.

28. Drake M. J. and Weill D. F. (1972) New rare earth elements standards for electron microprobe analysis. *Chem. Geol.* **10**, 179-181.

29. Dunn T. (1987) Partitioning of Hf, Lu, Ti, and Mn between olivine, clinopyroxene and basaltic liquid. *Contributions to Mineralogy and Petrology* **96**, 476-484.

30. Edgar A. D. (1973) Experimental petrology: Basic principles and techniques. Clarendon, Oxford.

31. Elderfield H. and Greaves M. (1982) The rare earth elements in seawater. *Nature (London)* **296**, 214-219.

32. Evans J. and Zalasiewicz J. (1996) U-Pb, Pb-Pb and Sm-Nd dating of authigenic monazite; implications for the diagenetic evolution of the Welsh Basin. *Earth and Planetary Science Letters* **144**, 421-433.

33. Evans O. C. and Hanson G. N. (1993) Accessory-mineral fractionation of rare-earth element (REE) abundances in granitoid rocks. *Chemical Geology* **110**, 69-93.

34. Ewing R. C., Wang L. M., Kohn M. J., Rakovan J.; Hughes J. M. (2002) Phosphates as nuclear waste forms. In *Phosphates; geochemical, geobiological, and materials importance* Mineralogical Society of America and Geochemical Society, Washington, DC, United States, pp. 673-699.

35. Fidelis I. and Siekierski S. (1971) Regularities or tetrad effect in complex formation by f-electron elements: Double-double effect. *J. Inorg. Nucl. Chem.* **33**, 3191-3194.

36. Foerster H. (1998) The chemical composition of REE-Y-Th-U-rich accessory minerals in peraluminous granites of the Erzgebirge-Fichtelgebirge region, Germany; Part II, Xenotime. *American Mineralogist* **83**, 1302-1315.

37. Franz G., Andrehs G., and Rhede D. (1996) Crystal chemistry of monazite and xenotime from Saxothuringian-Moldanubian metapelites, NE Bavaria, Germany. *European Journal of Mineralogy* **8**, 1097-1118.

38. Frey F. A., Walker N., Stakes D., Walker S.R., and Nielsen R. (1993) Geochemical characteristics of basaltic glasses from the AMAR and FAMOUS axial valleys, Mid-Atlantic Ridge (36^o-37^oN). *Earth. Plan. Sci. Lett.* **115**, 117-136.

39. Fryer B. J. and Taylor R. P. (1987) Rare-earth element distributions in uraninites; implications for ore genesis. *Chemical Geology* **63**, 101-108.

40. Fujimaki H., Tatsumoto M., and Aoke A. (1984) Partition coefficient of Hf, Zr and REE between phenocrysts and groundmasses. *J. Geophy. Res.* **89**, 662-672.

41. Ganapathy R. and Anders E. (1974) Bulk compositions of the Moon and Earth, estimated from meteorites. In *Chemical and isotope analyses; organic chemistry* (ed. W. A. Gose). Pergamon Press, New York, N.Y., United States, pp. 1181-1206.

42. Goldschmidt V. M. (1954) *Geochemistry.* Clareton Press, Oxford, 730 p.

43. Gratz R. and Heinrich W. (1997) Monazite-xenotime thermobarometry: Experimental calibration of the miscibility gap in the binary system CePO4-YPO4. *American Mineralogist* **82**, 772-780.

44. Green T. and Pearson N. (1985) Rare earth element partitioning between clinopyroxene and silicate liquid at moderate to high pressure. *Contributions to Mineralogy and Petrology* **91**, 24-36.

45. Green T. H, Blundy J. D., Adam J., Yaxley, G. M., Austrheim H. and Griffin,W.L. (2000) SIMS determination of trace element partition coefficients between garnet, clinopyroxene and hydrous basaltic liquids at 2-7.5 GPa and 1080-1200 °C. In *Element partitioning in geochemistry and petrology; special volume in honour of Brenda B.* Jensen Elsevier, Amsterdam, International, pp. 165-187.

46. Green T. H. (1994) Experimental studies of trace-element partitioning applicable to igneous petrogenesis - Sedona 16 years later. *Chemical Geology* **117**, 1-36.

47. Hack P. J., Nielsen R. L., Johnston A. D., Foley S. F. and Van-der-Laan S. R. (1994) Experimentally determined rare-earth element and Y partitioning behavior between clinopyroxene and basaltic liquids at pressures up to 20 kbar. In *Trace-element partitioning with application to magmatic processes* Elsevier, Amsterdam, Netherlands, pp. 89-105.

48. Hahn M., Behrens H., Tegge S. A., Koepke J., Horn I., Rickers K., Falkenberg G., Wiedenbeck M., Woodland A. B., and Foley S. F. (2005) Trace element diffusion in rhyolitic melts; comparison between synchrotron radiation X-ray fluorescence microanalysis (mu -SRXRF) and secondary ion mass spectrometry (SIMS). *European Journal of Mineralogy* **17**, 233-242.

49. Harrison T. M., Catlos E. J., Montel J. M., Kohn M. J., Rakovan J., and Hughes J. M. (2002) U-Th-Pb dating of phosphate minerals. In *Phosphates; geochemical, geobiological, and materials importance* Mineralogical Society of America and Geochemical Society, Washington, DC, United States, pp. 523-558.

50. Heinrich W., Andrehs G., and Franz G. (1997) Monazite-xenotime miscibility gap thermometry; 1, An empirical calibration. *Journal of Metamorphic Geology* **15**, 3-16.

51. Henderson P. (1984) General geochemical properties and abundances of the rare earth elements. In *Rare earth element geochemistry* (ed. P. Henderson). Elsevier Sci, Publ. Co.. Amsterdam, Netherlands, pp. 1-32.

52. Hess P. C. (1989) *Origin of Igneous rocks.* Harvard University Press.

53. Higuchi H. and Nagasawa H. (1969) Partition of trace elements between rock forming minerals and the host volcanic rocks. *Earth Planet. Sci. Lett.* **7**, 281.-287.

54. Hollings P. and Wyman D. (2004) The geochemistry of trace elements in igneous system: Principles and examples from basaltic system. In *Rare element geochemistry and mineral deposits. Geological Association of Canada. Short course notes. Volume 17.* (eds. R. L. Linnen and I. M. Samson). pp. 1-16.

55. Holloway J. R. (1971) Internally heated pressure vessels. In *Research techniques for high pressure and high temperatures.* (ed. G.C.Ulmer). Springer- Verlag, New York, pp. 217-258.

56. Huebner J. (1971) Buffering techniques for hydrostatic systems at elevated pressures. In *Research techniques for high pressure and high temperature* (ed. G. C. Ulmer). Springer-Verlag, New York, pp. 123-177.

57. Huheey J. E. (1983) Inorganic chemistry. Harper, Cambridge.

58. Irber W. et al. (1997) Experimental, geochemical, mineralogical and O-isotope constraints on the late-magmatic history of the Fichtelgebirge granites (Germany). In *The German Deep Drilling Project, KTB* Springer International, Berlin, Federal Republic of Germany, p. S110-S124.

59. Irber W. (1999) The lanthanide tetrad effect and its correlation with K/Rb, Eu/Eu*, Sr/Eu, Y/Ho, and Zr/Hf of evolving peraluminous granite suites. *Geochimica et Cosmochimica Acta* **63**, 489-508.

60. Jahn B. M., Wu F., Capdevila R., Martineau F., Zhao Z., and Wang Y. (2001) Highly evolved juvenile granites with tetrad REE patterns: The Woduhe and Baerzhe granites from the Great Xing'an Mountains in NE China. *Lithos* **59**, 171-198.

61. Johannes W. and Holtz F. (1996) *Petrognenesis and experimental petrology of granitic rocks.* Springer.

62. Jolliff B., Papike J., Shearer C., and Shimizu N. (1989) Inter- and intra-crystal REE variations in apatite from the Bob Ingersoll Pegmatite, Black Hills, South Dakota. *Geochimica et Cosmochimica Acta* **53**, 429-441.

63. Kawabe I., Kitahara Y., and Naito K. (1991) Non-chondritic yttrium/holmium ratio and lanthanide tetrad effect observed in pre-Cenozoic limestones. *Geochemical Journal* **25**, 31-44.

64. Kawabe I. (1995) Tetrad effects and fine structures of REE abundance patterns of granitic and rhyolitic rocks; ICP-AES determination of REE and Y in eight GSJ reference rocks. *Geochemical Journal* **29**, 213-230.

65. Kennedy A., Lofgren G., and Wasserburg G. (1993) An experimental study of trace element partitioning between olivine, orthopyroxene and melt in chondrules; equilibrium values and kinetic effects. *Earth and Planetary Science Letters* **115**, 177-195.

66. Keppler H. (1993) Influence of fluorine on the enrichment of high field strength trace elements in granitic rocks. *Contributions to Mineralogy and Petrology* **114**, 479-488.

67. Kerrick D. M. (1987) Cold-seal systems. In *Hydrothermal experimental techniques* (eds. G. C. Ulmer and H. L. Barnes). John Wiley & Sons, New York, NY, United States, pp. 293-323.

68. Klinkhammer G., Elderfield H., Edmond J., and Mitra A. (1994) Geochemical implications of rare earth element patterns in hydrothermal fluids from mid-ocean ridges. *Geochimica et Cosmochimica Acta* **58**, 5105-5113.

69. Kolitsch U. and Holtstam D. (2004) Crystal chemistry of $REEXO_4$ compounds (X = P, As, V); II, Review of $REEXO_4$ compounds and their stability fields. *European Journal of Mineralogy* **16**, 117-126.

70. Lee D. and Bastron H. (1967) Fractionation of rare-earth elements in allanite and monazite as related to geology of the Mount Wheeler Mine area, Nevada. *Geochimica et Cosmochimica Acta* **31**, 339-356.

71. Linnen R. L. and Cuney M. (2004) Granite-related rare element deposits and experimental constrants on Ta-Nb-W-Sn-Zr-Hf mineralization. In *Rare element geochemistry and mineral deposits* (eds. R. L. Linnen and I. M. Samson). Geological Association of Canada, pp. 45-68.

72. Liu C. and Zhang H. (2005) The lanthanide tetrad effect in apatite from the Altay No. 3 pegmatite, Xingjiang, China; an intrinsic feature of the pegmatite magma. *Chemical Geology* **214**, 61-77.

73. Lofgren G. (1987) Internally heated systems. In *Hydrothermal experimental techniques* (eds. G. C. Ulmer and H. L. Barnes). John Wiley & Sons, New York, NY, United States, pp. 324-332.

74. London D., Wolf M., Morgan G., and Garrido M. (1999) Experimental silicate-phosphate equilibria in peraluminous granitic magmas, with a case study of Alburquerque Batholith at Tres Arroyos, Badajoz, Spain. *Journal of Petrology* **40**, 215-240.

75. Lottermoser B. G. (1992) Rare earth elements and hydrothermal ore processes. *Ore Geology Reviews* **7**, 25-41.

76. MacKenzie J. M. and Canil D. (1999) Composition and thermal evolution of cratonic mantle beneath the central Archean Slave Province, NWT, Canada. *Contrib. Mineral. Petrol.* **134**, 313-324.

77. Manning D. A. C. and Pichavant M. (1988) Volatiles and their bearing on the behaviour of metals in granitic systems. In *CIM Metallurgy* (eds. R. P. Taylor and D. F. Srong). pp. 13-24.

78. Masau M., Cerny P., and Chapman R. (2000) Dysprosian xenotime-(Y) from the Annie Claim granitic pegmatite, southeastern Manitoba, Canada; evidence of the tetrad effect? *The Canadian Mineralogist* **38**, 899-905.

79. Masuda A. (1962) Regularities in variation of relative abundances of lanthanide elements and an attempt to analyse separation index patterns of some minerals. *J. Earth Sci. Nagoya Uni.* **10**, 173-187.

80. Masuda A. and Akagi T. (1989) Lanthanide tetrad effect observed in leucogranites from China. *Geochem. J.* **23**, 245-253.

81. Masuda A. and Ikeuchi Y. (1979) Lanthanide tetrad effect observed in marine environment. *Geochem. J.* **13**, 19-22.

82. Masuda A., Kawakami O., Dohmoto Y., and Takenaka T. (1987) Lanthanide tetrad effects in nature: Two mutually opposite types, W and M. *Geochem. J.* **21**, 119-124.

83. McDonough W. F. and Frey F. A. (1989) Rare earth elements in upper mantle rocks. In *Geochemistry and mineralogy of rare earth elements* (eds. B. R. Lipin and G. A. McKay). Mineralogical Society of America, Washington, DC, United States, pp. 100-145.

84. McKay G., Wagstaff J., and Yang S. R. (1986) Clinopyroxene REE distribution coefficients for shergottites; the REE content of the Shergotty melt. In *Shergotty Consortium and SNC meteorites* Pergamon, Oxford, International, pp. 927-937.

85. McKay G. A. (1989) Partitioning of rare earth elements between major silicate minerals and basaltic melts. In *Reviews in Mineralogy: Geochemistry and mineralogy of rare earth elements* (eds. B. R. Lipin and G. A. McKay). The mineralogical society of America, Washington, D.C., pp. 44-78.

86. McKay G. (1986) Crystal/liquid partitioning of REE in basaltic systems; extreme fractionation of REE in olivine. *Geochimica et Cosmochimica Acta* **50**, 69-79.

87. McLennan S. M. (1999) Lanthanide series: rare earths. In *Encyclopedia of Geochemistry* (eds. C. P. Marshall and R. W. Fairbridge). Kluwer Academic, Dordrecht, pp. 211-213.

88. McLennan S. M. (1994) Rare earth element geochemistry and the “tetrad” effect. *Geochimica et Cosmochimica Acta* **58**, 2025-2033.

89. McLennan S. M., Lipin B. R., and McKay G. A. (1989) Rare earth elements in sedimentary rocks; influence of provenance and sedimentary processes. In *Geochemistry and mineralogy of rare earth elements.* (eds. Lipin-Bruce-R and McKay-G-A). Mineralogical Society of America, Washington, DC, United States, pp. 169-200.

90. Michard A., Michard G., Stueben D., Stoffers P., Cheminee J., and Binard N. (1993) Submarine thermal springs associated with young volcanoes; the Teahitia vents, Society Islands, Pacific Ocean. *Geochimica et Cosmochimica Acta* **57**, 4977-4986.

91. Miller C. F. and Mittlefehld D. (1982) Depletion of ligth rare earth elements in felsic magmas. *Geology* **10**, 129-133.

92. Mittlefehld D. and Miller C.F. (1983) Geochemistry of the Sweetwater Wash Pluton, California; implications for "anomalous" trace element behavior during differentiation of felsic magmas. *Geochimica et Cosmochimica Acta* **47**, 109-124.

93. Moeller P., Dulski P., Savascin Y., and Conrad M. (2004) Rare earth elements, yttrium and Pb isotope ratios in thermal spring and well waters of west Anatolia, Turkey; a hydrochemical study of their origin. *Chemical Geology* **206**, 97-118.

94. Moeller P. (2000) Rare earth elements and yttrium in aqueous crustal fluids. In *Geological Society of America, 2000 annual meeting* Geological Society of America (GSA), Boulder, CO, United States, p. 187.

95. Monecke T., Kempe U., Monecke J., Sala M., and Wolf D. (2002) Tetrad effect in rare earth element distribution patterns; a method of quantification with application to rock and mineral samples from granite-related rare metal deposits. *Geochimica et Cosmochimica Acta* **66**, 1185-1196.

96. Montel J. M. (1987) Comportement des terres rares dans les magmas leucogranitiques: modelisation et approche experimantale du role la manazite. Ph.D. Thesis, INPL, Nancy.

97. Montel J. (1986) Experimental determination of the solubility of Ce-monazite in SiO_2-Al_2O_3-K_2O-Na_2O melts at 800 ^oC, 2 kbar, under H_2O-saturated conditions. *Geology (Boulder)* **14**, 659-662.

98. Montel J. M., Watson E. B., Harrison T. M., Miller C. F., and Ryerson F. J. (1993) A model for monazite/ melt equilibrium and application to the generation of granitic magmas. *Chemical Geology* **110**, 127-146.

99. Morris R. V. and Haskin L. (1974) EPR measurement of the effect of glass composition on the oxidation states of europium. *Geochimica et Cosmochimica Acta* **38**, 1435-1445.

100. Nabelek P. I. and Glascock M. D. (1995) REE-depleted leucogranites, Black Hills, South Dakota; a consequence of disequilibrium melting of monazite-bearing schists. *Journal of Petrology* **36**, 1055-1071.

101. Neary C. R. and Highley D. E. (1984) The economic importance of the rare earth elements. In *Rare earth element geochemistry* (ed. P. Henderson). Elsevier Sci, Publ. Co.. Amsterdam, Netherlands, pp. 1-32.

102. Ni Y., Hughes J. M., and Marino A. N. (1995) Crystal chemistry of the monazite and xenotime structures. *American Mineralogist* **80**, 21-26.

103. Nielsen R., Gallahan W., and Newberger F. (1992) Experimentally determined mineral-melt partition coefficients for Sc, Y and REE for olivine, orthopyroxene, pigeonite, magnetite and ilmenite. *Contributions to Mineralogy and Petrology* **110**, 488-499.

104. Nowak M. and Behrens H. (1995) The speciation of water in haplogranitic glasses and melts determined by in situ near-infrared spectroscopy. Geochimica et Cosmochimica Acta 59, 3445-3450.

105. Oreskes N. and Einaudi M. (1990) Origin of rare earth element-enriched hematite breccias at the Olympic Dam Cu-U-Au-Ag deposit, Roxby Downs, South Australia. *Economic Geology* **85**, 1-28.

106. Pan Y. and Bau M. (1997) Controls on the fractionation of isovalent trace elements in magmatic and aqueous systems; evidence from Y/ Ho, Zr/ Hf, and lanthanide tetrad effect; discussion and reply. *Contributions to Mineralogy and Petrology* **128**, 405-408.

107. Pan Y. and Breaks F. (1997) Rare-earth elements in fluorapatite, Separation Lake area, Ontario; evidence for S-type granite-rare-element pegmatite linkage. *The Canadian Mineralogist* **35**, Part 3, 659-671.

108. Parrish R. (1990) U-Pb dating of monazite and its application to geological problems. *Canadian Journal of Earth Sciences* **27**, 1431-1450.

109. Peppard D. F., Mason G. W., and Lewey S. (1969) A tetrad effect in the liquid-liquid extraction ordering of lanthanide (III). *J. Inorg. Nucl. Chem* **31**, 339-343.

110. Philpotts J. and Schnetzler C. (1970) Phenocryst-matrix partition coefficients for K, Rb, Sr and Ba, with applications to anorthosite and basalt genesis. *Geochimica et Cosmochimica Acta* **34**, 307-322.

111. Pichavant M., Montel J., and Richard L. (1992) Apatite solubility in peraluminous liquids; experimental data and an extension of the Harrison-Watson model. *Geochimica et Cosmochimica Acta* **56**, 3588-3861.

112. Piepgras D. and Jacobsen S. (1992) The behavior of rare earth elements in seawater; precise determination of variations in the North Pacific water column. *Geochimica et Cosmochimica Acta* **56**, 1851-1862.

113. Plimer I. R., Lu J., and Kleeman J. D. (1991) Trace and rare earth elements in cassiterite; sources and components for the tin deposits of the Mole Granite, Australia. *Mineralium Deposita* **26**, 267-274.

114. Ponader C. W. and Brown G. E. (1989) Rare earth elements in silicate glass/melt systems: I. Effects of composition on the coordination environments of La, Gd, and Yb. *Geochimica et Cosmochimica Acta* **53**, 2893-2903.

115. Rapp R. and Watson E. B. (1986) Monazite solubility and dissolution kinetics; implications for the thorium and light rare earth chemistry of felsic magmas. *Contributions to Mineralogy and Petrology* **94**, 304-316.

116. Rapp R. P. et al. (1987) Experimental evidence bearing on the stability of monazite during crustal anatexis. In *Heat production in the continental lithosphere* American Geophysical Union, Washington, DC, United States, pp. 307-310.

117. Rapp R. P. and Watson E. B. (1985) Solubility and dissolution behavior of monazite and LREE diffusion in a hydrous granitic melt. In *AGU 1985 spring meeting* American Geophysical Union, Washington, DC, United States, p. 416.

118. Rietveld H. M. (1969) A Profile Refinement Method for Nuclear and Magnetic Structures. *Journal of Applied Crystallography* **2**, 65-71.

119. Ross J. and Aller L. (1976) The chemical composition of the Sun. *Science* **191**, 1223-1229.

120. Salters V. and Stracke A. (2004) Composition of the depleted mantle. *Geochemistry, Geophysics, Geosystems* **5**.

121. Salters V. and Longhi J. (1999) Trace element partitioning during the initial stages of melting beneath mid-ocean ridges. *Earth and Planetary Science Letters* **166**, 15-30.

122. Schaller T., Dingwell D., Keppler H., Knoeller W., Merwin L., and Sebald A. (1992) Fluorine in silicate glasses; a multinuclear nuclear magnetic resonance study. *Geochimica et Cosmochimica Acta* **56**, 701-707.

123. Seung-Gu L., Masuda A., and Hyung-Shik K. (1994) An early Proterozoic leuco-granitic gneiss with the REE tetrad phenomenon. *Chemical Geology* **114**, 59-67.

124. Seydoux G., Wirth R., Heinrich W., and Montel J. (2002) Experimental determination of thorium partitioning between monazite and xenotime using analytical electron microscopy and X-ray diffraction Rietveld analysis. *European Journal of Mineralogy* **14**, 869-878.

125. Shannon R. D. (1976) Revised effective ionic radii and systematic studies of interatomic distances in halides and chacogenides. *Acta Crystallogr. Sect. A.* **32**, 751-767.

126. Shen Y. and Forsyth D. W. (1995) Geochemical constraints on the initial and final depth of melting beneath mid-ocean ridges. *Journal of Geophysic Resources*. **100**, 2211-2237.

127. Shimizu N., Layne G. D., and Walter M. (1997) Trace-element partitioning in pigeonite-garnet-melt assemblages in natural peridotite composition at high pressures. In *Seventh*

annual V. M. Goldschmidt conference Lunar and Planetary Institute, Houston, TX, United States, pp. 191-192.

128. Siekierski S. (1971) The shape of lanthanide contraction as reflected in the changes of the unit cell volumes, lanthanide radius and the free energy of complex formation. *J. Inorg. Nucl. Chem.* **33**, 377-386.

129. Sowerby J. S. and Keppler H. (1999) Water speciation in rhyolitic melt determined by in-situ infrared spectroscopy. *American Mineralogist* **84**, 1843-1849.

130. Stolper E. (1982) Water in silicate glasses; an infrared spectroscopic study. *Contributions to Mineralogy and Petrology* **81**, 1-17.

131. Sun S. S. and McDonough W. F. (1989) Chemical and isotopic systematics of oceanic basalts; implications for mantle composition and processes. In *Magmatism in the ocean basins* (eds. A. D. Saunders and M. J. Norry). Geological Society of London, London, United Kingdom, pp. 313-345.

132. Takahashi Y., Amano K., Hama K., Mizuno T., Yoshida H., and Shimizu H. (2003) W- and M-type tetrad effects in REE patterns for water-rock systems in the Tono uranium deposit, central Japan; reply. *Chemical Geology* **202**, 185-189.

133. Takahashi Y., Yoshida H., Sato N., Hama K., Yusa Y., and Shimizu H. (2002) W- and M-type tetrad effects in REE patterns for water-rock systems in the Tono uranium deposit, central Japan. *Chemical Geology* **184**, 311-335.

134. Taura e. al., Taura e. al., and Taura e. al. (1998) Pressure dependence on partition coefficients for trace elements between olivine and the coexisting melts. *Phys. Chem. Minerals* **25**, 469-484.

135. Taylor M. and Ewing R. C. (1978) The crystal structures of ThSiO4 polymorphs: huttonite and thorite. *Acta Crystallogr.* **B**, 1074-1079.

136. Taylor S. R. and McLennan S. M. (1985) *The continental crust: Its composition and evolution*. Oxford: Blackwell scientific publications. 312 p.

137. Taylor S. R. et al. (1988) The significance of the rare earths in geochemistry and cosmochemistry. In *Handbook on the Physics and Chemistry of Rare Earths* (eds. Gschneidner-Karl-A Jr. and Eyring-LeRoy). Amsterdam, Netherlands, pp. 485-570.

138. Tuttle O. F. and Bowen N. L. (1958) Origin of granites in the light of experimental studies in the system $NaAlSi_3O_8$ - $KAlSi_3O_8$ - SiO_2 - H_2O. *Geological Society of America Memoir* **74**, 1-153.

139. Tuttle O. (1949) Two pressure vessels for silicate-water studies. *Geological Society of America Bulletin* **60**, 1727-1729.

140. Van Westrenen W., Allan N. L., Blundy J. D., Purton J. A., and Wood B. J. (2000) Atomistic simulation of trace element incorporation into garnets-comparison with experimental garnet-melt partitioning data. *Geochemica et Cosmochemica Acta* **64**, 1629-1639.

141. Veksler I. V., Dorfman A., Kamenetsky M., Dulski P., and Dingwell D. (2005) Partitioning of lanthanides and Y between immiscible silicate and fluoride melts, fluorite and cryolite

and the origin of the lanthanide tetrad effect in igneous rocks. *Geochimica et Cosmochimica Acta* **69**, 2847-2860.

142. Wang J. et al. (1994) A precise ^{232}Th- ^{208}Pb chronology of fine-grained monazite; age of the Bayan Obo REE-Fe-Nb ore deposit, China. In *The Clair C. Patterson special issue* (ed. T. M. Church). Pergamon, Oxford, International, pp. 3155-3169.

143. Wilson M. (1989) *Igneous petrogenesis*. Unwin Hyman, London.

144. Wolf M. and London D. (1995) Incongruent dissolution of REE- and Sr-rich apatite in peraluminous granitic liquids; differential apatite, monazite, and xenotime solubilities during anatexis. *American Mineralogist* **80**, 765-775.

145. Wood B. and Blundy J. (1997) A predictive model for rare earth element partitioning between clinopyroxene and anhydrous silicate melt. *Contributions to Mineralogy and Petrology* **129**, 166-181.

146. Wood B. J. and Blundy J. D. (2004) Trace element partitioning under crustal and uppermost mantle conditions: The influences of ionic radius, cation charge, pressure, and temperature. In *Treatise on geochemistry, Volume 2: The mantle and core* (ed. Richard W.Carlson). Elsevier Pergamon, pp. 395-424.

147. Wood B. and Blundy J. (2002) The effect of H_2O on crystal-melt partitioning of trace elements. *Geochimica et Cosmochimica Acta* **66**, 3647-3656.

148. Wu F. Y., Sun D. Y., Jahn B. M., and Wilde S. (2004) A Jurassic garnet-bearing granitic pluton from NE China showing tetrad REE patterns. *Journal of Asian Earth Sciences* **23**, 731-744.

149. Yurimoto H., Duke E., Papike J., and Shearer C. (1990) Are discontinuous chondrite-normalized REE patterns in pegmatitic granite systems the results of monazite fractionation? *Geochimica et Cosmochimica Acta* **54**, 2141-2145.

150. Zhao J. and Cooper J. (1992) The Atnarpa igneous complex, Southeast Arunta Inlier, central Australia; implications for subduction at an early-mid Proterozoic continental margin. *Precambrian Research* **56**, 227-253.

151. Zhao Z. H., Xiong X. L., and Han X. D. (1999) The formation mechanism of REE tetrad in granites. Sci. China, Ser. D: Earth Sci 29, 331-338.

152. Zhao Z., Masuda A., and Shabani M. (1992) Tetrad effects of rare-earth elements in rare-metal granites. *Diqiu Huaxue* **1992**, 221-233.

153. Zhao Z., Masuda A., and Shabani M. (1993) REE tetrad effects in rare-metal granites. *Chinese Journal of Geochemistry* **12**, 206-219.

154. Zhu X., Nions R., Belshaw N., and Gibb A. (1997) Significance of in situ SIMS chronometry of zoned monazite from the Lewisian granulites, Northwest Scotland. *Chemical Geology* **135**, 35-53.

155. Zhu X. K. and O'Nions R. K. (1999) Monazite chemical composition: Some implications for monazite geochronology. *Contributions to Mineralogy and Petrology* **137**, 351-363.

Part II: Solubility of tin in (Cl, F)-bearing aqueous fluids at 700 °C, 140 MPa: a LA-ICP-MS study on synthetic fluid inclusions

II- 1. Introduction

More than 95% of the world's Sn-production comes from ore deposits that are directly or indirectly related to granitic rocks, with cassiterite (SnO_2) being the main ore mineral (Lehmann, 1990). Primary tin mineralization occurs in veins, breccias, replacement bodies and quartz-muscovite-topaz greisens in the roof regions of highly evolved biotite and/or muscovite granites and leucogranites. These granites are characterized by a shallow level of emplacement (≤ 3-4 km), are markedly peraluminous (ASI ≥ 1.1), reduced ("ilmenite-series"), and enriched in fluorine and other incompatible trace elements such as Li, B, Cs, Rb and Sn (e.g., Tischendorf, 1977; Lehmann, 1990; Baumann et al., 2000). Numerous studies have shown that tin ore formation results from a sequence of processes that involves: (i) melt generation at depth, (ii) magma ascent, fractional crystallization, assimilation and magma mixing (iii) emplacement of evolved, residual magma in a shallow magma chamber (iv) magma solidification, further melt fractionation, and exsolution of aqueous fluids, (v) transport and focusing of magmatic fluids into local structures, and (vi) precipitation of dissolved Sn in response to fluid – rock interaction, cooling, fluid depressurization and/or fluid mixing. Although this general sequence is well established, some mechanisms are still poorly understood. For example, it is not clear whether the close association of F and Sn is accidental, or whether fluorine actually played an active role in the process of Sn-enrichment. Experimental studies on the solubility of Sn in hydrothermal fluids are focused mostly on chlorine-bearing systems at temperatures ≤ 500 °C (e.g., Klintsova and Barsukov, 1973; Klintsova et al., 1975; Nekrasov and Ladze, 1973; Kovalenko et al., 1986, 1986), with spare data being available for higher temperatures (e.g., Wilson and Eugster, 1990; Taylor and Wall, 1993). The scarcity of high-temperature data is partly explained by the tendency of Sn to alloy with noble metals (e.g., Nekrasov et al., 1980; Keppler and Wyllie, 1991), which may lead to disequilibria in the experimental charge. Furthermore, because Sn-solubilities traditionally were determined in quench solutions at ambient conditions, it is possible that true solubilities were underestimated due to precipitation of originally dissolved Sn during the quench.

Here we followed a different approach by trapping small portions of fluid at high pressure and temperature in the form of synthetic fluid inclusions in quartz, and subsequently analyzing individual inclusions by Laser-Ablation Inductively-Coupled-Plasma Mass-Spectrometry (e.g., Loucks and Mavrogenes, 1999). Two different methods for fluid inclusion synthesis were used: (i) a new technique that we call "etched plate technique", and (ii) the in-situ cracking technique (e.g., Sterner, 1992). The former technique has the advantage that it produces relatively large inclusions, and – if used in combination with fine-grained starting material – allows entrapment of fluid that for a considerable amount of time was not in contact with the capsule walls, avoiding potential disequilibria caused by alloying. The in-situ cracking method produces much smaller inclusions and does not circumvent problems caused by alloying. However, it has the advantage that fluid inclusion formation can be initiated after some time of pre-equilibration, which is crucial in cases where fluid inclusion formation is fast relative to the time required to reach equilibrium in the fluid. Because fluid inclusions produced by both techniques subsequently are analyzed as a whole, any material that precipitates within the inclusions during cooling is included in the analysis.

II- 2. Methods

II- 2.1. Inclusion synthesis by the etched plate technique

Oriented quartz laths measuring ca. 1 x 2 x 10 mm were cut from an inclusion-free quartz crystal in such a way that their longest dimension was parallel to the c-axis of the crystal. By using a rough rock saw for cutting, numerous small cracks were generated along the sample surface. The quartz pieces where then etched in 30-40% HF for 1-2 hours to produce a network of small channels on the surface. Subsequently, fine cassiterite powder of 20-60 µm grain size (prepared from a natural cassiterite crystal from Viloco, Bolivia) was sprinkled over the quartz surface, such that individual cassiterite fragments fell into the etch channels. Three or four so-prepared quartz laths were sealed together with silica glass (0.2-0.3 g), some larger cassiterite grains (0.014-0.015 g; to assure cassiterite saturation during the run) and 65-90 µl aqueous solution into gold capsules of 35 mm length, 5.0 mm outer diameter (O.D.) and 4.6 mm inner diameter (I.D.). Starting solutions were prepared from doubly distilled water and reagent-grade NaCl (5-35 wt.%), NaF (5-35 wt.%), HCl (0.5-4.4 m) or HF (0.5-3.2 m). The HCl and HF-bearing solutions were spiked with 304-487 ppm each of Rb, Cs and Ba (added as RbCl, CsCl and $BaCl_2{\cdot}2H_2O$, respectively) for internal standardization of the LA-ICP-MS analyses. After loading, the capsules were sealed by arc welding, re-weighed, and left at 150 °C overnight. Only capsules that had lost less than 2 % weight during this procedure were used for the experiments.

Experiments were conducted in cold-seal pressure vessels of 39 mm outer diameter, 7 mm inner diameter, and 235 mm length, using water as pressure medium. The samples were first pressurized to 100 MPa, then isobarically heated to 400 °C, and subsequently isochorically heated up to the experimental conditions of 140 MPa and 700 °C. Temperatures were measured with NiCr-Ni thermocouples that were placed either inside the bomb or in a well at the end of the bomb, giving an overall uncertainty of ± 15 °C. Pressures were measured on a Heise gauge calibrated to an uncertainty of 10 MPa. Oxygen fugacity was intrinsically buffered near the nickel – nickel oxide buffer (NNO) by the reaction of the pressure medium (water) with the Ni-rich alloy of the pressure vessel and a nickel filler rod. Experiments lasted for 4-5 days, after which the cold-seal vessels were quenched isochorically by air cooling. Recovered capsules were cleaned, dried overnight at 150 °C, and re-weighed to check for leaks during the run. Most capsules gained a small amount of weight ($\leq$ 0.3wt.%) during the run, probably due to uptake of nickel. Two capsules (*NaCl5* and *NaCl10*) were visibly broken after the experiment, and two more capsules (*NaCl25, NaF15*) lost several percent of the mass of the loaded solution. However, at least in the former case the capsules must have ruptured during quenching, as the contained quartz crystals did not show any signs of dissolution. For this reason, these samples nevertheless were analyzed.

During the experiments, dissolution of silica glass and re-precipitation of dissolved silica onto the etched quartz laths lead to the entrapment of numerous cassiterite grains and fluid inclusions Figure II- 2.1). The shape and distribution of the fluid inclusions suggest that most of them did not form individually, but rather evolved from larger, irregular inclusions by necking down. Hence, in cases where a cassiterite grain was present in one of these early inclusions, any secondary inclusion evolving from it trapped fluid that for a certain amount of time was in contact with cassiterite and quartz only, without having access to the gold capsule. Identification of such secondary, "equilibrium-type" inclusions after the run is possible only if the inclusion necked down only recently, because in this case former connections to cassiterite-bearing mother inclusions still can be inferred from the inclusion shapes. If available, such "equilibrium type" inclusions were the main targets for LA-ICP-MS analysis. However, in order to check whether the uptake of Sn by the gold capsule caused any disequilibrium effects in the bulk fluid we also analyzed "normal" inclusions that did not neck-down from larger, cassiterite-bearing inclusions.

II- 2.2. Inclusion synthesis by the in-situ cracking technique

Two runs with a 3.14 m HF solution and a 4 m HCl solution were performed in rapid-quench pressure vessels in which the samples are held in the top part of the bombs by a 25 cm long holder which itself can be moved from outside by means of a magnet. Pressure medium was again water. After one week of pre-equilibration at 700 °C / 140 MPa, the samples were pulled within one second to the cold end of the vessel and subsequently back to the hot end, where they were kept for another three days. The thermal shocking produced numerous small cracks in the quartz cores, which partly healed during the subsequent three days, thereby trapping small amounts of fluid (Figure II- 2.2). In the run with the 3.14 m HF solution, a previously uncracked quartz core of 4 mm diameter and 8 mm length was sealed together with 17 mg of solution (spiked with 851 ppm each of Rb and Cs) and 25 mg of cassiterite powder (60-160 μm grain size) into a gold capsule of 5 mm O.D., 4.6 mm I.D. and 13 mm length. To ensure an external oxygen fugacity close to NNO, a smaller gold capsule of 5 mm O.D., 4.6 mm I.D and 7 mm length was filled with Ni-powder, crimped, and placed immediately below the main capsule.

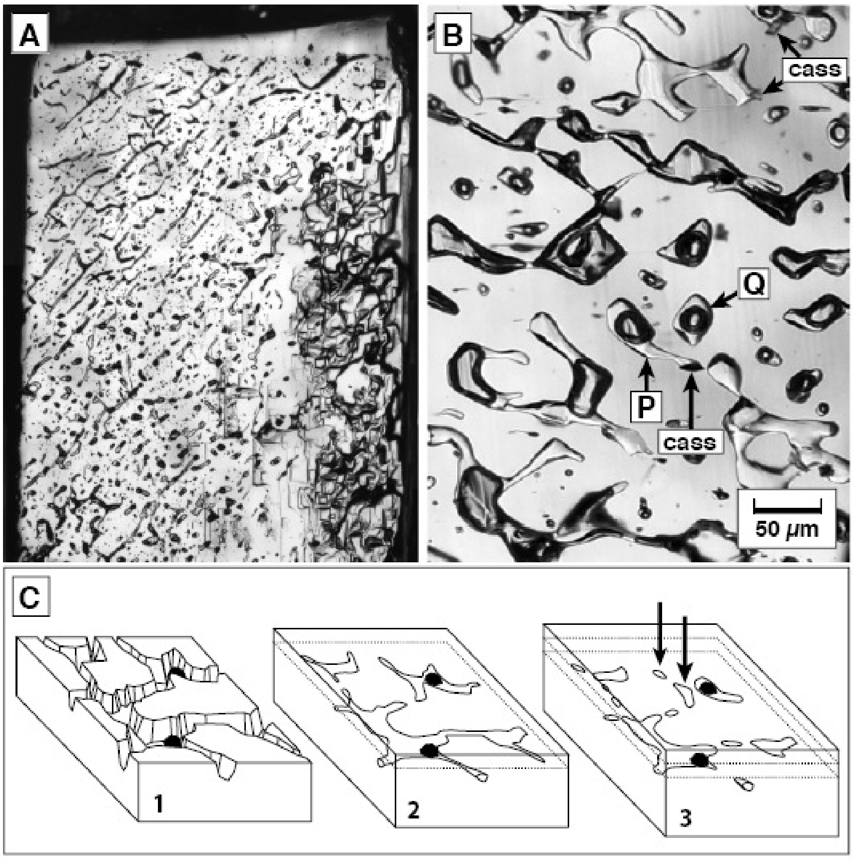

Figure II- 2.1. *Fluid inclusions grown by the etched plate technique. (A) Photograph of a polished quartz plate after 5 days residence in a 25 wt.% NaCl solution at 700 °C / 140 MPa (transmitted light). Overgrowth of new quartz led to the entrapment of numerous fluid inclusions and cassiterite grains in etch channels along the former quartz surface. (B) Close view of a sample synthesized in a 15 wt.% NaCl solution. Most fluid inclusions are still in the process of necking down, trying to reduce their surface-to-volume ratio. Inclusion P, for example, still is connected by a small neck to a cassiterite grain ("cass"). If the run had been taken down one day later, this inclusion would have become separated from the cassiterite grain, an therefore would have isolated fluid that for a considerable amount of time was in equilibrium with quartz and cassiterite only, without having access to the capsule wall. Inclusion Q probably once was connected to the same cassiterite grain, too, and therefore likely represents such an "equilibrium-type" inclusion. (C) Cartoon showing the mechanism of fluid entrapment and subsequent re-organization of large, irregular inclusions into several smaller inclusions of lower surface energy. Two "equilibrium-type" inclusions that formed by necking down from a cassiterite-bearing inclusion are marked by arrows*

In the run with the 4 m HCl solution, a double capsule technique was employed to speed up hydrogen transfer and concomitant cassiterite dissolution (see below). For this purpose, 15 mg each of Ni and NiO powder were sealed together with 12 mg of H_2O into a platinum capsule of 3.0 mm O.D., 2.7 mm I.D. and 14 mm length. This capsule was sealed together with an uncracked quartz core, 30 mg of solution (spiked with 603 ppm each of Rb and Cs) and cassiterite powder (60-160 µm grain size) into a gold capsule of 5.0 mm O.D., 4.6 mm I.D., and 20 mm length. No external, Ni-filled Au-capsule was used in this case.

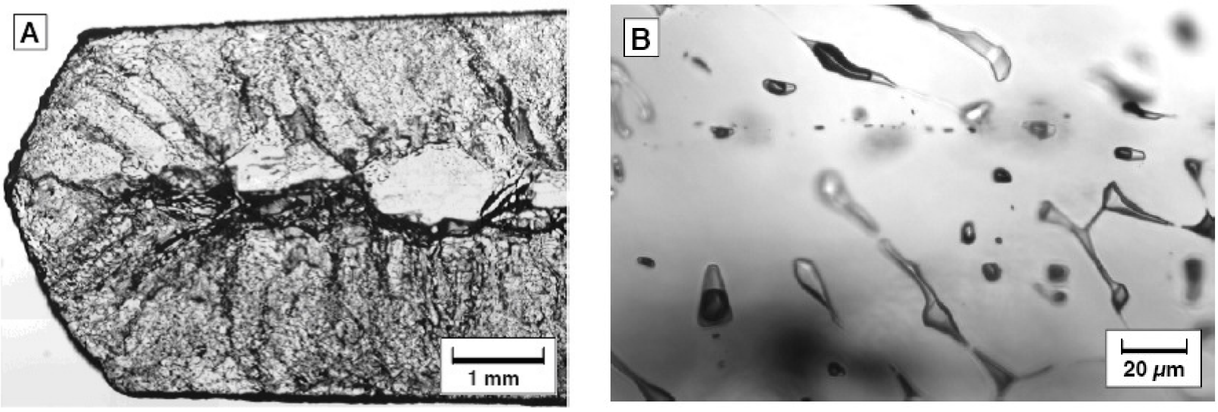

Figure II- 2.2. *Fluid inclusions grown by the in-situ cracking technique. (A) After one week of pre-equilibration, isobaric quenching from 700 °C to 20 °C and immediate re-heating to 700 °C lead to the development of numerous small cracks in the quartz core. The cracks partly healed out in the days following the in-situ cracking (transmitted light). (B) Close view of a portion of the sample shown in A. Note the small size of the fluid inclusions compared to those produced by the etched plate technique (transmitted light).*

II- 2.3. Analytical methods

Five to ten inclusions of each run were analyzed by LA-ICP-MS in the Laboratory of Analytical Chemistry at ETH Zürich and at the Bayerisches Geoinstitut for the isotopes ^{23}Na, ^{29}Si, ^{85}Rb, ^{118}Sn, ^{120}Sn, ^{133}Cs, and ^{137}Ba. The utilized LA-ICP-MS systems consisted of an Elan 6100 or Elan DRC-e quadrupole mass spectrometer (Perkin Elmer Instruments) attached to a Geolas M 193nm ArF Excimer Laser system (Coherent / Lambda Physik). Technical details concerning these systems and their operation can be found in Günther et al. (1997, 1998). Individual inclusions were ablated through the host quartz in several steps, using laser beam sizes ranging from 4 to 60 µm in diameter. The laser was operated at a frequency of 10 Hz and a power of 25 kV. The sample chamber was flushed with helium gas at a rate of 1 l/min, to which Ar was added on the way to the ICP-MS. Signals were recorded with 5 sweeps per second, and instrument background was measured for 30 seconds before each analysis. Integrated signal intensities were referenced to NIST SRM 610 glass according to routines described in Longerich et al. (1996). Calculated element ratios were then turned into absolute values using Na as internal standard in NaCl and NaF-bearing runs, and using Rb or Cs as internal standard in HCl and HF-bearing runs. Switching between Rb or Cs as internal standards had no measurable effect on the calculated mean Sn-content of a given inclusion population. Barium could not be used as an internal standard because it usually was below detection limit. Within the analytical precision of ca. 10% relative, Sn concentrations calculated on the basis of ^{118}Sn are identical to those obtained from ^{120}Sn, implying that no interference problems occurred on these isotopes.

Internal standardization in the NaF-bearing experiments is complicated by the formation of a separate melt phase, as demonstrated by the presence of coexisting melt and fluid inclusions in the recovered samples (Figure II- 2.3). Hence, the starting Na concentration of the bulk fluid could no longer be used as an internal standard. The Na content of the melt phase was, therefore, estimated on the basis of phase equilibria constraints and Na : Si : Sn-ratios obtained from LA-ICP-MS analysis of rapidly quenched, exposed melt inclusions (see below). The Na content of the coexisting fluid phase was determined microthermometrically based on the ice-melting curve in the system H_2O-NaF (Kovalenko, pers. commun., 1988).

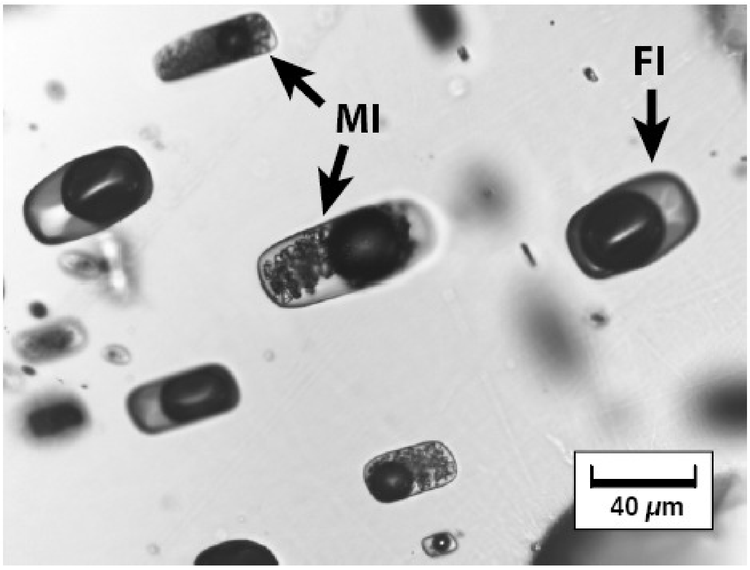

Figure II- 2.3. *Coexisting melt inclusions (MI) and fluid inclusions (FI) in a sample synthesized in a 10 wt.% NaF solution. The melt inclusions unmixed into glass, fluid and villaumite crystals during the cooling at the end of the experiment (transmitted light photomicrograph).*

II- 3. Results

Compositions of individual fluid inclusions are listed in Table II- 3.1 and Table II- 3.2, and are summarized in Figure II- 3.1. Tin concentrations generally increase with increasing Cl and F concentration in the fluid, regardless of whether Cl and F were added in the form of salts or acids. However, Sn solubilites are about two orders of magnitude higher in HCl-bearing fluids than in NaCl-bearing fluids of the same chlorine content (0.8 - 11 wt.% vs. 100-800 ppm). Since the fluid in the NaF-bearing runs was buffered by the coexisting melt phase at a constant concentration of 0.5 wt.% NaF, only one point can be shown for this series.

Considering the fact that none of the fluid inclusions produced in this study contain any daughter crystals, Sn contents of up to 11 wt.% in the HCl-bearing fluid inclusions may appear surprisingly high. To demonstrate that these high Sn contents are real we subjected fluid inclusion from sample *HCl4* in a subsequent experiment to high oxygen fugacities, with the idea that the cassiterite dissolution reaction (which involves reduction of tetravalent Sn to divalent tin; see below) will be reversed, and that dissolved divalent Sn will re-precipitate in the form of cassiterite within the inclusions. Mavrogenes and Bodnar (1994) showed that hydrogen diffusion through quartz at temperatures of ≥600 °C is fast enough to allow small fluid inclusions near the quartz surface to equilibrate to the surrounding f_{H2} within a matter of hours to a few days. Two pieces of sample *HCl4* were therefore sealed together with a small amount of water, silicate glass and hematite into a small gold capsule, which itself was sealed together with water, silicate glass and hematite into a larger gold capsule. The double-capsule was then held for five days at 670 °C / 129 MPa in a cold-seal pressure vessel pressurized with Ar (log fO_2 ~ NNO + 2). After this experiment, small fluid inclusions near the quartz surface indeed contained relatively large cassiterite daughter crystals (Figure II- 3.2), substantiating the Sn concentrations of 2.5-3.9 wt.% measured in identical inclusions by LA-ICP-MS.

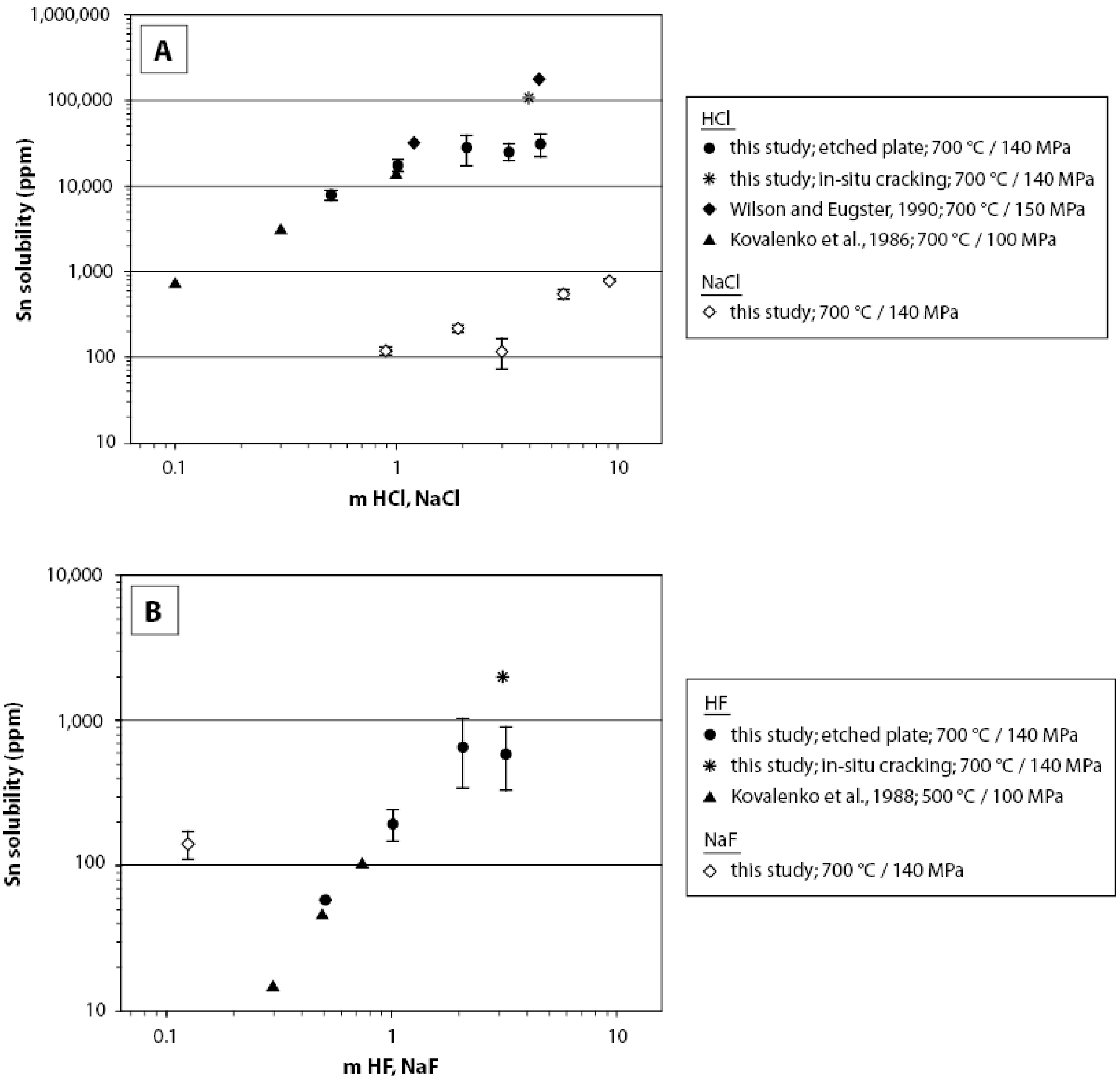

Figure II- 3.1.*Summary of Sn-solubilities measured by LA-ICP-MS analysis of synthetic fluid inclusions grown at 700 °C / 140 MPa. (A) HCl vs. NaCl-bearing fluids; (B) HF vs. NaF-bearing fluids. Results from previous studies conducted at similar P/T -conditions are shown for comparison. In all studies, fO_2 was buffered near NNO.*

Table II- 3.1. *LA-ICP-MS analyses of individual fluid inclusions produced by the etched plate technique*

Inclusion	a)	NaCl (wt.%)	**Na**	^{118}Sn	^{120}Sn
NaCl5-47	N	5	19650	105	102
NaCl5-48	N	5	19650	129	146
NaCl5-49	N	5	19650	102	103
NaCl5-50	N	5	19650	80	81
NaCl10-36	E	10	39300	235	226
NaCl10-37	E	10	39300	220	214
NaCl10-39	E	10	39300	211	215
NaCl10-40	N	10	39300	218	233
NaCl10-41	N	10	39300	236	232
NaCl10-42	E	10	39300	193	197
NaCl10-43	N	10	39300	227	236
NaCl10-44	N	10	39300	221	214
NaCl15-24	E	15	58950	71	75
NaCl15-25	E	15	58950	113	111
NaCl15-27	E	15	58950	107	106
NaCl15-29	N	15	58950	106	147
NaCl15-30	N	15	58950	163	171
NaCl15-31	N	15	58950	147	141
NaCl15-33	N	15	58950	83	83
NaCl15-34	N	15	58950	76	74
NaCl25-12	E	25	98349	524	539
NaCl25-14	E	25	98349	564	569
NaCl25-15	E	25	98349	560	555
NaCl25-16	E	25	98349	552	549
NaCl25-17	E	25	98349	550	583
NaCl25-19	N	25	98349	598	612
NaCl25-20	N	25	98349	463	480
NaCl25-21	N	25	98349	516	511
NaCl25-22	N	25	98349	484	499
NaCl25-23	N	25	98349	544	583
NaCl35-5	E	35	137550	740	698
NaCl35-6	E	35	137550	743	757
NaCl35-7	E	35	137550	797	804
NaCl35-9	N	35	137550	778	778
NaCl35-10	N	35	137550	808	830

Inclusion	a)	HCl (m)	**Rb**	^{118}Sn	^{120}Sn	Cs
HCl0.5-31	N	0.50	472	7698	7597	534
HCl0.5-32	N	0.50	472	8145	8482	618
HCl0.5-27	N	0.50	472	6542	6346	474
HCl0.5-28	N	0.50	472	6938	7258	434
HCl0.5-29	N	0.50	472	8236	8142	464
HCl0.5-30	N	0.50	472	8299	8379	497
HCl1-21	N	1.02	444	17135	17032	453
HCl1-22	N	1.02	444	19697	19277	469
HCl1-23	N	1.02	444	19583	19756	449
HCl1-24	N	1.02	444	19915	20247	445
HCl1-26	N	1.02	444	14276	14266	447
HCl2-19	N	2.09	390	35049	34737	419
HCl2-20	N	2.09	390	17859	17251	388
HCl2-15	N	2.09	390	38058	38040	375
HCl2-16	N	2.09	390	22276	22540	391
HCl2-17	N	2.09	390	37170	37780	416
HCl2-18	N	2.09	390	16869	16668	397
HCl3-8	E	3.20	337	27424	28100	337
HCl3-9	N	3.20	337	26271	26130	345
HCl3-10	E	3.20	337	19457	19316	353
HCl3-12	N	3.20	337	22807	23135	323
HCl3-13	N	3.20	337	29639	28942	381
HCl3-14	N	3.20	337	26336	29438	371
HCl4-3	N	4.36	286	24818	24600	291
HCl4-4	N	4.36	286	27225	27371	309
HCl4-5	N	4.36	286	29219	28604	297
HCl4-6†	N	4.36	286	21408	21159	318
HCl4-7	N	4.36	286	30496	30223	339
HCl4-1	N	4.36	286	39485	38691	317
HCl4-2	N	4.36	286	39137	38978	301

Inclusion	a)	HF (m)	**Rb**	^{118}Sn	^{120}Sn	Cs
HF0.5-11	N	0.51	487	(304)	(238)	463
HF0.5-12	N	0.51	487	(241)	(201)	495
HF0.5-13	N	0.51	487	59	72	493
HF0.5-14	E	0.51	487	(426)	(366)	559
HF0.5-15	E	0.51	487	(246)	(190)	530
HF0.5-16	E	0.51	487	(271)	(226)	513
HF0.5-17	E	0.51	487	(204)	(174)	583
HF1-4	E	1.02	474	199	198	523
HF1-5	E	1.02	474	237	247	519
HF1-6	E	1.02	474	(567)	(501)	483
HF1-7	E	1.02	474	(425)	(346)	529
HF1-8	N	1.02	474	231	213	477
HF1-9	N	1.02	474	(270)	(207)	474
HF1-10†	N	1.02	474	144	144	460
HF2-34	N	2.09	449	336	317	465
HF2-35	N	2.09	449	470	482	471
HF2-36	N	2.09	449	474	488	450
HF2-37	N	2.09	449	562	572	523
HF2-38	N	2.09	449	538	599	487
HF2-39	N	2.09	449	616	611	457
HF2-40	N	2.09	449	509	680	640
HF2-1	E	2.09	449	436	408	462
HF2-2	E	2.09	449	1008	1052	213
HF3-8	E	3.19	423	455	434	478
HF3-9	N	3.19	423	356	424	386
HF3-10	E	3.19	423	449	444	449
HF3-11	N	3.19	423	884	863	733
HF3-12	N	3.19	423	323	353	446
HF3-13	N	3.19	423	745	730	439
HF3-14	N	3.19	423	466	474	452

All values in ppm; values in parantheses represent detection limits in cases where no signal was obtained.
Tin-concentrations were calculated based on two different isotopes, ^{118}Sn and ^{120}Sn

Table II- 3.2. *LA-ICP-MS analyses of individual fluid inclusions produced by the in-situ cracking technique*

Inclusion	HCl (m)	**Cs**	^{118}Sn	Rb	Inclusion	HF (m)	**Cs**	^{118}Sn	Rb
HCl4-I-1	4	603	101112	578	HF3-I-1	3.14	851	2066	1020
HCl4-I-3	4	603	99204	460	HF3-I-2	3.14	851	1771	919
HCl4-I-4	4	603	120873	553	HF3-I-3	3.14	851	2209	836
HCl4-I-5	4	603	103671	789	HF3-I-4	3.14	851	1802	1000
HCl4-I-6	4	603	117376	484	HF3-I-5	3.14	851	1726	840
HCl4-I-7	4	603	118042	656	HF3-I-6	3.14	851	1738	918
HCl4-I-8	4	603	127563	483	HF3-I-7	3.14	851	1933	1019
HCl4-I-10	4	603	117175	540	HF3-I-8	3.14	851	2049	770
HCl4-I-11	4	603	113780	572	HF3-I-9	3.14	851	2094	940
HCl4-I-12	4	603	101791	704	HF3-I-11	3.14	851	1823	904
					HF3-I-12	3.14	851	2296	934
					HF3-I-13	3.14	851	2100	971

All values in ppm; Tin-concentrations were calculated based on ^{118}Sn

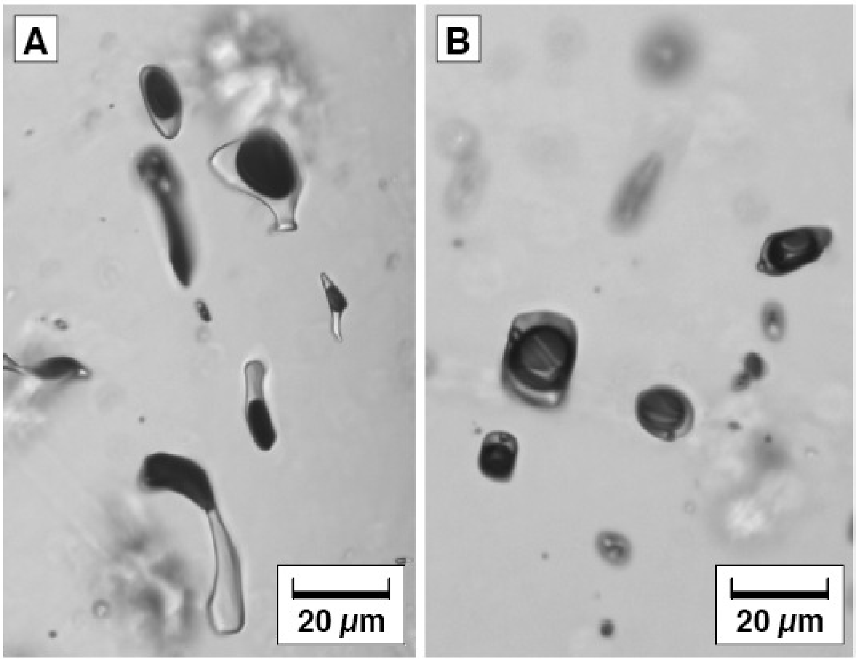

Figure II- 3.2. *Fluid inclusions synthesized in a 4m HCl-solution. Typical views (A) before, and (B) after diffusive re-equilibration at 670 °C / 130 MPa and a high (but unknown) oxygen fugacity. After equilibration, each inclusion contains a relatively large daughter crystal of cassiterite (identified by Raman spectroscopy), in agreement with Sn contents of 2.5-3.9 wt.% determined by LA-ICP-MS (transmitted light photomicrographs).*

Tin contents of fluid inclusions from the NaCl-series are well reproducible and lie on a well-defined trend, except for run *NaCl15* that shows anomalously low values and a large scatter (Figure II- 3.1; Figure II- 3.3a). The good reproducibility observed in the other NaCl-bearing runs implies that in these cases the fluid reached equilibrium with regard to Sn-solubility before it became trapped in the fluid inclusions. In run *NaCl15*, however, fluid inclusion formation apparently was too fast (probably due to an anomalously large thermal gradient across the sample), leading to entrapment of fluid that had not yet reached equilibrium. The fact that no systematic differences between "equilibrium type" and "normal" inclusions can be observed in runs *NaCl5*, *NaCl10*, *NaCl25* and *NaCl35* (Figure II- 3.3a, Table II- 3.1) suggests that the alloying of Sn with the gold capsule had no measurable effect on the equilibrium Sn concentration in the fluid.

Tin contents of HCl and HF-bearing fluid inclusions synthesized by the etched plate technique are relatively reproducible at low acid concentrations, but show a large scatter at high acid concentrations (Figure II- 3.1; Figure II- 3.3b-d). This scatter is unlikely to reflect an analytical uncertainty because the acid-rich inclusions contain more Sn than the acid-poor inclusions, hence they can be analyzed with higher precision. In view of the observations made in the NaCl-bearing experiments it seems more likely that the large scatter in the concentrated HCl and HF-solutions is caused by the same problem as the one encountered in run *NaCl15*, i.e., by entrapment of fluid that had not yet reached equilibrium with respect to Sn solubility. This failed equilibrium could be result of several factors. In the HCl-rich runs, the limiting factor may have been the diffusion rate of H_2 through the gold capsule, as large amounts of H_2 are required for the reduction of SnO_2 to achieve solubilities of up to 11 wt.% Sn in the fluid. In the HF-bearing runs the required amount of H_2 was much smaller, but fluid inclusion formation may have been extraordinarily fast due to the high quartz solubility in HF-bearing fluids.

To test this hypothesis we performed two additional experiments using the in-situ cracking technique. Resulting Sn solubilites are significantly higher than those obtained by the etched plate experiments, are better reproducible (despite much smaller inclusion sizes), and are in good agreement with solubility data of previous workers and trends displayed by the etched plate experiments performed at low acid concentrations (Figure II- 3.1), supporting the suspicion that the etched plate experiments in concentrated HCl and HF solutions failed to trap equilibrium fluid.

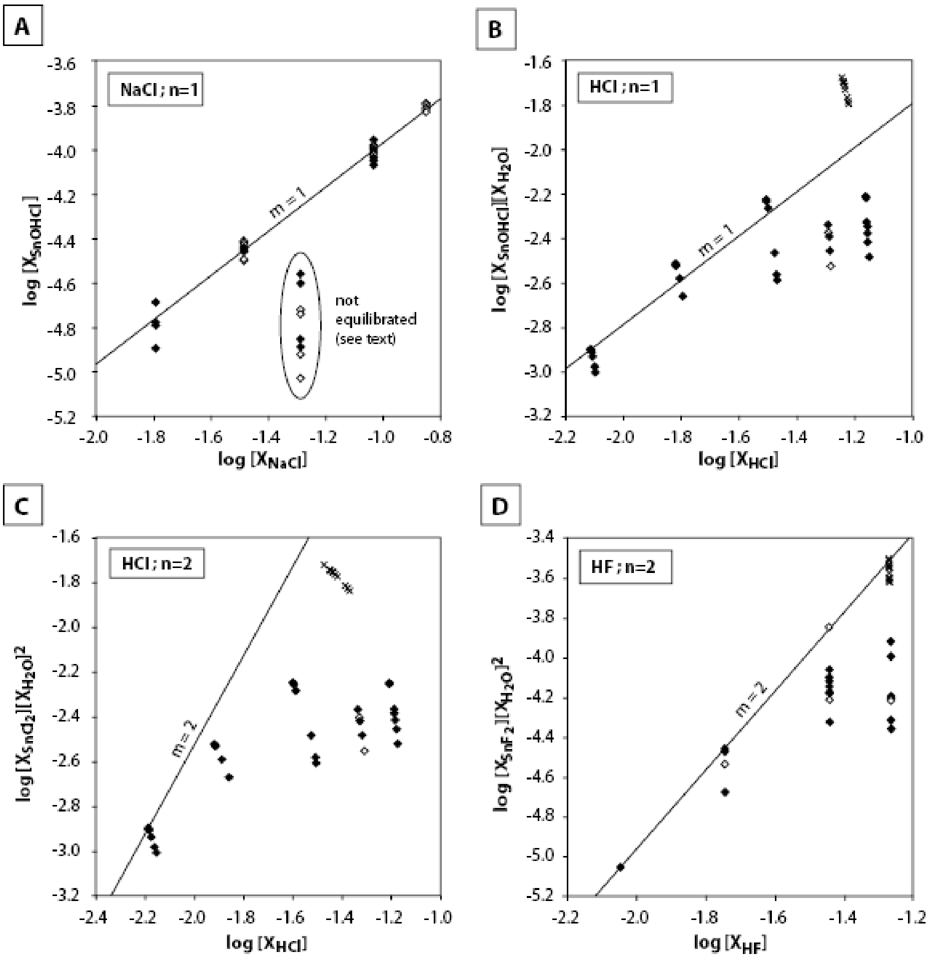

Figure II- 3.3. *Tin content of individual fluid inclusions plotted against ligand concentration (all concentrations expressed as mole fractions). The graphs allow testing for the cassiterite dissolution reactions 1, 2, 5 and 6 as explained in the text. Each data point represents a single fluid inclusion analysis, with full symbols denoting "normal inclusions", and empty symbols denoting "equilibrium-type" inclusions.*

Information on potential Sn-complexes in the fluid was obtained by procedures similar to the ones discussed in Wilson and Eugster (1990). The atomic ratio of metal ion to complexing anion can be estimated graphically from a set of solubility data in which the ligand concentration is the only variable. If the log of the measured Sn concentrations is plotted against the log of the corresponding ligand concentrations, the slope of interpolating lines yields the ligand/Sn-ratio of the dominant species in the fluid. Potential dissolution reactions were written on the assumption that at the oxygen fugacities near the Ni-NiO buffer all Sn is dissolved in the divalent state (e.g., Kovalenko et al., 1986; Wilson and Eugster, 1990) and those only neutral charges species occur in the fluid (e.g., Eugster and Baumgartner, 1987). In a first attempt, only ligand numbers of 1 or 2 are considered.

Two potential reactions in the HCl-bearing runs are:

$$SnO_2 + HCl + H_2 \Leftrightarrow Sn(OH)Cl + H_2O \qquad \textbf{(Eq. II-3.1)}$$

$$SnO_2 + 2HCl + H_2 \Leftrightarrow SnCl_2 + 2H_2O \qquad \textbf{(Eq.II- 3.2)}$$

The equilibrium equation of reaction 2 (Eq.II-5.2), for example, is:

$$K = \frac{[SnCl_2][H_2O]^2}{[SnO_2][HCl]^2 f_{H_2}} \qquad \textbf{(Eq.II- 3.3)}$$

Since the activity of SnO_2 (a pure phase) by definition is unity, this can be transformed into:

$$\log\left([SnCl_2][H_2O]^2\right) = 2 \cdot \log[HCl] + \log\left(f_{H_2} \cdot K\right) \qquad \textbf{(Eq.II- 3.4)}$$

If cassiterite was dissolving in all our HCl-bearing experiments according to reaction 2 (Eq.II-5.2), measured solubilites should plot in a graph of $\log\left([SnCl_2][H_2O]^2\right)$ vs. $\log[HCl]$ on a straight line with a slope of +2. However, if it was dissolving according to reaction 1 (Eq.II-5.1), measured Sn solubilites should plot, in a graph of log $\log\left([Sn(OH)Cl][H_2O]\right)$ vs. $\log[HCl]$, on a line with a slope of +1. In applying this principle, it does not matter which concentration unit is used, as the absolute value of K has no influence on the slope of the line. For the HF- and NaCl-bearing experiments the following reactions were investigated:

$$SnO_2 + 2HF + H_2 \Leftrightarrow SnF_2 + 2H_2O \qquad \textbf{(Eq.II- 3.5)}$$

$$SnO_2 + NaCl + H_2 \Leftrightarrow Sn(OH)Cl + NaOH \qquad \textbf{(Eq.II- 3.6)}$$

Following the work of Ellis (1963), Aranovich and Newton (1996), Tagirov et al. (1997), Pokrovskii (1999), and Newton and Manning (2000) it was assumed that HCl, NaCl and HF were fully associated in our experiments. Equilibrium concentrations of HCl, NaCl and HF were corrected for the amounts of Cl and F incorporated in the Sn-complexes. This correction had a significant effect only for the HCl-bearing runs and is responsible to the nonlinear data arrays in Figure II- 3.3-b, -c. For reaction 6 (Eq.II-5.6), it was further assumed that the concentration of NaOH was independent of Sn-solubility, as it is governed by the reaction $NaCl + H_2O \Leftrightarrow NaOH + HCl$.

II- 4. Discussion

A rigorous comparison of our solubility data with earlier work is possible only for the HCl-bearing experiments because most previous studies were either performed at lower temperatures (e.g., Klintsova and Barsukov, 1973; Kovalenko et al., 1986, 1988) or with more complex fluids (Taylor and Wall, 1993). Results from our 0.5 and 1.0 m HCl etched plate experiments and the 4 m HCl in-situ cracking experiments fit well onto a trend defined by three measurements at 700 °C / 100 MPa by Kovalenko et al. (1986) and two measurements at 700 °C / 150 MPa by Wilson and Eugster (1990). As discussed above, the deviation of the 2.1 m, 3.2 m and 4.4 m HCl etched plate experiments from this trend can be explained by the entrapment of disequilibrium fluids. The plots in Figure II- 3.3-a, -b demonstrate that neither reaction 1 (Eq.II-5.1), nor reaction 2 (Eq.II-5.2), can fully explain the data set, but that a combination of them could do so. We therefore suggest that Sn dissolves in HCl-bearing fluids both as Sn(OH)Cl and as $SnCl_2$, with the latter species becoming dominant at high fluid acidities. This interpretation is in accord with the results of Kovalenko et al. (1986), Wilson and Eugster (1990), and Taylor and Wall (1993), who all found average ligand numbers between one and two that increase with increasing acidity. The lack of daughter crystals in synthetic fluid inclusions containing up to 11 wt.% Sn is in agreement with $SnCl_2$ being the dominant species in very HCl-rich fluids, as $SnCl_2$ remains soluble during cooling to room temperature ($SnCl_2$ solubility in pure water at ambient conditions is 89g/100 ml).

Results from the HF-bearing experiments can be compared with data of Kovalenko et al. (1988). Although the latter study was conducted at significantly lower temperatures and pressures (500 °C / 100 MPa), the trend displayed by their data matches well the trend defined by the maximum values of the etched plate runs with 0.5, 1 and 2 m HF solutions and the in-situ cracking experiment with the 3 m HF solution (Figure II- 3.1b). Graphical evaluation of our data indicates a ligand number of 2 (Figure II- 3.3d), consistent with the findings of Kovalenko et al. (1988) who concluded that SnF_2 is the dominant tin-bearing complex in their experiments at 500 °C / 100 MPa.

The data obtained from the NaCl-bearing experiments lie on a well-defined trend with a slope of +1 (Figure II- 3.3a), suggesting that cassiterite may have dissolved according to reaction 6 (Eq.II-5.6). Tin transport in the form of Sn(OH)Cl was proposed also by Kovalenko et al. (1988) based on two solubility measurements in 0.5 m and 4 m NaCl-solutions at 500 °C / 100 MPa.

Taylor and Wall (1993), on the other hand, concluded that the dominant Sn-carrying species in rock-buffered fluids at 700-800 °C / 200 MPa is $NaSn(OH)Cl_2$.

We are not aware of any previous Sn-solubility studies in NaF-bearing fluids. As mentioned above, all experiments of this series produced a separate melt phase due to the reaction of NaF with the quartz cores. Microthermometric measurements on fluid inclusions from all five experiments returned a constant ice melting temperature of -0.4 °C, suggesting that the fluid was buffered by the melt phase at a composition of 0.5 wt.% NaF_{equiv}. LA-ICP-MS analyses of fluid inclusions from runs *NaF5*, *NaF25* and *NaF35* revealed constant Sn concentrations of 150 ± 40 ppm Sn.

Tin concentrations in the coexisting silicate melt are extremely high, ranging from 3 to 7 wt.% Sn. Because in some of the runs all cassiterite completely dissolved in the melt, only the maximum Sn concentrations are regarded as equilibrium values. A first estimate on the composition of this highly unusual melt was obtained chemographically in a plot of the ternary system SiO_2–NaF–H_2O (Figure II- 4.1a). For this, Na : Si -ratios determined by LA-ICP-MS analysis of rapidly quenched, exposed melt inclusions were recalculated to NaF : SiO_2-ratios (assuming that NaF dissolved stochiometrically in the melt), and were plotted together with the bulk starting compositions in the graph. Because all runs were saturated in quartz, melt and fluid, and run *NaF35* additionally in villaumite, the bulk composition of the latter experiment must plot on a cotectic line. Hence, the composition of the ternary melt should be situated somewhere along on a line projected from the SiO_2 apex through the *NaF35* starting composition. The intersection of this line with the array of NaF : SiO_2 -ratios gives a melt composition of 53-63 wt.% SiO_2; 23-31 wt.% H_2O and 13-16 wt.% NaF. A similar water content of 30 wt.% was determined for the eutectic melt composition in the system albite–NaF–H_2O (Koster van Groos and Wyllie, 1968; Figure II- 4.1b). A NaF content of 14 wt.% was then used to transfer Na : Sn -ratios measured by LA-ICP-MS into absolute SnO values (assuming that tin was dissolved as Sn^{2+} at our experimental conditions – see Bhalla et al., 2005), and normalizing everything to 100 wt.%. Using this procedure, the final melt composition is calculated at 49-58 wt.% SiO_2, 21-29 wt.% H_2O, 12-15 wt.% NaF and ca. 8 wt.% SnO.

Melt inclusions containing up to 30 wt.% of water, 6 wt.% fluorine and 0.7 wt.% tin have been described from two tin-mineralized granites in the Erzgebirge, Germany (Webster et al., 1997; Thomas et al., 2000a, b, 2006). Although most of these inclusions are highly peraluminous and a positive correlation between melt peraluminousity and Sn content has been observed in the samples from Ehrensfriedersdorf (Webster et al., 1997; Thomas et al., 2000b). Recent results from Zinnwald (Thomas et al., 2005) suggest that a second, even more hydrous melt of peralkaline character exsolved from the peraluminous melt at high degrees of melt fractionation. Synchrotron-XRF analyses on such peralkaline melt inclusions revealed Sn contents that were comparable to – if not even higher than – that of coexisting peraluminous melt inclusions, demonstrating that significant amounts of Sn were transported by a highly peralkaline phase at the very final stage of magma crystallization (Thomas et al., 2005). This interpretation is supported by the fact that at Zinnwald the Sn concentration of the peraluminous melt decreases with increasing degree of melt fractionation.

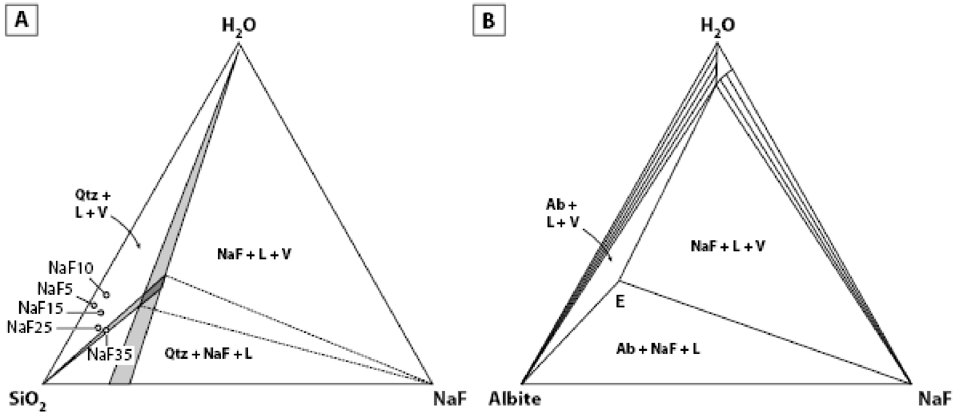

Figure II- 4.1. *(A) Chemographic reconstruction of the melt composition in the fluid-saturated system* SiO_2*–NaF–*H_2O *at 700 °C / 140 MPa, based on Na : Si -ratios determined by LA-ICP-MS analysis of exposed melt inclusions, and the phase assemblages produced in the different starting compositions. Runs NaF5, NaF10, NaF15 and NaF25 contained quartz, fluid and melt, whereas Run NaF35 additionally was saturated in villaumite, implying that this starting composition is situated on a cotectic line. Intersection of this line with the array of recalculated NaF :* SiO_2 *-ratios defines the melt composition somewhere in the dark grey area. (B) An isobaric, isothermal cut through the eutectic point E in the system* $NaAlSi_3O_8$ *– NaF –* H_2O *at 688 °C / 100 MPa is shown for comparison (Koster van Groos and Wyllie; 1968). All compositions are plotted in terms of weight ratios.*

II- 5. Implications for fluid–melt partitioning

The results of this study can be used in conjunction with available data on cassiterite solubility in silicate melts (Taylor and Wall, 1992; Linnen et al., 1995, 1996; Bhalla et al., 2005) to estimate fluid–melt partition coefficients of Sn. The solubility of SnO_2 in a haplogranitic melt (ASI = 1) at 850 °C / 200 MPa and an oxygen fugacity near NNO is 0.7-0.9 wt.% (Linnen et al., 1996). Bhalla et al. (2005) found that the SnO_2-solubility in a natural, peraluminous granitic melt with 2.8 wt.% normative corundum at 200 MPa and log fO_2 ~ NNO decreases from 1.2 to 0.32 wt.% if the temperature is lowered from 850 °C to 700 °C. Assuming that a similar temperature effect applies for the haplogranite melt and that the effect of pressure is comparatively small, Sn-solubility in a haplogranite melt at 700 °C / 0.14 GPa can be estimated at 1500-1900 ppm Sn.

Let us now assume that this melt is saturated in an aqueous fluid with 5 wt.% total salinity, which is a typical value for granites crystallizing at pressures of 100-200 MPa (Burnham, 1979; Audétat and Pettke, 2003). In order to estimate the Sn-solubility in this fluid one needs to know the relative abundance of HCl vs. (NaCl, KCl), because – as shown above – the Sn-solubility in HCl-bearing fluids is far higher than in NaCl-bearing fluids of the same chloride content. Experimental data summarized in Burnham (1979), Candela and Piccoli (1995) and Frank et al., (2003) suggest that in a fluid of 5 wt.% salinity in equilibrium with haplogranite melt (ASI=1) at 800 °C / 100 MPa, ca. 5-10% of the total chlorine is present as HCl (corresponding to 0.05-0.1 m HCl). According to the data presented in Figure II- 3.1a, this HCl concentration corresponds to a solubility of 250-700 ppm Sn, whereas the remaining 4-4.5 wt.% NaCl+KCl (~ 0.8 m) leads to dissolution of another 100 ppm Sn (assuming that the cassiterite solubility in KCl-bearing fluids is comparable to that in NaCl-bearing fluids). Hence, the Sn-solubility in the magmatic fluid is governed by its HCl content despite of a much higher abundance of NaCl and KCl.

From the data presented above, a value of $D_{\text{Sn, fluid/melt}}$ = 0.2-0.5 can be inferred for a haplogranitic melt in equilibrium with a low-salinity fluid at 700 °C / 100-200 MPa and log fO_2 ~ NNO. This result is in agreement with experimental studies of Taylor (1988) and Keppler and Wyllie (1991), who found that $D_{\text{Sn, fluid/melt}}$ is <1 in runs with fluids of similar salinity. Also, our calculated $D_{\text{Sn, fluid/melt}}$ compares favorably with the $D_{\text{Sn, fluid/melt}}$ = 0.1-0.2 derived from LA-ICP-MS analyses of coexisting melt and fluid inclusions in the Canada Pinabete Pluton in northen New Mexico, USA (Audétat and Pettke, 2003). Attainment of fluid saturation in a crystallizing magma will therefore not result in a depletion of Sn in the residual melt. Rather, the Sn content of the residual melt will continue to increase rapidly, because at a typical solubility of 5 wt.% H_2O in the melt a $D_{Sn,\ fluid/melt}$ greater than 20 would be needed to result in a net depletion of Sn in the residual melt (assuming 100% incompatibility of Sn with respect to the crystallizing solid phases). The occurrence of Sn-rich melt inclusions in fluid-saturated, pegmatitic environments (see above) supports this conclusion. The presence of fluorine is unlikely to change this general picture because Sn-solubilities in < 1m HF-solutions were shown to be small (<200 ppm Sn), and because the Sn-solubility in F-bearing melts is similar to that in F-free melts (Bhalla et al., 2005). In fact, $D_{Sn,\ fluid/melt}$ in F-bearing systems is probably smaller than in the F-free system because $D_{Cl,\ fluid/melt}$ decreases rapidly with increasing F concentration the melt (Webster and Holloway, 1990). It should be noted that most Sn-related magmas are peraluminous, which leads to a higher fluid acidity than in the case of subaluminous magmas (e.g., Urabe, 1985). Fluid/melt-partition coefficients in tin-mineralizing magmas could therefore be significantly higher than the value of 0.2-0.5 estimated based on a subaluminous melt composition. However, the common presence of Sn-rich melt inclusions trapped at fluid-saturated conditions indicates that in these systems $D_{Sn,\ fluid/melt}$ usually is far from the critical value of ~20, above which no Sn-enrichment in the residual melt would occur.

II- 6. Conclusions

The combination of synthetic fluid inclusions with Laser-ablation ICP-MS analysis represent a powerful tool to measure mineral solubilities at high pressures and temperatures. This technique is particularly advantageous if solutes re-precipitate during quenching, as is the case for most studies at magmatic-hydrothermal conditions (e.g., Loucks and Mavrogenes, 1999; Hack and Mavrogenes, 2006). The present study seems to be an exception because the Sn solubilities achieved during the experiments appear to be quenchable to room temperature without precipitation of any solid phases. The newly developed etched plate technique produces large, primary fluid inclusions along a single plane, facilitating sample preparation and inclusions analysis. If used in combination with fine-grained solute, this technique can be used to investigate potential disequilibrium effects caused by alloying with the capsule walls. Results from the NaCl-bearing runs suggest that there was no such effect in our experiments. However, Sn solubilities obtained by the etched plate technique in the most concentrated HCl and HF solutions show a large scatter and plot significantly below those obtained by the in-situ cracking technique after one week of pre-equilibration, demonstrating that caution is required if mineral solubilities depend on time-dependent factors such as diffusion rates of H_2 through the capsule walls. In these cases, the in-situ cracking technique is the preferred method, despite the fact that resulting fluid inclusions are smaller and, therefore, more difficult to analyze.

Our data confirm earlier findings that cassiterite-solubility in HCl-bearing fluids is about two orders of magnitude higher than in NaCl and HF-bearing fluids of the same molality. Tin is transported most likely as Sn(OH)Cl in the NaCl-bearing fluids, as Sn(OH)Cl and $SnCl_2$ in the HCl-bearing fluids, and as SnF_2 in the HF-bearing fluids. A comparison of our data with published cassiterite solubilities in silicate melts suggests that the fluid/melt partition coefficient of Sn is smaller than 1 (an the order of 0.2-0.5 in a haplogranitic system at 700 °C / 140 MPa and log fO_2 near NNO) and is governed by the abundance of HCl in the fluid. The alumina saturation index of the melt is expected to exert a strong control on $D_{\mathrm{Sn,\ fluid/melt}}$ due to its influence on fluid acidity. However, reports of tin concentrations of up to 7000 ppm Sn in natural, peraluminous melt inclusions suggest that even relatively acidic fluids cannot efficiently remove Sn from these melt. A potential mechanism for Sn extraction at the final stages of magma crystallization is through alkaline, F-bearing melts similar to those observed in our NaF-bearing experiments. Evidence for the existence of such melts is reported from a tin-mineralized granite at Zinnwald (Thomas et al., 2005).

References

Aranovich L. Y. and Newton R. C. (1996) H_2O activity in concentrated NaCl solutions at high pressures and temperatures measured by the brucite-periclase equilibrium. *Contrib. Min. Petrol.* **125**, 200-212.

Audétat A. and Pettke T. (2003) The magmatic-hydrothermal evolution of two barren granites: a melt and fluid inclusion study of the Rito del Medio and Cañada Pinabete Plutons in northern New Mexico (USA). *Geochim. Cosmochim. Acta* **67**, 97-121.

Baumann L., Kuschka E., and Seifert T. (2000) *Lagerstätten des Erzgebirges*. Enke, Stuttgart.

Bhalla P., Holtz F., Linnen R. L., and Behrens H. (2005) Solubility of cassiterite in evolved granitic melts: effect of T, fO_2, and additional volatiles. *Lithos* **80**, 387-400.

Burnham C. W. (1979) Magmas and hydrothermal fluids. In *Geochemistry of hydrothermal ore deposits* (ed. H. L. Barnes), Wiley, New York, pp. 71-136.

Candela P. A. and Piccoli P. M. (1995) Model ore-metal partitioning from melts into vapor and vapor/brine mixtures. In *Magmas, Fluids and Ore Deposits*, (ed. J. F. H. Thompson), pp. 101-128. Mineralogical Association of Canada, Short Course Series, Vol. 23.

Ellis A. J. (1963) The effect of temperature on the ionization of hydrofluoric acid. *Chem. Soc. [London] Jour.* **166**, 4300-4304.

Eugster H. P. and Baumgartner L. (1987) Mineral solubilities and speciation in supercritical metamorphic fluids. In *Thermodynamic modeling of geological materials; minerals, fluids and melts*, Reviews in Mineralogy, Vol. 17 (ed. I. S. E. Carmichael and H. P. Eugster), Mineralogical Society of America, Washington DC, pp. 367-403.

Frank M. R., Candela P. A., and Piccoli P. M. (2003) Alkali exchange equilibria between a silicate melt and coexisting magmatic volatile phase: An experimental study at 800 °C and 100 MPa. *Geochim. Cosmochim. Acta* **67**, 1415-1427.

Hack A. C. and Mavrogenes J. A. (2006) A synthetic fluid inclusion study of copper solubility in hydrothermal brines from 525 to 725 °C and 0.33 to 1.7 GPa. *Geochim. Cosmochim. Acta* **70**, 3970-3985.

Günther D., Frischknecht R., Heinrich C. A., and Kahlert H. J. (1997) Capabilities of an Argon Fluoride 193nm Excimer Laser for Laser Ablation Inductively Coupled Plasma Mass Spectrometry Microanalysis of Geological Materials. *J. Anal. Atom. Spectrom.* **12**, 939-944.

Günther D., Audétat A., Frischknecht R., and Heinrich C. A. (1998) Quantitative analysis of major, minor and trace elements in fluid inclusions using Laser Ablation-Inductively Coupled Plasma-Mass Spectrometry (LA-ICP-MS). *J. Anal. Atom. Spectrom.* **13**, 263-270.

Keppler H. and Willie P. J. (1991) Partitioning of Cu, Sn, Mo, W, U and Th between melt and aqueous fluid in the systems haplogranite-H_2O-HCl and haplogranite-H_2O-HF. *Contrib. Mineral. Petrol.* **109**, 139-150.

Klintsova A. P. and Barsukov V. L. (1973) Solubility of cassiterite in water and in aqueous NaOH solutions at elevated temperatures. *Geochem. Int.* **10**, 540-547.

Klintsova A. P., Barsukov V. L., Shemarykina T. P., and Khodakovskiy L. I. (1975) Measurement of the stability constants for Sn(IV) hydrofluoride complexes. *Geochem. Int.* **12**, 207-215.

Kovalenko N. I., Ryzhenko B. N., Barsukov V. L., Klintsova A. P., Velyukhanova T. K., Vlynets M. P., and Kitayeva L. P. (1986) The solubility of cassiterite in HCl and HCl + NaCl (KCl) solutions at 500 ºC and 1000 atm under fixed redox conditions. *Geochem. Int.* **23**, 1-16.

Kovalenko N. I., Ryzhenko B. N., Velyukhanova T. K., and Barsukov V. L. (1988) Cassiterite solubility in HF solutions and forms of tin transport by supercritical fluids. *Transactions (Doklady) of the U.S.S.R. Academy of Sciences: Earth Science Sections* **290**, 212-215.

Koster van Groos A. F. and Wyllie P. J. (1968) Melting relationships in the system $NaAlSi_3O_8$–NaF–H_2O to 4 kilobars pressure. *J. Geology* **76**, 50-70.

Lehmann B. (1990) *Metallogeny of Tin*. Springer, Berlin.

Linnen R. L., Pichavant M., Holtz F., and Burgess S. (1995) The effect of fO_2 on the solubility, diffusion, and speciation of tin in haplogranitic melt at 850 ° and 2 kbar. *Geochim. Cosmochim. Acta* **59**, 1579-1588.

Linnen R. L., Pichavant M., and Holtz F. (1996) The combined effects of fO_2 and melt composition on SnO_2 solubility and tin diffusivity in haplogranitic melts. *Geochim. Cosmochim. Acta* **60**, 4965-4976.

Longerich H. P., Jackson S. E., and Günther D. (1996) Laser ablation inductively coupled plasma mass spectrometric transient signal data acquisition and analyte concentration calculation. *J. Anal. Atom. Spectrom.* **11**, 899-904.

Loucks R. R. and Mavrogenes J. A. (1999) Gold solubility in supercritical hydrothermal brines measured in synthetic fluid inclusions. *Science* **284**, 2159-2163.

Mavrogenes J. A. and Bodnar R. J. (1994) Hydrogen movement into and out of fluid inclusions in quartz: experimental evidence and geologic implications. *Geochim. Cosmochim. Acta* **58**, 141-148.

Nekrasov I. Y. and Ladze T. P. (1973) Solubility of cassiterite in silicic chloride solutions at 300 and 400 ºC. *Doklady Akad. Nauk SSSR* **213**, 145-147.

Nekrasov I. Y., Epel'baum M. B., and Sobolev V. P. (1980) Partitioning of tin between melt and chloride fluid in the granite-SnO-SnO_2 fluid system. *Doklady, Acad. Sci. USSR, Earth Sci. Section* **252**, 165-168.

Newton R. C. and Manning C. E. (2000) Quartz solubility in H_2O-NaCl and H_2O-CO_2 solutions at deep crust-upper mantle pressures and temperatures: 2-15 kbar and 500-900 ºC. *Geochim. Cosmochim. Acta* **64**, 2993-3005.

Pokrovskii V. A. (1999) Calculation of the standard partial molal thermodynamic properties and dissociation constants of aqueous HCl° and HBr° at temperatures to 1000 ºC and pressures to 5 kbar. *Geochim. Cosmochim. Acta* **63**, 1107-1115.

Sterner S. M. (1992) Synthetic fluid inclusions XI. Notes on the application of synthetic fluid inclusions to high P-T experimental aqueous geochemistry. *Am. Mineral.* **77**, 156-167.

Tagirov B. R., Zotov A. V., and Akinfiev N. N. (1997) Experimental study of dissociation of HCl from 350 to 500 ºC and from 500 to 2500 bars: thermodynamic properties of HClº(aq). *Geochim. Cosmochim. Acta* **61**, 4267-4280.

Taylor J. R. (1988) Experimental studies on tin in magmatic-hydrothermal systems. Ph. D. thesis, Monash University, Australia.

Taylor J. R. and Wall V. J. (1992) The behavior of tin in granitoid magmas. *Econ. Geol.* **87**, 403-420.

Taylor J. R. and Wall V. J. (1993) Cassiterite solubility, tin speciation, and transport in a magmatic aqueous phase. *Econ. Geol.* **88**, 437-460.

Thomas R., Webster J. D., and Heinrich W. (2000a) Melt inclusions in pegmatitic quartz: complete miscibility between silicate melts and hydrous fluids at low pressure. *Contrib. Mineral. Petrol.* **139**, 394-401.

Thomas R. and Webster J. D. (2000b) Strong tin enrichment in a pegmatite-forming melt. *Mineralium Deposita* **35**, 570-582.

Thomas R., Förster H. J., Rickers K., and Webster J. D. (2005) Formation of extremely hydrous melt fractions and hydrothermal fluids during differentiation of highly evolved tin-granite magmas: a melt/fluid inclusion study. *Contrib. Min. Petrol.* **148**, 582-601.

Urabe T. (1985) Aluminous granite as a source of hydrothermal ore deposits: an experimental study. *Econ. Geol.* **80**, 148-157.

Webster J. D. and Holloway J. R. (1990) Partitioning of F and Cl between magmatic hydrothermal fluids and highly evolved granitic magmas. In *Ore-bearing granite systems; Petrogenesis and mineralizing processes* (ed. H. J. Stein and J. L. Hannah), Geological Society of America, Special Paper, Vol. 246, pp. 21-34.

Webster J. D., Thomas R., Rhede D., Förster H. J., and Seltmann R. (1997) Melt inclusions in quartz from an evolved peraluminous pegmatite: Geochemical evidence for strong tin enrichment in fluorine-rich and phosphorous-rich residual liquids. *Geochim. Cosmochim. Acta* **61**, 2589-2604.

Tischendorf G. (1977) Geochemical and petrographic characteristics of silicate magmatic rocks associated with rare-element mineralization. In *Metallization associated with acidic magmatism* (eds. M. Stemprok, L. Burnol and G. Tischendorf), Ustred. ustav. geol., Vol. 2, Prague, pp. 41-96.

Wilson G. A. and Eugster H. P. (1990) Cassiterite solubility and tin speciation in supercritical chloride solutions. In *Fluid-mineral interactions: a tribute to H.P. Eugster* (ed. R. J. Spencer and I. M. Chou), The Geochemical Society, Special Publication , Vol. 2, pp. 179-195.